Table of contents

List of figures

List of Tables

1 Introduction

In the standard model of elementary particles[1,2] all matter is comprised of quarks and leptons which exist in three generations of doublets. Each lepton doublet includes a massive charged particle and a massless neutral neutrino that are limited to purely weak interactions. The weak interactions are mediated by Z^0 or $W^{+/-}$ bosons in neutral-current and charged-current interactions, respectively. The vector bosons also couple to quarks and thus neutrino interactions with nuclear matter are possible. Interactions of ν_e and ν_μ have been studied whereas those of ν_τ as yet have not been observed. The first observation of ν_τ charged-current interactions are presented in this thesis.

Pauli postulated the neutrino's existence in 1930 to explain the anomalous energy distribution of electrons from beta decay. Evidence of their existence was found experimentally 20 years later by Reines and Cowan *et al* [3] using $\bar{\nu}_e$ at the Savannah River nuclear reactor in inverse beta decay experiments. Davis and Harmer proved that the neutrino must have a distinct antiparticle in 1959.[4] In 1962 the ν_e and ν_μ were distinguished at Brookhaven National Lab using $\bar{\nu}_\mu$ + proton reaction [5] leading to the inclusion of neutrinos in specific lepton generations.

Ever since the discovery of the charged tau-lepton by Perl *et al* [6] in 1975, the existence of an associated neutrino of the same family has been assumed. There is experimental evidence to support this hypothesis: the invisible width of the Z^0 limits the number of light neutrino types to three[7] and the missing energy of tau-lepton's decay spectrum requires the existence of a light neutral particle[8] which is assumed to be the tau neutrino.

Before this experiment the tau-neutrino was the only stable particle in the Standard Model whose interaction had not been observed. Interactions of the muon and electron neutrino with nuclear matter have been studied extensively but a direct observation of tau-neutrino interaction has not been achieved in the same manner. Independent of their lepton generation, all neutrinos are expected to interact through the same mechanism and this could be verified through comparison of ν_τ interactions to those of ν_e and ν_μ.

Aside from verifying the interaction of the third lepton generation and thus completing an important component of the Standard Model, detection of the ν_τ has other motivations. A great effort is underway to measure a non zero neutrino mass. Flavor changing in neutrinos indicates that they have mass and the witnessing of flavor changing oscillations is the goal of several current experiments. Any experiment expecting to see $\nu_\mu \rightarrow \nu_\tau$ oscillations will require detecting ν_τ interactions and benefit from the techniques of this experiment.

Experiment E872 used an emulsion detector in a tau-neutrino-enriched neutrino beam to observe ν_τ + N interactions. The tau lepton produced in the interaction was identified by a signature kink in a track caused by the decay channels: $\tau \rightarrow$ one charged daughter. Single charged decays of the tau have a total branching fraction of 85%.

The neutrino beam was created using 800GeV protons from the Fermilab Tevatron that interacted in a massive tungsten dump. The primary source of the ν_τ component of the beam is the decay of D_s mesons created in these interactions. The leptonic decay of the $D_s \rightarrow \tau\, \nu_\tau$, which account for ~ 6% of all D_s decays, results in a $\bar{\nu}_\tau\ \nu_\tau$ pair since the τ decays into a $\bar{\nu}_\tau$ as well. The primary source of ν_μ and ν_e,

whose interactions were also observed in the emulsion target, are the decays of $D^{+/-}$, D^0 and D_s in the tungsten dump. This thesis presents evidence of $\nu_\tau + N \rightarrow X + \tau$ found in Fermilab's E872 experiment.

This thesis is organized as follows: in chapter two the theory of neutrino interactions and of neutrino production are presented, chapter three describes the experimental apparatus including the neutrino beam and emulsion-spectrometer, chapter four describes the data collected from the detector and the process of the selection of neutrino interaction events making up the data set. Chapters five and six document the tau neutrino interaction selection procedure and the results of the selection including possible backgrounds to the tau-neutrino signal. Chapter seven is a statistical analysis of the results including a probability analysis of each selected tau-neutrino event. There is one appendix which details the calculation of the expected rate of all types of neutrino interaction in the emulsion detector.

2 Phenomenology

2.1 Neutrino interactions in the Standard Model

Within the Standard Model of elementary particles, the interaction of neutrino is mediated by the vector bosons; $W^{+/-}$ for charged-current interactions and Z^0 for neutral current interactions. These exchanges conserve the lepton generation, that is, any exchange of a W or Z can only alter the lepton between the two states in its own doublet. This is shown graphically with the Feynman diagrams in Figure 2-1.

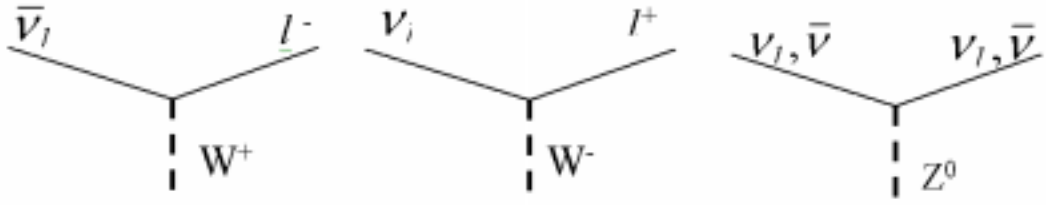

Figure 2-1 Feynman diagrams of all possible neutrino and antineutrino interactions.

2.1.1 Neutrino-nucleon interactions

Neutrino–nucleon interactions result when the intermediate boson of the interactions displayed above couple to the quarks of nuclear matter. It is possible to distinguish between ν_e , ν_μ and ν_τ charged-current interactions since the final state will include a charged leptons along with the final quark states. The kinematics of inelastic neutrino–nucleon scattering are shown in Figure 2-2. Because of quark confinement, the final state quark is only observed in a hadron.

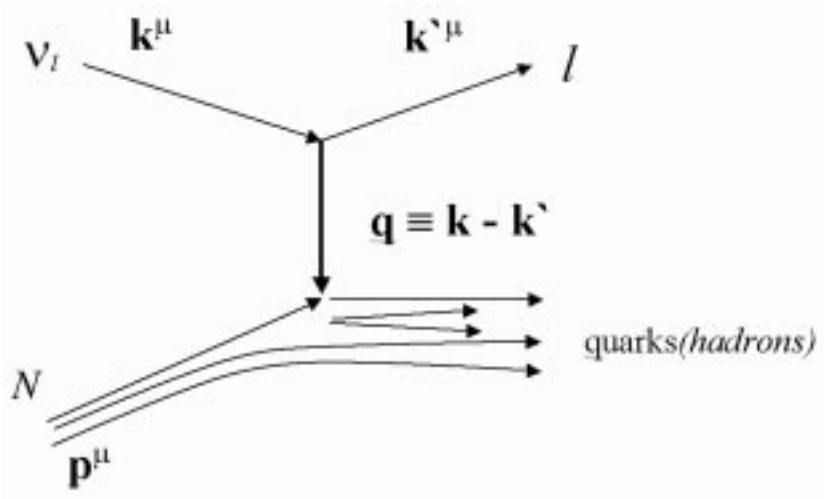

Figure 2-2 Kinematics of neutrino –nucleon interactions

The three relevant variables describing the interaction are: the square of the momentum transfer Q^2, the inelasticity of the interaction y, and the Bjorken-x variable describing the fraction target nucleons momentum carried by the struck quark. These are defined in Equations 2-1 through 2-3.

$$Q \equiv -q^2 = (k - k')^\mu (k - k')_\mu \qquad \textbf{Eq. 2-1}$$

$$y \equiv \frac{E_{quarks}}{E_\nu} = \frac{q \cdot p}{k \cdot p} \qquad \textbf{Eq. 2-2}$$

$$x \equiv \frac{-q^2}{2q \cdot p} = \frac{Q^2}{2m_N E_{quarks}} \qquad \textbf{Eq. 2-3}$$

The interaction cross-sections with nucleons are expressed in terms of the nucleon structure functions F_i that describe the distribution of the momentum of the partons when the nucleons momentum is large.

$$\frac{d^2\sigma}{dxdy} = \frac{G^2 m_N E_\nu}{\pi} \cdot \left[(1-y) F_2^{\nu N}(x) + yxF_1^{\nu N}(x) + y(1-\frac{y}{2}) xF_3^{\nu N} \right] \qquad \textbf{Eq. 2-4}$$

The structure functions can be expressed in terms of the nucleons quark and anti-quark distributions: $q(x)$ and $\bar{q}(x)$

$$F_2^{\nu N}(x) = 2xF_1^{\nu N}(x) = 2x(q(x) + \bar{q}(x)) \qquad \textbf{Eq. 2-5}$$

$$xF_3^{\nu N}(x) = 2x(q(x) - \bar{q}(x)) \qquad \textbf{Eq. 2-6}$$

here $q(x) = d^p(x) + d^n(x)$ and $\bar{q}(x) = \bar{u}^p(x) + \bar{u}^n(x)$ and it is assumed that there are an equal number of protons and neutrons in the nucleus.

This leads to the following equations for neutrino and antineutrino cross-sections:

Neutrino : $$\frac{d^2\sigma}{dxdy} = \frac{G^2 m_N E_\nu x}{\pi} \cdot \left[q(x) + \bar{q}(x)(1-y^2) \right] \qquad \textbf{Eq. 2-7}$$

Antineutrino: $$\frac{d^2\sigma}{dxdy} = \frac{G^2 m_N E_\nu x}{\pi} \cdot \left[\bar{q}(x) + q(x)(1-y^2) \right] \qquad \textbf{Eq. 2-8}$$

The total cross-section is computed by integrating these over *x* and *dy*. The result increases linearly with neutrino energy: $\sigma = \sigma_0 \cdot E_\nu$. Equation 2-7 also suggests that for an isoscaler target with equal number of up quarks and down quarks the total cross-section for neutrinos is three times as large as the antineutrino cross-section since

$\int (1-y^2)dy = 1/3$. The true ratio is slightly smaller due to the presence of sea quarks within the nucleons. The total cross-section has been thoroughly measured for muon and electron neutrinos and antineutrinos over a wide energy range. The measured cross-sections displayed in Figure 2-3 show the linear relationship to neutrino energy.

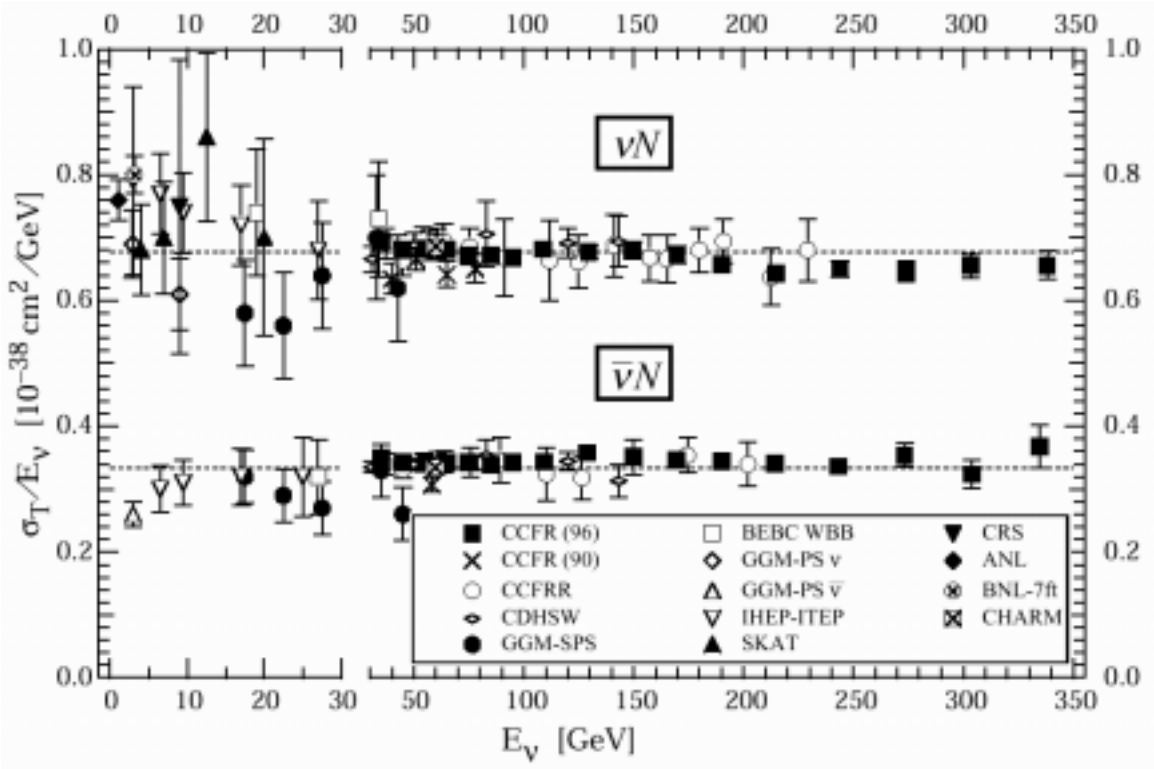

Figure 2-3 Total neutrino nucleon and anti-neutrino nucleon cross-section measurements. Figure is taken from reference 27. Results are from CCFR(96)[9], CCFR(90)[10],CCFRR[11],CDHSW[12],GGM-SPS[13],BEBC WBB[14],GGM-PS(N)[15],GGM-PS[16],IHEP-ITEP[17],SKAT[18],CRS[19],ANL[20],BNL-7ft[21],CHARM[22]

The average value of σ_0 for the charged-current cross-section for neutrinos is 0 $.677 \pm 0.014 \times 10^{-38}$ cm^2/GeV and for anti-neutrinos is 0 $.334 \pm 0.008 \times 10^{-38}$ cm^2/GeV.

Tau neutrino charged-current interaction result in the production of the more massive tau-lepton. For this reason there is a significant threshold effect: the cross-section is 0 at ν_τ energies below approximately twice the tau mass. Since the interaction is kinematically limited, the linear energy dependence of the cross-section is only

approached asymptotically at higher energies. The cross-section for ν_τ charged-current interactions is given by the expression: $\sigma(\nu_\tau) = \sigma_0 \cdot K(E) \cdot E$. Here σ_0 is the same as measured for ν_μ and ν_e charged-current interactions and K(E) is the kinematic factor introduced by production of the more massive tau.

Calculation of the kinematic factor K(E) has been carried out explicitly using the prescription for creation of a heavy lepton of Albgight and Jarlkog.[23] The ELQH set of structure functions were used[24]. The result is shown as the ratio of $\sigma(\nu_\tau)$ to $\sigma(\nu_\mu)$ for various neutrino energies in Figure A-2.

2.1.2 Neutrino production

The source of neutrinos used in E872 are the leptonic and semi-leptonic decays of mesons which are in turn produced by high energy proton-nucleon interactions.

The most general leptonic meson decay is shown in Figure 2-4.

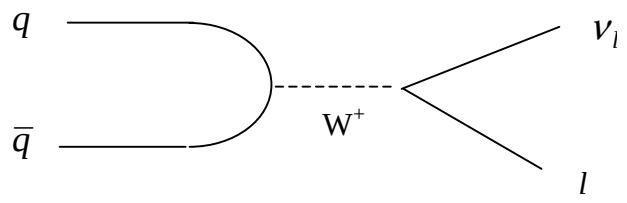

Figure 2-4 Feynman diagram of leptonic meson decay

Muon neutrinos result from decay of the $\pi^{\pm}$, $K^{\pm}$, K^0,$D^{\pm}$,D^0,D_s. Electron neutrinos are produced from the same sources except the π's which do not have a significant electron decay channel. The lightest meson that has a significant τ - ν_τ pair decay mode is the D_s and it is through this decay that E872 creates its ν_τ beam. The tau that is produced in this decay subsequently decays itself resulting in a $\bar{\nu}_\tau$. Hence each D_s produces a ν_τ $\bar{\nu}_\tau$ pair. A diagram of the ν_τ production chain is shown in Figure 2-5.

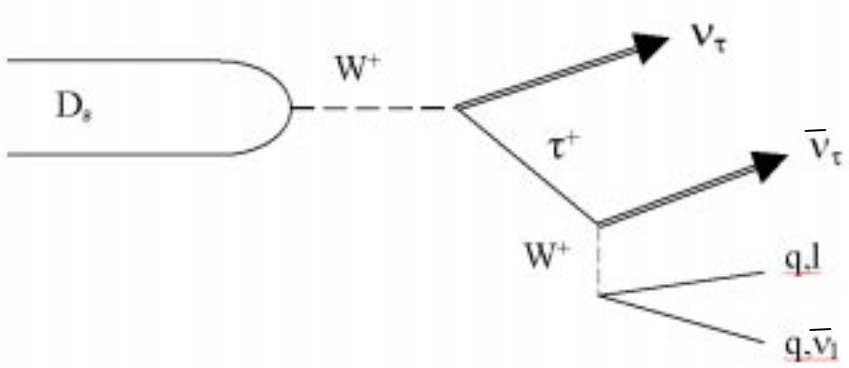

Figure 2-5 D_s decay chain resulting in a neutrino antineutrino pair.

The mass difference between the D_s and the tau (209 MeV/c^2) is only a fraction of the tau mass (1.777 GeV/c^2) whereas the tau is much more massive than the sum of its decay products. For this reason the energy of the neutrino resultant from the tau decay is much greater than that of the initial D_s decay due to the allowable phase space.

2.2 Properties of the tau-lepton.

The charged-current interactions of the ν_τ result in a tau-lepton and it is through the tau lepton that ν_τ interactions are identified in this experiment. For this reason the properties of the tau are reviewed here.

The tau lepton has been studied extensively at electron-positron colliders where τ^+ τ^- pairs are produced. The most accurate measurement of the mass comes from the BES collaboration[25]: 1776.96 ± 0.35 GeV/c^2 and the world average is 1777.03 ± 0.30 GeV/c^2 [27] The tau lifetime has been measured most accurately by the ALEPH collaboration [26] as 290. 1 ± 1.9 $\times 10^{-15}$ seconds. The word average is 290.6 ± 1.1 $\times 10^{-15}$ seconds [27]. This short lifetime corresponds to a $c\tau$ of 87.2 microns. Consequently it will not travel very far unless it is created with a high momentum. Detection in colliders is through the reconstruction of its decay products since the taus themselves do not live long enough to pass through any part of the detectors.

The tau decays only through the emission of a virtual W. The final state depends on the decay of the W and since the tau's mass is greater than the electron, muon and the first quark generation, there are three first order channels.

$$\tau \rightarrow \bar{\nu}_\tau \nu_e e^+$$

$$\tau \rightarrow \bar{\nu}_\tau \nu_\mu \mu^+$$

$$\tau \rightarrow \bar{\nu}_\tau u\bar{d}$$

Since there are three color states of the quark pair, the ratio of leptonic channels to hadronic channels is expected to be (2:3) which is close to the observed value, as can be seen in Table 2-1. The number of hadronic channels possible as final states is increased by gluon radiation and the branching ratios to many final states have been measured.[27]

Decay products	Branching ratio (%)
$\nu_\tau\ \nu_\mu\ \mu^-$	17.37 ± .07
$\nu_\tau \nu_e\ e^-$	17.83 ± .06
$\nu_\tau \rho^-$	25.40 ± .14
$\nu_\tau \pi^-$	11.09 ± .12
$\nu_\tau\ \pi^-\ 2\pi^0$	9.13 ± .07
$\nu_\tau\ \pi^-\ 3\pi^0$	1.08 ± .10
$\nu_\tau\ K^-$	.699 ± .27
$\nu_\tau\ \pi^-\pi^-\pi^+$	9.49 ± .11
$\nu_\tau\ \pi^-\pi^-\pi^+\pi^0$	4.32 ± .08

Table 2-1 Major decay modes of tau lepton to 1 and 3 charged daughters. From reference [27]

Of interest to this thesis are the "1-prong" decay modes: those modes that result in only one charged particle. It is through these modes that taus are identified. In all , 85.5% of the tau's decay modes are "1-prong". Of these, 20.8% are electron, 20.3% are muon and 58.9% are hadronic modes

3 Experiment E872

3.1 Introduction

A detector used to identify tau leptons resulting from neutrino interactions must be capable of recording neutrino interactions, tracking the resultant particles at sub-millimeter lengths and have angular resolution of better than 1 mrad. The small resolution necessary to track the tau required that nuclear emulsion be used as the primary detector and the entire design philosophy of the experiment was centered around its use.

There are two difficulties in using emulsion that needed to be overcome by the rest of the experimental set-up: firstly the shielding needed to protect the emulsion from unwanted background tracks and secondly locating the neutrino interactions within the large volume of emulsion. Emulsion is a permanently active detector and all charged particles traversing the emulsion from the time of its production to the time of its development will leave tracks. If the density of background tracks is too high they will mask those of neutrino interactions. Also, tracks in the emulsion are viewable only by

microscope and a good prediction of their location is necessary or else searching for them would take years.

E872 created a neutrino beam that was rich with tau neutrinos by using 800 GeV/c protons incident on a tungsten beam dump. These neutrinos were directed at a hybrid emulsion/spectrometer detector that was used to identify and record neutrino interactions by the tracks of charged particles resulting from these interactions. A spectrometer downstream of the emulsion triggered on neutrino events occurring in the emulsion and tracking detectors were used to point back to areas in the emulsion which was subsequently scanned by an automated microscope. The signature of a ν_τ interaction was a kink in one of the emulsion tracks that indicated a single charge decay of the resulting tau. A muon identification system and an electromagnetic calorimeter were used to identify muons and electrons that were created in ν_μ and ν_e interactions and thus to distinguish these types of events from tau-neutrino interactions.

3.2 The Neutrino Beam Line

The neutrino beam was generated with 800 GeV/c protons extracted from Fermilab's Tevatron accelerator to the experimental hall along the PWEST beam line. A high intensity beam was needed since very few ν_τ are produced in the proton-tungsten interactions and neutrinos have a small interaction cross-section . The proton beam trajectory was monitored and controlled at several places along the beam pipe to insure accurate positioning of the beam on the dump. This was necessary for three reasons: firstly neutrino flux at the detector target is decreased if the beam is not directed precisely at the target, secondly the effectiveness of the shielding of the emulsion target is dependant on beam direction and thirdly the intensity of the proton beam is so high that if it were to strike an un-cooled section of the beam dump the surrounding radiation shielding would melt.

For safety, 100 meters upstream of the experimental hall was another beam dump to which the proton beam could be diverted by an electromagnet, in case of a failure of the downstream muon shielding. This was essential since, if a single spill of protons were to reach the E872 dump without the muon shielding active, the resultant track

density in the emulsion detector due to the muon flux would render the emulsion useless. This safety provision was never needed during the experimental run.

3.2.1 Beam dump

The beam dump was designed maximize the number of ν_τ interactions observed in the downstream detector.

Neutrinos are created from the decay of both the light and charmed mesons. The majority of the high energy neutrinos in the beam are ν_e and ν_μ from the decay of the $D^{+/-}$, D^0, and D_s: tau neutrinos are produced in D_s decays. The E872 dump was designed to enrich the ν_τ fraction of the beam by limiting the number of light meson decays which only result in ν_μ. The light mesons, pions and kaons, have much longer lifetime than do the charmed mesons and subsequently lose energy by re-interacting in the beam dump before they can decay. The nuclear interaction length of tungsten is 9.6 cm.[27] while $c\tau$ for a pion (kaon) is 7.8 m (3.7m).[27] Thus, the majority of the high-energy in neutrinos the beam are from charm-meson decays. These will be referred to as "prompt" for the remainder of this thesis since the charmed mesons result directly from the proton-tungsten interaction. Neutrinos resulting from the decay of the lighter mesons are referred to as "non-prompt": their parent mesons result not only from the initial proton-tungsten interaction but also secondary interactions within the dump.

Table 3-1 lists charm mesons and the decay channels that contribute to the prompt portion of the neutrino beam.

The resulting neutrino beam contains approximately is ~80% ν_μ , 18% ν_e and 2% ν_τ. Although there is a still majority of ν_μ, most of these are from non-prompt sources and their lower energy significantly reduces their relative contribution to the number of interaction in the emulsion target. Details of the calculation of neutrino beam composition are discussed in Appendix A.

3.2.2 Downstream beam line

To maximize the number of neutrino interactions, the emulsion target was positioned 36 meters downstream, as close to the dump as possible. The proximity was limited by the shielding needed to keep the density of tracks in the emulsion below the

Meson	Decay channel	Branching fraction (%)
D	$\overline{K}^0 e^+ \nu_e$	6.7 ± . 9
	$\overline{K}^0 \mu^+ \nu_\mu$	$7.0\ ^{+3.0}_{-2.0}$
	$K^- \pi^+ \mu^+ \nu_\mu$	3.2 ± 0.4
	$K^- \pi^+ e^+ \nu_e$	4.1 ± 0.8
	$\overline{K}^*(892)^0 e^+ \nu_e$	4.8 ± 0.5
	$\overline{K}^*(892)^0 \mu^+ \nu_\mu$	4.4 ± 0.6
	$\pi^0 l^+ \nu_l$	0.31 ± 0.04
	$\mu^+ \nu_\mu$	0.08 ± 0.05
	$\phi \mu^+ \nu_\mu$	< 3.72
	$\phi e^+ \nu_e$	< 2.09
	$\eta'(958) \ell \nu_\ell$	< 0.9
	$\eta \ell \nu_\ell$	< 0.5
	$(\overline{K}^*(892)\pi)^0 e^+ \nu_e$	< 1.2
	$K^- \pi^+ \pi^0 \mu^+ \nu_\mu$	< 0.14
D^0	$K^- e^+ \nu_e$	3.64 ± 0.18
	$K^- \mu^+ \nu_\mu$	3.22 ± .17
	$\overline{K}^0 \pi^- e^+ \nu_e$	$2.8\ ^{+1.7}_{-0.9}$
	$K^- \pi^+ \pi^- \mu^+ \nu_\mu$	$1.6\ ^{+1.3}_{-0.5}$
	$\pi^- e^+ \nu_e$	0.37 ± 0.06
D_s	$\tau^+ \nu_\tau$	6.6 ± 0.8
	$\phi \ell \nu_l$	2.0 ± 0.5
	$\eta \ell \nu_l$	3.5 ± 1.0
	$\eta'(958) \ell \nu_l$	2.0 ± 0.5
	$\mu^+ \nu_\mu$	0.46 ± 0.19

Table 3-1 Decay modes of the charmed mesons that contribute to the neutrino beam. Here *l* stands for muon or electron

limit of 5×10^5 cm^{-2} for automated scanning procedure which is described in section 4.2.1. The main elements of the E872 beam line between the tungsten beam-dump and the emulsion are magnetic and passive shielding used to reduce the flux of charged particles from the beam dump.

The major sources of background tracks are muons created in the beam-dump and their secondary interactions in material surrounding the detector. Low energy neutrons from the dump that were captured near the emulsion with the emission of a gamma are also sources of background tracks.

3.2.3 Muon shielding

The layout of the muon shielding is shown in Figure 3-1.

Penetrating muons were by far the largest source tracks in the emulsions detector and only the success in shielding the emulsion from them made the experiment feasible. The magnetic and passive shielding reduced the muon flux at the emulsion target by five orders of magnitude at the center of the emulsion detector. Measurements of the muon flux dump in a scintillating paddle counter placed in front of the emulsion target stand 1.5 meter off of center were 6kHz/cm^2 while the average flux measured across the emulsion target using test areas of emulsion was only 0.2 Hz/cm^2.

The magnetic shielding consisted of two large steel electromagnets that swept the muons to either side of the emulsion target. The first magnet was positioned directly downstream of the tungsten dump. It had a central pole of steel focused to 7cm. in width and was 7m long along the beam. The magnetic field along the pole was 3T in the vertical direction and provided a transverse momentum kick of 6.3 GeV/c to charged particles that passed through the entire length of the pole. Muons of less than 650 GeV would be swept at least 50 cm off the beam axis at the position of the emulsion detector. The space between the focused pole and the return steel was filled with lead to absorb lower momentum charged particles.

A second sweeping magnet in the shielding system was 2 meters further downstream. It shielded the emulsion from muons that were directed toward the emulsion from the magnetic field in the return steel of the primary shielding magnet. It had a steel pole 70 cm wide and 5 meters along the beam and a magnetic field of 1.8 Tesla.

The passive elements of the shielding consisted of 18 meters of steel between the second magnet and the emulsion target and 13 meters of steel in the magnet poles. This much steel absorbs muons with a momentum less than 40GeV/c. There were two regions of high flux along the paths of deflected muons that were left unshielded to minimize the possibility of secondary interactions generating additional charged particles which would traverse the emulsion target.

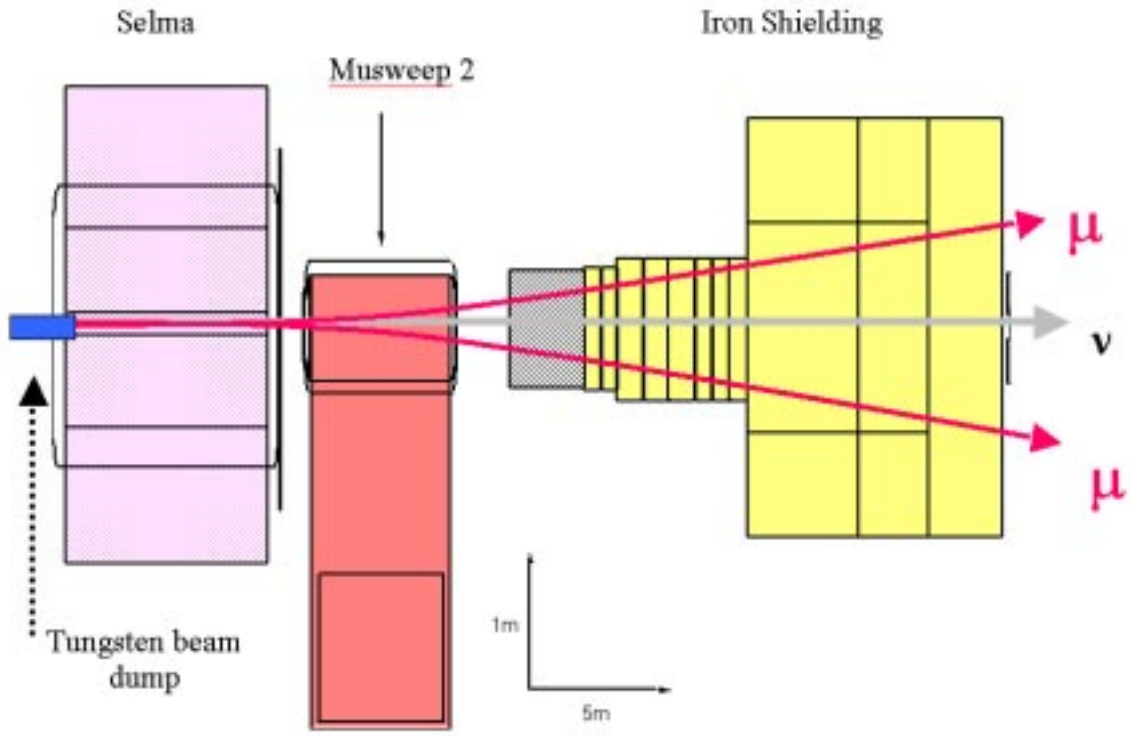

Figure 3-1 Muon shielding used in E872. Muons are directed to either side of the emulsion target.

To shield against neutrons a 1m layer of concrete was placed around both the tungsten dump and the first magnet and a three meter tall concrete wall downstream of the second magnet was erected. Additionally, bags of polyethylene beads and Borax were placed directly around the dump. Finally, the emulsion target itself was surrounded by a 1cm thick lead skin.

3.3 The E872 detector

Identification of ν_τ charged-current interaction requires a detector that can measure tracks that are 100 μm or longer and at the same time identify electrons and muons. The need to measure tracks down to 100 μm is so that the tau lepton track and its decay can be observed, while the identification of muons and electrons is to identify background ν_e and ν_μ interactions.

E872 used a hybrid emulsion/spectrometer detector in which all charged particles resulting from a neutrino interactions were tracked for several centimeters in emulsion with a spectrometer downstream to measure the properties of particles produced in the event.

Two types of nuclear emulsion targets were exposed to the neutrino beam. One in which the emulsion itself was the target material and a second type where steel plates were interleaved with emulsion. The second type had a larger mass, and therefore a higher probability of a neutrino interaction at lower cost.

Once exposed to the beam the emulsion was developed and then the charged particle tracks were recorded with an automated scanning microscopes. These emulsion tracks are linked to data recorded in the rest of the spectrometer to reconstruct the neutrino interaction event. Properties of nuclear emulsion and the target configurations used in E872 are also presented in section 3.3.1

The remaining elements of the E872 detector were used not only to identify the resulting electron or muon from charged-current neutrino interactions but also to pinpoint areas in the emulsion to scan and to measure the kinematic properties of the interaction. A precision scintillating-fiber tracker recorded particle trajectories as they exited the emulsion targets. Downstream of the emulsion target and scintillating-fiber system were a large aperture analysis magnet used for momentum analysis, an electro-magnetic calorimeter and a muon identification system. Tracking drift chambers upstream, inside and downstream of the analysis magnet allowed the momentum measurement of tracks found in the emulsion. These drift chambers also linked to signals in the electromagnetic calorimeter and muon id system do be linked to the scintillating-fibers. The spectrometer elements, including the scintillating-fiber system the EM calorimeter and the muon identification system are described in detail elsewhere[28,29], and in this thesis only the components of importance to this thesis will be discussed.

3.3.1 Emulsion

The experiment used eight different emulsion targets in the neutrino beam. These served dual roles, providing interaction material for the neutrino beam and detecting particles resulting from the interaction with high-resolution. The targets consisted of several layers of thin emulsion plates, 50 cm by 50 cm oriented transverse to the beam direction and are shown in Figure 3-2. Each plate had a layer of emulsion on either side of a supporting acrylic sheet. Two of the three different types of plates also included a 1mm thick steel sheet to augment the available interaction mass. Each emulsion thus had two planes of emulsion, and each plane of emulsion provided a measured segment of the particle's track.

"Bulk" type plates had 350 μm of emulsion on either side of a 90 μm supporting acrylic base and 95% of the mass of these plates was due to the emulsion. The benefit of a target made entirely of emulsion is that the neutrino interaction vertex itself is observable, the charged tracks resulting from the interaction are recorded in the emulsion at the point of their creation.

The other types of plates "emulsion cloud chamber" or "ECC" had a 1 mm steel sheet layered with 90 mm of emulsion on either side of either a 200 μm or 800 μm acrylic sheet. These two types were called ECC200 and ECC800 respectively. In these plates the majority of the mass comes from the steel sheets and this is where neutrino interactions were most likely to occur. These plates are much more dense that the bulk type and a greater number of neutrino interaction result for a given volume of detector and at a much lower cost.

The layers of ECC plates form a sampling detector, recording trajectories in intervals of 200μm, 800μm or 1mm. In these plates it is unlikely that the decay position of the tau is seen, rather the daughter track and the parent tau track will have to be identified by projection to a common decay position. It is also possible that a tau created by a ν_τ interaction in the steel will decay before it passes a single layer of emulsion and is hence never recorded. In these cases the tau can only be identified by the impact parameter of its daughter to the neutrino interaction vertex. Figure 5-1 shows the two scenarios for tau decay in ECC plates.

The emulsion plates were stacked to a depth of 7 cm in 8 different modules. Table 3-2 shows the composition of each of the target modules. A rigid aluminum target stand held up to 4 of the modules at once.

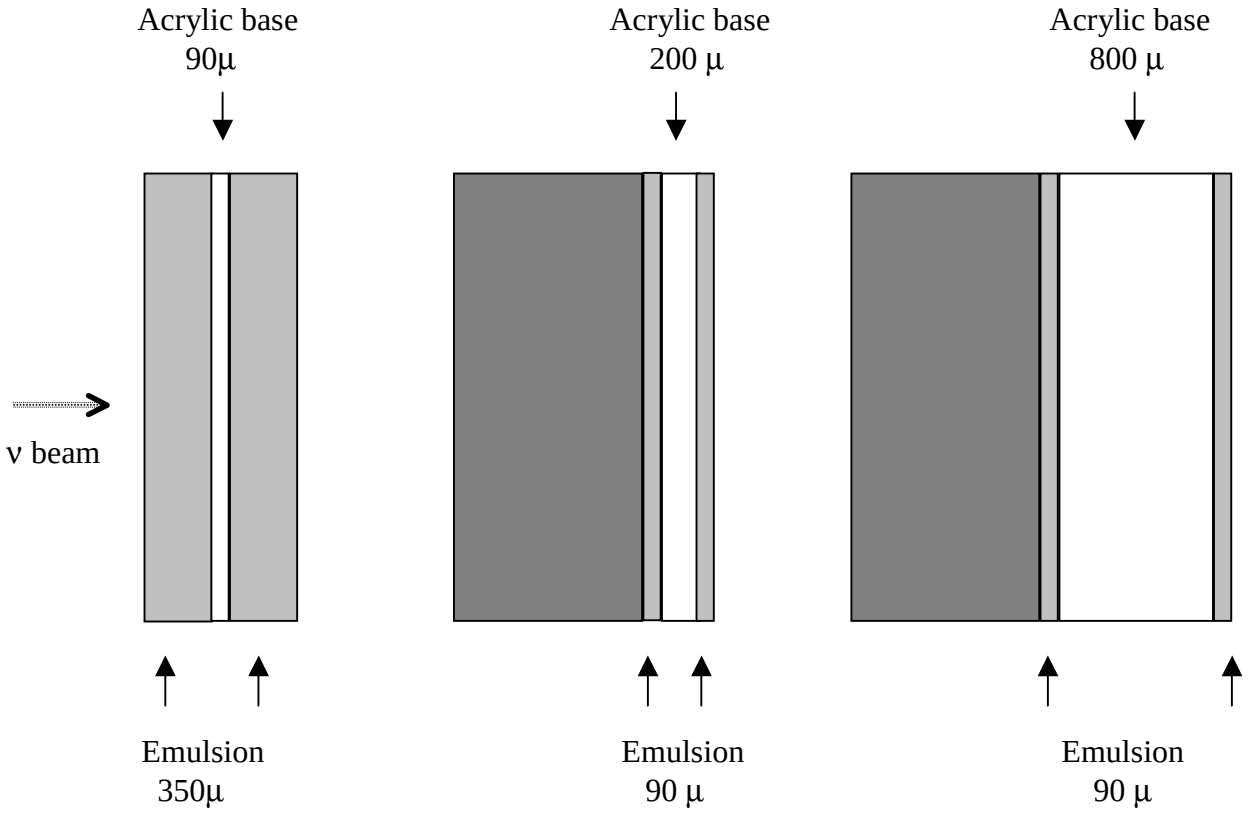

Figure 3-2 Emulsion plate configurations used in E872

The target stand was housed in a temperature and humidity controlled enclosure 36m downstream of the beam dump and past the muon shielding. The stand allowed the emulsion target modules to be removed and replaced while maintaining an accurate position reference to the neutrino beam. Within the target stand there were four stations along the beam direction for module placement. The spaces between the emulsion station

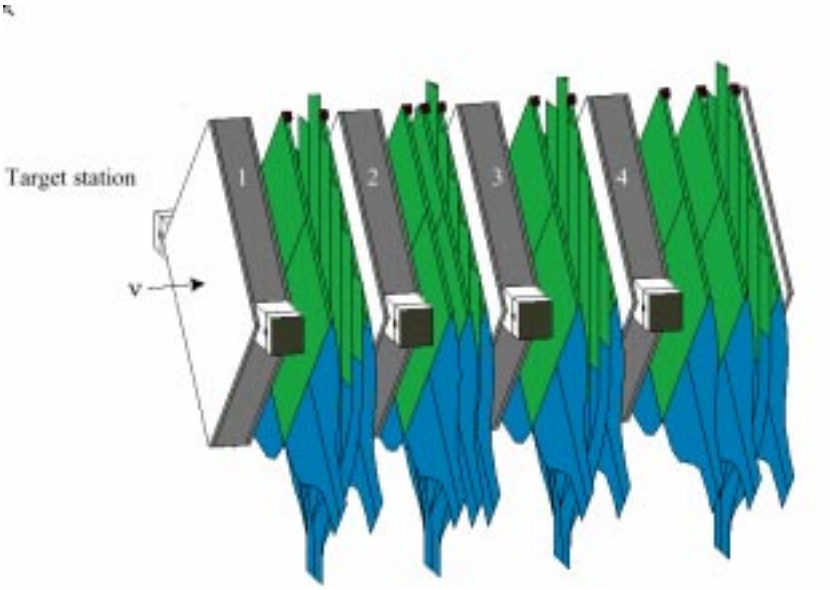

Figure 3-3 Orientation of emulsion target modules and scintillating fiber planes

and the area downstream of the last station contained the planes of the fiber tracker system. The positioning of the target modules and scintillating fiber planes are shown in Figure 3-3.

The composition and total mass of each target module is shown in Table 3-2.

Module	Sheet Composition	Period	Station	Mass (kg) ECC / Bulk / Total
ECC1	(47) ECC200	1-3	1	100.49 / 0 / 100.49
ECC3	(47) ECC200	1,2	3	100.49 / 0 / 100.49
E/B1	(21) ECC200 (30) Bulk	4	1	49.15 / 19.35 / 68.50
E/B2	(47) ECC200 (39) Bulk	3,4	2	42.12 / 25.15 / 66.70
E/B3	(47) ECC200 (33) Bulk	3,4	3	44.46 / 21.28 / 65.74
E/B4	(12) ECC200 (2) ECC800 (53) Bulk	2,3	4	36.71 / 27.73 / 64.44
B/4	(87) Bulk	4	4	56.10 / 0 / 56.10

Table 3-2 Composition and placement of the emulsion targets

3.3.2 Emulsion properties

Nuclear emulsion is similar to photographic film, consisting of a crystalline silver-halide salt suspended in a gelatin. E872 used the commercially available emulsion Fuji ET7C which contains silver-bromide salt. The make up of emulsion is shown in Table 3-3.

When a charged particle traverses a small crystal of silver-bromide a fraction of the salt molecules disassociate. The positions of the bare silver atoms form the latent image of the particle track, around which larger grains of silver grow when the emulsion is developed. The probability of a grain being formed during development depends on the initial size of the crystal. Unlike the surrounding gel, the silver grains which grow around the latent image sites are dark and thus a visible and measurable record of the particle's trajectory remains in the emulsion after development. As with photographic emulsion the image is fixed in place during development.

Element	Fraction (%)
Silver	45.4
Bromine	33.4
Carbon	9.3
Oxygen	6.8
Nitrogen	3.1
Hydrogen	1.5
Iodine	0.3
Sulfur	0.2

Table 3-3 Composition of Fuji EB-7C nuclear emulsion

The sizes of the developed silver grains depend on the development time as well as the size of the initial silver halide crystal. Typically silver-halide crystals sizes are sub-micron and the resulting silver grain are approximately 1 micron in diameter after development. The distribution of initial AgBr crystal diameters for the Fuji ET7C

emulsion used in E872 is shown in Figure 3-4. These were measured with a manual microscope and precision staging table.

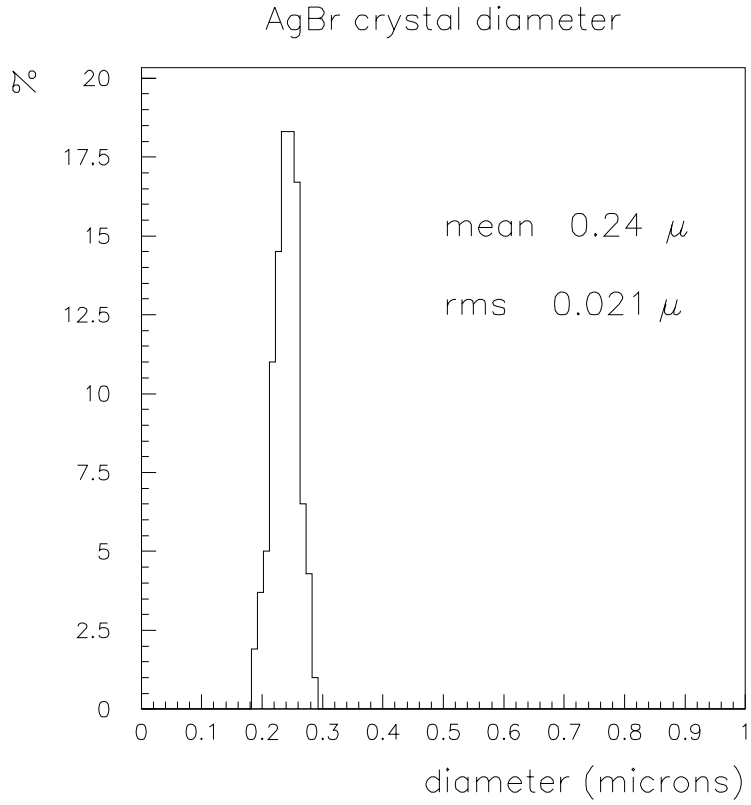

Figure 3-4 SilverBromide crystal diameter for Fuji ET7C emulsion

The spatial density of the grains that develop along a particles path is a measure of the sensitivity of the emulsion and the development process is adjusted to optimize this density. At densities below ~20 grains/100μm the efficiency of the automatic scanning procedure drops dramatically and cannot be used. The final grain densities for E872 were measured using the abundant background muon tracks. The distribution of densities for bulk and ECC800 were 28 ± 2 grains/100μm and ~20 grains/100 μm for ECC200 plates.

Silver bromide crystals may be displaced during the development process leading to a distortion of the image that is created. One cause of displacement is that a substantial fraction of the material in the emulsion is removed during development; the unexposed silver bromide salt which accounts for 50 % of the emulsion volume initially is dissolved

and removed from the gel. The thickness of the developed emulsion is thus approximately half of that which is exposed. This effect can be relatively easily corrected in analysis as the image of the trajectory record is only compressed in one dimension. However, distortions also arise from lateral movement of the silver bromide within the gel. During fabrication of the plates the emulsion is poured as a liquid onto the acrylic substrate. The emulsion does not dry evenly and the non-uniform surface tensions result in unequally distributed strains. When the emulsion is re-wetted during development the strain displaces the silver crystals within the gel and results in a local distortion of the image record. The method by which these distortions were found and treated are discussed in chapter 4.

3.3.3 Spectrometer

Figure 3-5 shows the layout of the detectors making up the downstream spectrometer.

The detectors were read out with a VME processor that gathered information from CAMAC ADCs and TDCs associated with the various elements. Signals from the detectors were recorded on 8mm tapes at a rate of ~500kB per second and the trajectories of charged particles making up the event were later reconstructed offline. The readout of detectors was triggered by combinations of signals from scintillation detectors and the electromagnetic calorimeter which indicated that there were charged tracks beginning within the emulsion target region.

The trigger system was composed of several scintillating counters designed to select events that had no upstream charged track and one or more high momentum charged tracks originating in the target region. Specific trigger criteria are discussed in section 4.1.1.

The veto wall was used to reject events that were caused by charged particles. It consisted of a double layer of 10cm thick 1.5 m tall scintillator counters read out on both ends by photomultiplier tubes. Each VETO counter had an efficiency of 95%, and the efficiency of both layers together was more than 99%.[29]

Three planes of scintillating counters were positioned within and just downstream of the emulsion target were used to identify charged tracks within the emulsion stacks.

The two planes of counters within the target hut (labeled T1 and T2) were vertically oriented planes of scintillating-fibers of the same type used in the fiber tracker. The light signals from these fibers were read out by Hamamatsu R5600 photomultiplier tubes. T1 was located downstream of the second emulsion module had eight segments, each four fibers deep and 8.75 cm wide. T2 was located downstream of the last emulsion module had nine segments of the same type as T1. The T3 trigger plane was downstream of the target hut and consisted of eight slabs of scintillator 1cm thick and 10 cm wide. The scintillator was attached to light guides 49 cm long and read out at both ends by Phillips 2262b photomultiplier tubes. The efficiency of each trigger counter was measured with background high energy muons and was better than 97% [29].

The scintillating-fiber tracker was used to project tracks back into the emulsion. It contained 107,000 SCSF78 500 μm diameter scintillating-fibers mounted in four stations, each one directly downstream of an emulsion module. The stations contain up 13 planes of fibers, each 1000 fibers wide extending slightly past the edge of the emulsion.

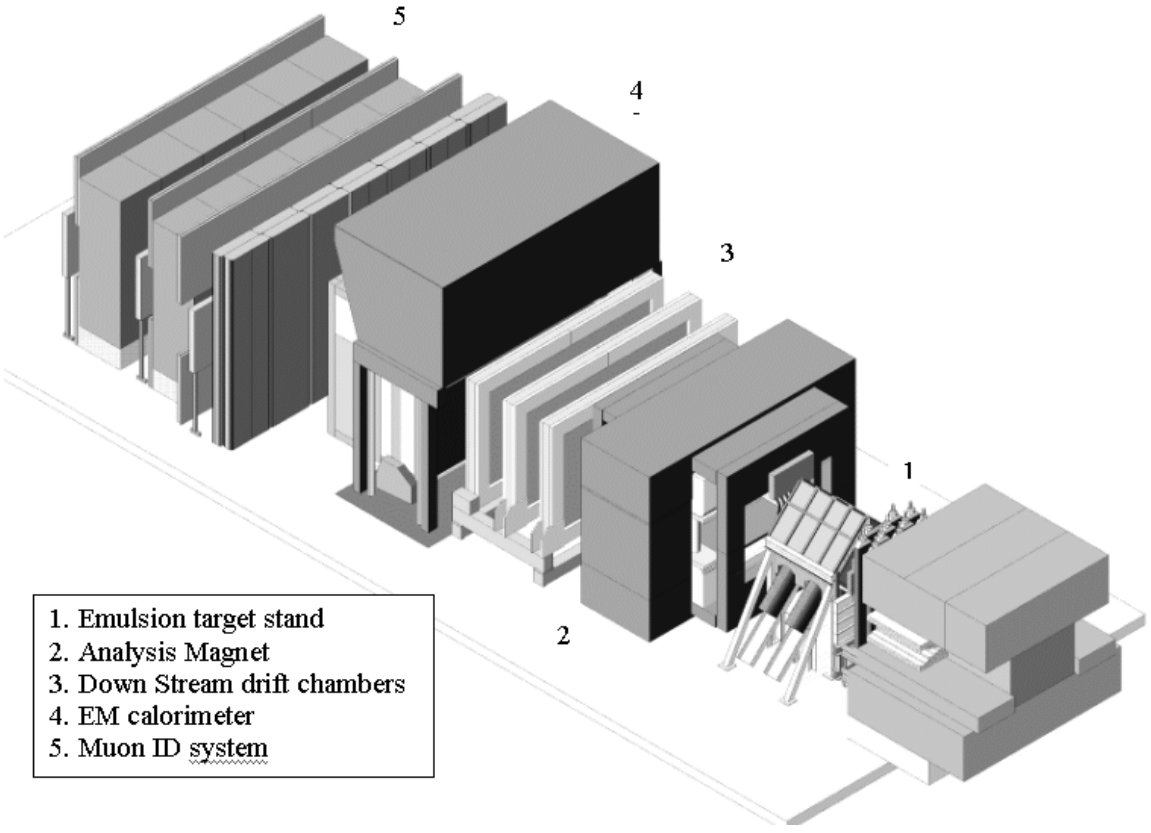

Figure 3-5 E872 detector elements

The detection planes were oriented vertically and $\pm 45^0$ with respect to the vertical (named X, U, and V respectively) Each U and V detection plane was two fibers deep and each of the four X planes was six fibers deep. The fibers were held rigidly on a flat support which is slightly larger in area than the emulsion target. Approximately 80cm of fiber was unsupported, extending past the end of the mounting plane, gathered into six bundles and attached to an image intensifier. The total length of the fibers is 1.3 meters and yielded ~4 photo-electrons when traversed by a minimum ionizing particle. The intensified and de-magnified images of the fiber bundles were recorded by CCD camera. Every sixth fiber was illuminated by an electro-luminescence plate during readout. The positions of the pixels in the event signal images were compared to those of the illuminated fiducial fibers during decoding and allowed for accurate position assignment of the signal.

The scintillating-fiber system was calibrated and aligned with high-energy muons. Figure 3-6 shows the distribution of the distance between scintillating-fiber hits and tracks reconstructed using a linear fit to all fiber planes. When fit to a Gaussian distribution the central peak of the distribution has a sigma of 170 μm. For tracks reconstructed using fibers in only one station of planes this corresponds to an accuracy of 0.5 mm when projected to the center of an upstream target module. When using scintillating-fiber tracks to find the target volume to scan, the energy of the track is not usually known, and the resolution may be significantly degraded by multiple scattering. For this reason only signals from the station directly downstream of the target module was used in the projection.

The spectrometer downstream of the emulsion/fiber target enclosure consisted of four drift chambers, an analysis magnet, a calorimeter and a muon identification system.

The first drift chamber spans 1.1m by 0.8m and was located in the aperture of the analysis magnet directly downstream of the emulsion target enclosure. Each of its three views (oriented at 0^0, $+3.5^0$- and -3.5^0) had 16 cells along the x direction with six sense wires within each cell. Within each cell the individual hits were combined to define a plane parallel to the sense wires. Three dimensional tracks were reconstructed from the three stereo views. This drift chamber had two primary purposes: to aid the

scintillating-fiber tracker in track reconstruction for locating vertices in the most downstream emulsion station and to provide a means to match tracks from the fibers to tracks reconstructed in detectors downstream of the analysis magnet. The resolution of an individual sense wire was measured with muons to be ~200 microns and the angular resolution set of hits within a single cell was 2.5mr.

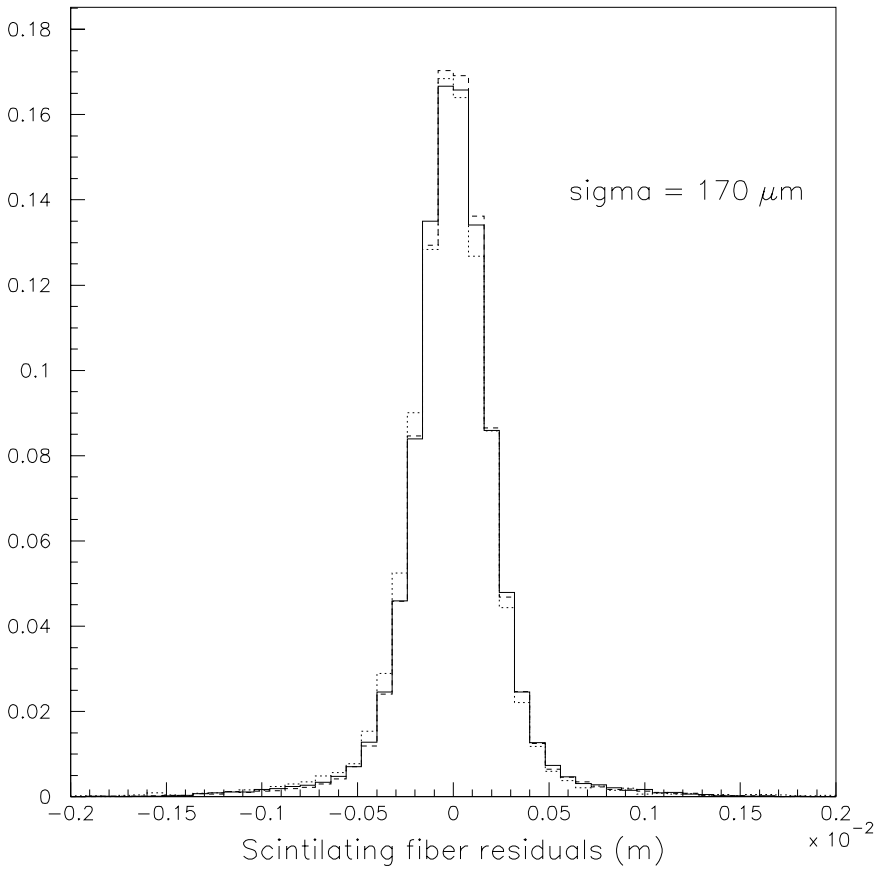

Figure 3-6 Scintillating-fiber residuals for U, V and Z planes.

The analysis magnet had an aperture of 2m x 1.7 meters. Attached to both upstream and downstream faces were mirror plates to contain the magnetic fields which would otherwise degrade the performance of the adjacent photomultiplier tubes and distort the image of the scintillating-fiber tracker's CCDs. The field was mapped using an automated tracker with three orthogonal hall probes. The integrated $\vec{B} \cdot d\vec{l}$ along a track parallel to the beam is 0.75T·m giving a transverse momentum kick of 225MeV/c to a singly charged particle.

Just downstream of the analysis magnet was a set of three large drift chambers. The tracks recorded in the drift chambers allow for momentum measurement and for matching of tracks from the vertex to hits in the calorimeter and muon identification system. Drift chamber tracks were also used in event selection: a down steam track projected to the emulsion volume was an indication of valid trigger. These drift chambers had an aperture of 3m x 2m, and were separated by 80 cm along the beam line. Resolution for each plane, also measured with residuals from fit muon tracks, was 300 microns. The angular resolution for fitted tracks was ~250 μrad.

Downstream of the last drift chamber an electro-magnetic calorimeter. It was made of 426 lead glass and scintillating glass blocks covering an area of 4 meters wide and 2 meters tall. The central region near the beam had 7.5×7.5.cm rectangular blocks of scintillating–glass 20.6 radiation lengths deep. The outer region had 15cm ×15 cm blocks that were 16.4 radiation length deep. A sample of ten of the calorimeter blocks were calibrated in a test beam at Brookhaven Nation Lab using pions, electron and muons with energies from 1- 5GeV, the energy resolution was $20\%/\sqrt{E}$.

The final element of the spectrometer was the muon identification system. It consisted of three walls of ranging steel and three wall of proportional tube detectors that were each 5m wide and 3m tall. The total range of the steel to the third wall was ~2.7 GeV. Each wall of detectors had an array of horizontal and vertical proportional tubes covering the regions of low muon flux.. The proportional tubes were 4 cm wide square aluminum tubes filled with Argon. The efficiency of each wall of proportional tube is estimated to be ~97%; the only inefficiency was due to the inactive regions corresponding to the walls of the tubes.

4 Data collection and neutrino interaction data set

E872 recorded data for an total 3.56 **x** 10^{18} protons on dump during the fixed target period of operation in 1997. Protons were delivered in spills of approximately 5×10^{12} which lasted 20 seconds and came at a frequency of 1 per minute. Data were recorded during four different run periods, each with a different configuration of the emulsion modules. In all eight different modules were exposed to the neutrino beam. Table 4-1 shows the distribution of the emulsion modules and their exposure.

The data collected from the exposure were 6.3 million triggered events that occurred in the emulsion target region. Neutrino interactions were selected from this set of recorded data by patterns of reconstructed tracks and detector signal distributions which had the topology of a neutrino interaction: no identified particle upstream and one or more charged particles traveling downstream. Tracking information from the scintillating-fiber tracker was used to predict interaction positions in the emulsion modules and define a volume of emulsion to search for the event. The emulsion was scanned optically and information from the scan volume was then used to reconstruct a precise vertex of the coming from the neutrino interaction vertex. A second scan of the

emulsion data in a volume centered around the located neutrino interaction vertex was later performed and used for the tau decay search.

Run Period	1	2	3	4
Number of protons on dump	5.4×10^{16}	4.4×10^{16}	1.03×10^{17}	1.55×10^{17}
Number of triggered events	1.0×10^{6}	0.8×10^{6}	2.1×10^{6}	2.7×10^{6}
Station 1 target module	ECC1	ECC1	ECC1	E/B1
Station 2 target module	-	-	E/B2	E/B2
Station 3 target module	ECC3	ECC3	E/B3	E/B3
Station 4 target module	-	E/B4	E/B4	B4
Total target mass	201 kg	268 kg	297 kg	257 kg

Table 4-1 Emulsion module exposure over the four run periods.

4.1 Spectrometer data

4.1.1 Trigger

Neutrino event selection began at the hardware level with a trigger system designed to identify events with the general characteristics of a neutrino interactions: no upstream charged track and one or more high momentum charged tracks originating in the target region. Events satisfying this criteria triggered the data acquisition system and information from all spectrometer elements were recorded to tape. Events having a charged track upstream of the emulsion region were identified and rejected by a two meter wide veto wall directly preceding the emulsion target stand in the beam line. A neutrino interaction typically has ~5 charged primary particles. The number of tracks viewed in the trigger counters and scintillating fibers is generally much higher due to secondary interactions of the primary particle and photon conversion.

The segmentation of the trigger counters gave the ability to recognize charged tracks downstream of the interaction vertex that were above a minimum angle and below a maximum angle with respect to the beam. This allowed for the rejection of penetrating muons which were typically with a few milliradians of the beam and would not fulfill the

minimum angle. An adjacency in these segmented counters was defined a hit recorded in any upstream segment and a hit in the neighboring segment in the next downstream trigger plane. A schematic of an event with two adjacencies is shown in Figure 4-1.

The primary trigger requirement was more than one adjacencies in an event. This trigger type had a rate of ~3Hz throughout the data taking period. A second trigger type, requiring only a single adjacency and a hit in the central region of the calorimeter, was

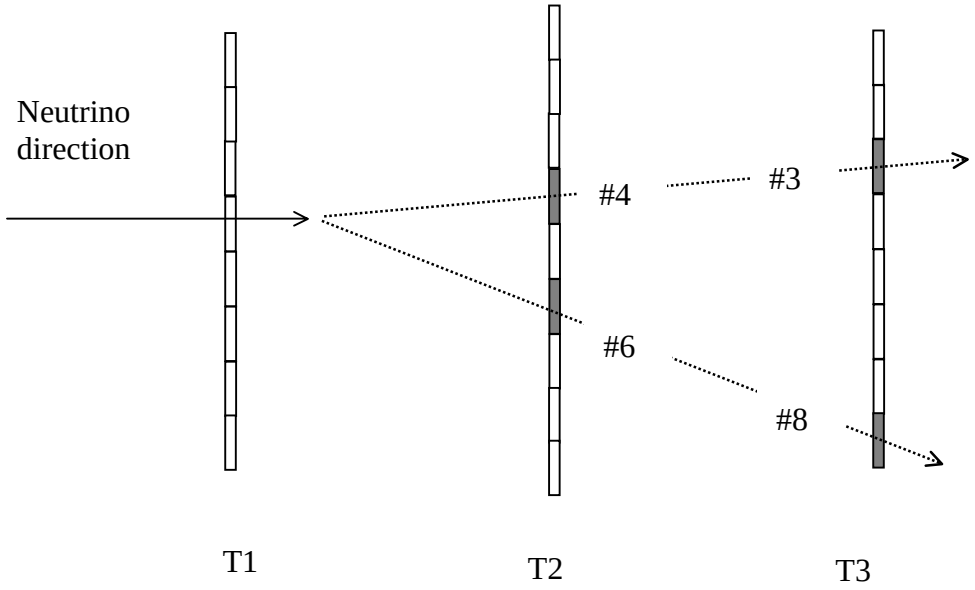

implemented during run periods two and three. This second trigger allowed for events having only one charged track beginning in the emulsion region to be included in the data record and added less than 10% to the total trigger rate.

Figure 4-1 Schematic of segmented trigger. The two charged products of a neutrino-nucleon interaction pass through trigger counters and fulfill the primary trigger requirement.

4.1.2 Data acquisition

Once the spectrometer had been triggered, the signals from the spectrometer elements were digitized and recorded to 8mm data tapes. Information about the number of protons in the spill and upstream beam position monitoring measurements were included in the recorded data. A total of 325 data tapes were written.

The trigger counters and drift chambers were read out by CAMAC controlled LeCroy TDCs. The muon identification proportional tubes, EM calorimeter and

scintillating-fiber tracker CCD information was digitized by CAMAC controlled ADCs. Those for the scintillating-fiber system were custom built eight-bit flash ADCs. The data acquisition system had an input limit of 32MB/second and this was dominated by large events in the SFT in which many fibers had signals and thus contained much information.

The majority of events written to tape were backgrounds to the neutrino interactions. Principally they were events where a muon interacted in the heavy material of the emulsion target stand producing charged particles that entered the target region from the side. Offline track reconstruction software and visual selection on an interactive event display were used to select neutrino interactions from the 6.3 million events recorded on tape.

4.1.3 Offline neutrino selection

The first step in neutrino interaction identification was an offline selection based on data from the scintillating-fiber tracker, drift chamber and EM calorimeter to select possible neutrino like interactions and to reject background events. If any one of the following three selection criteria were satisfied ,the event was selected for further analysis:

1) The event had one or more of the drift chamber tracks point back to a 50 cm by 50 cm area in the most downstream emulsion module
2) The event had an energy greater than 30 GeV as measured in the calorimeter
3) The event had vertex formed by tracks in the scintillating-fiber tracker U view and a vertex formed by tracks in the scintillating-fiber tracker V view, both of which were in the same emulsion module.

These criteria were filed by ~10,000 events out of the 6.3 million trigger as possible neutrino interactions.

4.1.4 Visual selection and interaction vertex prediction

The set of events remaining in the sample after offline selection was still contaminated with many background events. Inefficiencies in the reconstruction of spectrometer tracks and interaction vertices in showering events, as well as the inability of the software to recognize tracks originating from outside the target region necessitated a visual evaluation of each event. All events passing the offline selection were refit and evaluated by teams of physicists on a graphical event display. Refitting involved the adding or removing of individual hits in the scintillating-fibers and drift chambers along tracks that had been incorrectly omitted or included by the software reconstruction. Often in instances where hit density and track density was high the software would assign hits to a neighboring track. The refit tracks suspected of being the direct products of an interaction were then used to calculate an vertex position within an emulsion module by finding the most likely common position of origin. The following selection criteria were then applied to further refine the data set after interactive refitting;

1) The event had 2 or more high momentum tracks or particle showers pointing to a vertex.
2) The vertex was within an emulsion target module
3) The total event energy was greater than 5 GeV as measured by the calorimeter or by the total momentum of charged tracks passing through the analysis magnet.

Four teams of two physicists selected a total of 892 events as neutrino interactions.

The purpose of the interactive event refitting was not only to select neutrino interactions but also to define a precise neutrino interaction vertex position. An accurate prediction of the neutrino interaction position is needed to increase the likelihood of finding he interaction vertex in the scanned volume. Making an accurate prediction was often difficult due to multiple scattering and shower development in the emulsion modules. It was more likely for the software to erroneously assign hits in the areas of high hit density that were the result of a shower. Typically a vertex prediction was made with only the most well defined, highest-momentum reconstructed tracks in the

scintillating fiber tracker and resulted in a vertex with an uncertainty of 5 mm in the transverse direction and 1 cm in the beam direction.

4.2 Emulsion data

Once a prediction of the neutrino interaction vertex has been made the developed emulsion plates were scanned in a region surrounding the predicted position. The size of the volume scanned depended on the uncertainty in the vertex prediction. Typically the dimensions of the scan volume were 2.6 mm perpendicular to the beam and up to 1 cm along the beam direction. Approximately 25 emulsion plates were scanned for each event. Tracks were reconstructed by linking emulsion track segments found in successive plates. This was done for all track segments found throughout the entire scan volume.

4.2.1 Emulsion scanning procedure

The emulsion sheets were individually developed and scanned using automated track selecting microscopes originally developed for the CHORUS experiment[30,31]. The entire sheet of emulsion is positioned with a ball screw driven XY stage under a microscope attached to a CCD camera. At every sheet position the image of the grain pattern is recorded at sixteen different depths throughout the emulsion on each side of the sheet's plastic base. The focal plane of the microscope is moved throughout the first 100 microns of the emulsion adjacent to the supporting base. These sets of digitized images were processed by dedicated electronics programmed to recognize grain positions that are collinear through successive focal planes within each layer of emulsion. The angle and positions of the three dimensional lines found by the processor are recorded as track segments and output to data files. Large areas of emulsion are scanned by moving the emulsion and repeating the process in overlapping fields of view. In the Bulk plates, the emulsion layers are 350 μm and therefore in these plates 250μm of emulsion is not used by the automated scanning system to create segments. The remaining emulsion can still be scanned by eye to , for example, verify an neutrino interaction.

The readout time for the track selector decreased over the course of analysis due to improvements in the processors used for track recognition and in CCD camera

speeds. The latest iterations used for this analysis, called the UTS for "ultra track selector", reads out ~1cm^2 of emulsion on both sided of an emulsion plate per hour and a typical scan volume for a single event can be completed in approximately six hours.

The data for one emulsion sheet are combined with those of adjacent sheets to give a record for an entire scan volume. The track segments in each sheet are connected to those in other sheets to form longer reconstructed tracks. The length of these reconstructed tracks is only limited by the number of emulsion sheets used and connecting segments through an entire emulsion stack is possible. The accuracy of the recorded segments is found by computing the position and angular deviations to reconstructed tracks. Figure 4-3 shows that resolutions of less than 1 micron are typical for individual segments and angular resolutions for individual segments are generally < 3 mrad

4.2.2 Emulsion track reconstruction

The linking of the track segments is accomplished by projecting each segment onto the next plate and searching for a segment that matches in both position and angle. The process begins with the most downstream emulsion plate and the search area in the next upstream emulsion plate is defined by a cone along the direction of the original segment. The opening angle of the cone is the rms scatter for a 100MeV/c singly charged particle traversing the material through which the projection is made. If no matching segment is found the search moves to the next downstream plate. If more than one segmet was missing, the upstream and downstream sections are reconstructed as two separate tracks. If more than one segment is found within the area defined by the cone, the one matching closest in position is used. The projections are continued upstream until no match is made or the track leaves the upstream boundary of the scan volume.

This method of linking segments into tracks is very efficient: the position and angular resolution of each segment is high enough that the possibility of linking unassociated segments is small. The efficiency of track linking is found from the fraction of linked tracks which have missing segments, it is defined as the total number of missing segments in all tracks in an event divided by the total number of tracks. Since the vast majority of tracks in the emulsion are penetrating it is assumed that all tracks should

have segments in every plane of the scan volume. Figure 4-2 shows the efficiencies for a random selection of tracks taken from the emulsion records of all the located neutrino interactions.

Once the tracks have been linked a local alignment of every segment in each plate is preformed to correct for the strain distortions. The local alignment is accomplished by using a set of adjacent background muon tracks.

The overwhelming majority of the tracks reconstructed in the emulsion are due to high energy muons that traverse the entire emulsion module and are easily identified. Since they are high energy, their recorded tracks are essentially straight. The alignment is accomplished by computing the average angular and position residual of penetrating tracks that are within a $100\mu m \times 100\mu m$ area surrounding the segment to be aligned. These high momentum muon tracks are fit to a straight line and the angular and position deviation from this fit is found for each plate containing. This is repeated for all the penetrating tracks near the segment to be aligned, the average angular and position deviations between the segments on the penetrating tracks and the straight line fits are used as the position and angular distortion for the area. The measured position and angle of the segment in question is then corrected with the average deviations.

The set of aligned segments and reconstructed tracks in the entire region surrounding the predicted vertex comprise an volume scan data set for each of the events. Figure 4-3 shows the position deviations after the alignment was completed on all the emulsion segments.

4.2.3 Emulsion vertex location

Once aligned, the tracks belonging to the neutrino interaction vertex must be identified out of the more than 100,000 tracks in each scanned volume. The emulsion vertex is first located offline using the recorded emulsion scan data and then confirmed with a manual scan using a conventional microscope to view the tracks in the emulsion directly.

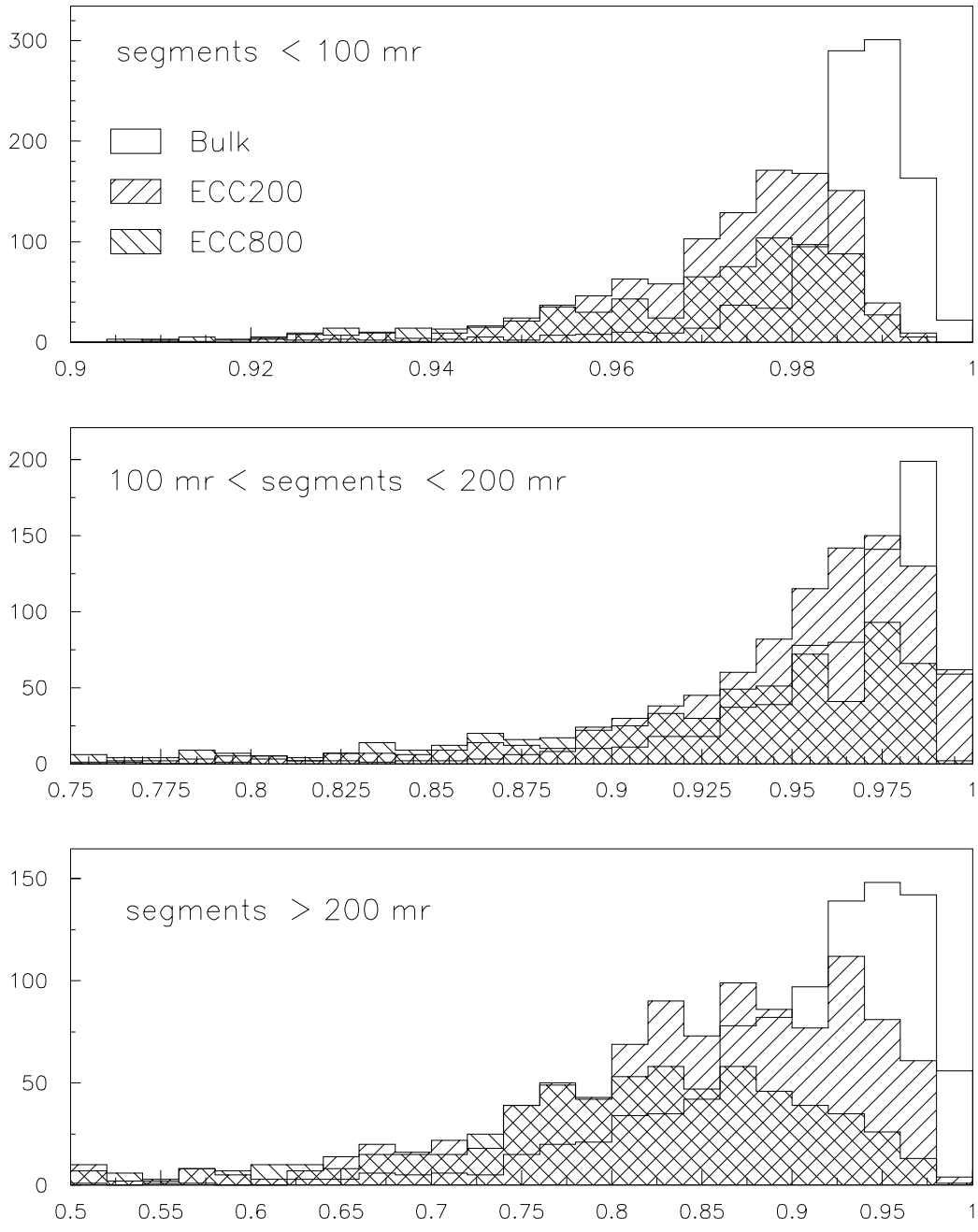

Figure 4-2 Efficiencies for Bulk, Ecc200 and ECC800 emulsion planes. The efficiency is the ratio of segments missing to the total number of tracks.

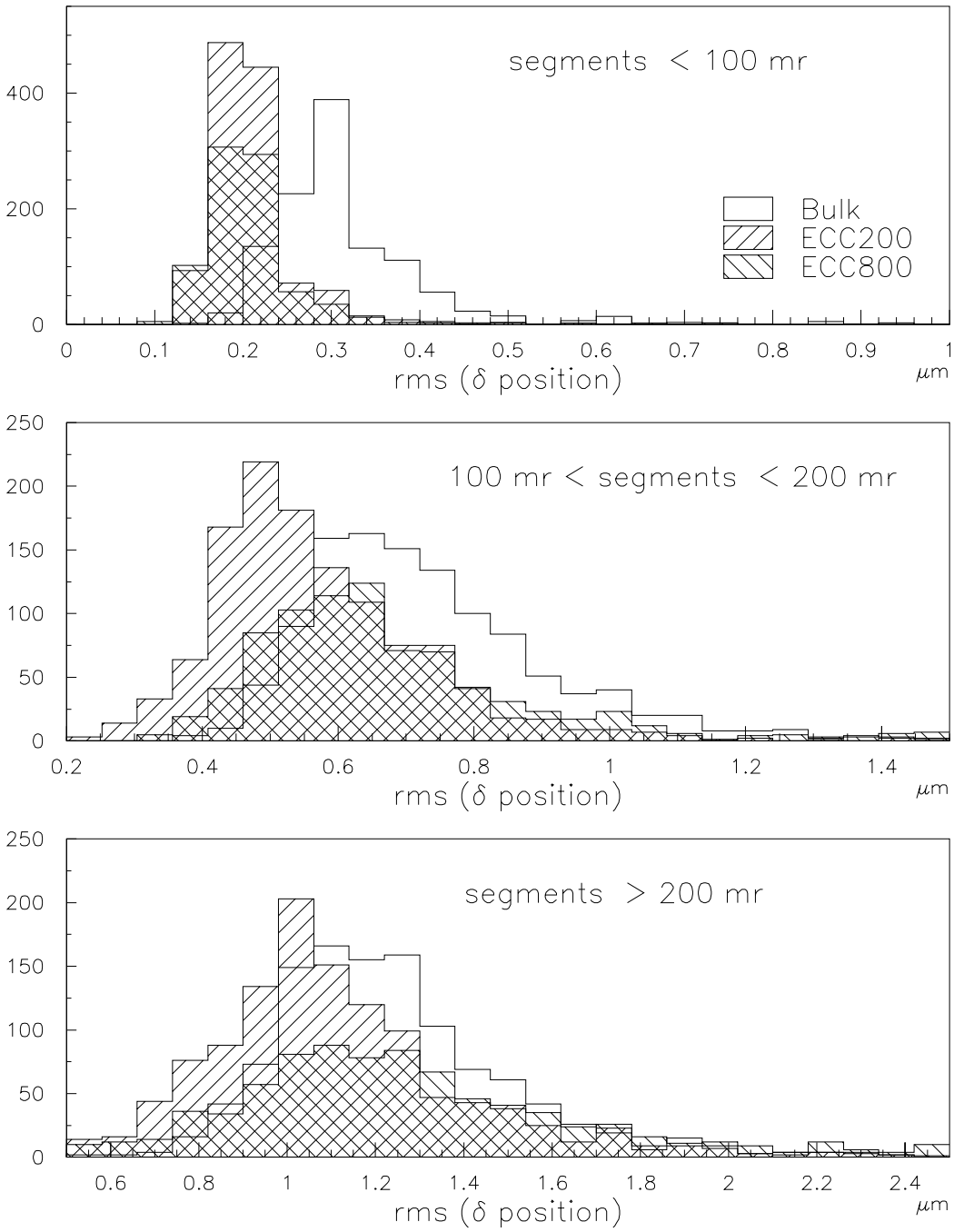

Figure 4-3 RMS deviations from segments to linked emulsion tracks for every emulsion sheet Neutrino interaction location.

4.2.4 Neutrino interaction location

The neutrino interaction vertices are located by finding pairs of non-penetrating tracks which have an impact parameter less than a threshold value that depends on the emulsion data quality. This is typically 5 μm. For an interaction vertex with three or more tracks, several pairs are found at the same intersection position. Simply finding a vertex with three or more tracks usually guarantees that the correct interaction vertex was located since the probability that a random association of three tracks forming a vertex is small. The probability is estimated from the observed density of two track vertex pairs which is ~.03 pairs per mm^2. This corresponds to density of $\sim 8 \times 10^{-8}$ per mm^{-2} for random three track vertices or, equivalently, 10^{-5} per emulsion scan volume.

The tracks from a vertex are then projected to the scintillating-fiber tracker where a search for confirming hits or two-dimensional lines is carried out. A small fraction of neutrino interactions result in only two charged tracks. A tighter impact parameter cut of ~2.5 microns is applied to the track pairs in a search for or these events.

Once the neutrino interaction is found offline, a manual microscope above a precision stationing table is used to search for track segments missed by the automated scanner. This has been the traditional method of by finding particle tracks in emulsion. A trained scanner would use a microscope to search the emulsion and locate individual grains which lined up to form tracks.

For each track forming the vertex an area one and two plates upstream of the vertex is scanned in this way. This step is to double-check that the vertex is the result of a neutrino interaction and not caused by an incoming charged particle. It also checks that the vertex contains no penetrating tracks that may have been mis-linked by the track reconstruction software. The efficiency of a human eye scan is limited only by the efficiency of the emulsion record, even with very poor grain density it is essentially ~100%.

In all total of 268 neutrino interaction vertices were located and verified in the emulsion by a manual eye scan.

4.2.5 Decay volume data.

After the neutrino interaction vertex is confirmed, a second scan centered on the interaction vertex position is performed to ensure the highest data quality. In this scan a volume 2.6 x 2.6 by 10mm^3 centered on the vertex is scanned and the resulting data file is used for the tau decay search. This scan ensures that all the tracks of the event are included and that they were followed for a useful length; a particle coming from the interaction at an angle of 400 mrad with respect to the neutrino beam is tracked for a minimum of 5mm in a decay volume scan. These scan volumes undergo the same track reconstruction and alignment as the location scan volumes.

4.2.6 Data quality check

Before a search for the tau was preformed, a selection based on alignment was done so that the data in the emulsion decay volume scans are all of similar quality. The requirements that define a good event are that all plates within the volume are globally aligned to less than 1 μm and that no plate slipping occurred. In some cases during exposure, a shift in the vertical direction was caused by imperfect adhesion between the plates. This slipping problem was more apparent in the relatively dense ECC modules.

Plate slipping made it difficult for the track reconstruction software to correctly link penetrating tracks. All penetrating muon tracks left in the emulsion after the slip occurred could be reconstructed throughout the entire volume whereas those from muons occurring before the slip were only reconstructed on either side of the dislocation. These two sides were not linked together due to the relatively large discontinuity, often greater than 10 microns.

Of the 246 located neutrino interactions, 203 had decay volume data with the required alignment and no plate slippage dislocations within the 1 cm depth. These made up the data set of neutrino interactions which was searched for evidence of a tau particle.

5 Tau event selection

The 203 identified events selected from the decay volume data set include all types of neutrino interactions. The ν_τ charged-current interactions were selected from these. Lepton number conservation dictates that the primary products of a ν_τ charged-current interactions must include a tau and no other lepton. Thus, the defining characteristics of a ν_τ charged-current interactions are the presence of a tau particle coming directly from the primary neutrino-nucleon interaction vertex and the absence of either a high-energy muon or electron.

The identification of the tau is through its decay and criteria placed on events to select tau events were based on kinematics of the decay. The tau will decay within a few millimeters of the primary interaction vertex and its decay products will appear as tracks in the emulsion plates downstream. A majority (~85%) of the tau's decay modes result in only one charged particle and this allows the tau to be identified by the topology of single charged decay. For ν_τ energies in this experiment, the average decay length of the tau's produced is 2.2 mm and the average angle between the tau and its charged daughter is 55 mrad

Tau decays can be separated into two distinct cases: the first is where the tau decays before it is tracked in the emulsion, and the second is where the tau lasts long enough to be tracked in at least one emulsion plane.

The first case is most likely for events that occur in the ECC detectors which have a greater distance between tracking planes: in these the tau may travel for up to 1mm to before it reaches an emulsion plane where it can be tracked. If it decays before it reaches an emulsion plane, only its daughter tracks can be recorded. The daughter track will not project back to the primary vertex like the other particles from the neutrino interaction. These types of decays are called 'short' and are expected for 25% of tau decays in the target. They are shown schematically in Figure 5-1.

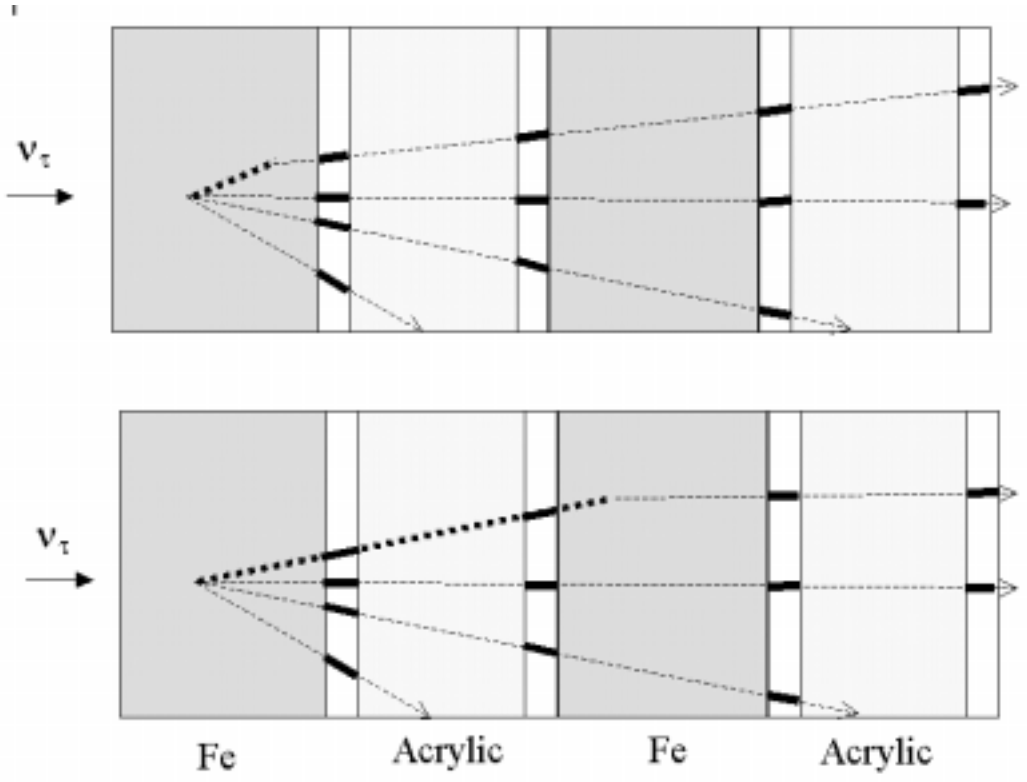

Figure 5-1 Schematic of short (top) and long (bottom) tau decays.

In the second case the tau reaches an emulsion plate and its recorded track projects back to the interaction vertex. Further downstream the track will be kinked where the tau decays. The downstream portion of the track is due to the daughter particle which has a different trajectory than the original tau. Tau events of this type are denoted

'long' and are shown schematically in the bottom of Figure 5-1. About 75% of the tau decays in the emulsion modules will have this 'long' decay topology. It is interesting to note that the 'long' events found in this experiment have the first ever recorded tracks of the tau-lepton.

The two types of tau events, 'short' and 'long' require two different types of analyses with different systematic effects. The analysis described in this thesis is restricted to 'long' events.

Two methods were used to find the 'long' events in the emulsion data set, both of which rely on finding a kink in a primary track. The first method assumes that the parent track and the track of the daughter were reconstructed separately and were identified as distinct tracks. The second method found small angle kinks (less than ~10 mrad) in the cases where and the parent and daughter were reconstructed as a single track.

The first method proceeds by examining all tracks from the primary interaction vertex that stop within the scan volume. All tracks that start in the next emulsion plate downstream are checked to see if they intersect the stopping primary track. An intersection was defined as the projection of the two tracks coming within some minimum distance that is determined by alignment and track reconstruction accuracy. This requirement on the distance of closest approach is usually less than 1 μm. Events in which there is a stopping track from the interaction vertex intersecting one and only one downstream starting track were considered potential single-charge tau decays.

The second method found kinks in parent-daughter pairs that have previously been linked together as a single track This mis-linking is possible in instances when the decay angle is small. This method proceeds by breaking all primary tracks into two parts. The upstream and downstream parts were fit separately to a straight line and the result was compared to the original fit. If the fit improved after separation and the angle between the two lines was greater than a minimum acceptable value, the two sections are reclassified as two separate tracks. The minimum angle for selecting kinks is discussed in the next section. All primary tracks are separated between every pair of segments and tested in this way.

5.1 Tau event selection criteria

Several *a priori* criteria based on the properties of the tau and knowledge of the detector were applied to the kinks to identify ν_τ charged-current interactions. The tau selection criteria applied to the events that have kinked tracks are:

1. There is no high energy electron or muon track originating from the interaction vertex.
2. The parent track is less than 5mm. in length.
3. The angle of daughter track with respect to the parent track is greater than 10 mrad
4. The impact parameter of the daughter track to the neutrino interaction vertex is less than 500 microns
5. The daughter track momentum is greater than 1GeV /c
6. The transverse momentum of the decay is greater than 250 MeV/c

Each of these selection criteria is discussed below.

Primary lepton identification

Any neutrino interaction producing an electron (muon) is by definition a ν_e (ν_μ) charged-current interaction and therefore cannot be a ν_τ interaction. Muons are identified by hits in the MID which are associated with a track projected from the primary vertex. Electrons are identified by their shower development or by the EM calorimeter signal.

If a track had hits in at least four of the six planes of the MID within three sigma of a projection using emulsion and drift chamber data, it is tagged as a muon. The MID system hodoscope had a detection efficiency near 97% and Monte Carlo simulation of ν_μ charged-current interaction showed that the geometrical acceptance was 63% for primary muons.

Electrons were identified by either the onset of a electromagnetic shower in the emulsion or a minimum of 5 GeV of energy in the calorimeter associated with a primary track. The start of an electromagnetic shower is easily identified in the emulsion: e^+/e^- pairs are produced adjacent to the primary electron. Their tracks begin within a few microns of the original electron's and the trajectories of both the electron

and the positron are of both is essentially along the primary electron's path. Simulation shows that the average distance form the original electron is 6.7 μm a the average angular deviation is 4.4 mrad. For each candidate tau event fulfilling the rest of the selection criteria, all primary tracks are followed to the end of the emulsion stack to search for e^+/e^- production. To do this the emulsion surrounding each track is scanned in all of these downstream planes and this data is used to search for the onset of a shower. The efficiency of this method depends on the number of radiation lengths remaining downstream of the interaction vertex within the emulsion module. Interaction in the upstream ends of the modules have more material remaining downstream leading to a higher probability of the shower being identified. For the 203 events in the data set, the average amount of material downstream of the interaction vertex is $\overline{X}$ = 0.96 and the probability of pair production occurring before the end of the module is 70%.

Electromagnetic showers were also identified in the scintillating fiber tracker. Showers there appeared as a dense concentration of hits. An electromagnetic shower could an be identified unambiguously , however, it was often difficult to assign the shower to a specific track in the emulsion. This happened when there was more than one track from the vertex pointing in the direction of the shower. However, in the cases where all primary emulsion tracks from the interaction vertex were well isolated, it was possible to use a shower in the fibers to identify the primary electron .

The electromagnetic calorimeter was also used to identify events with electrons. Primary electrons were identified by linking emulsion tracks with scintillating fiber tracks and downstream drift chamber tracks that were associated with high signal regions in the calorimeter.

Tau decay length selection

The decay length is defined the distance between the position of the neutrino interaction vertex and the intersection of the parent track and the daughter track. The intersection position is found by projecting a straight line fit of the last three segments of the parent track and a fit of the first three segments of the daughter track. Only three segments are used reduce any error caused by multiple scattering. The maximum accepted decay length is chosen to be 5mm which is half the length of the decay scan

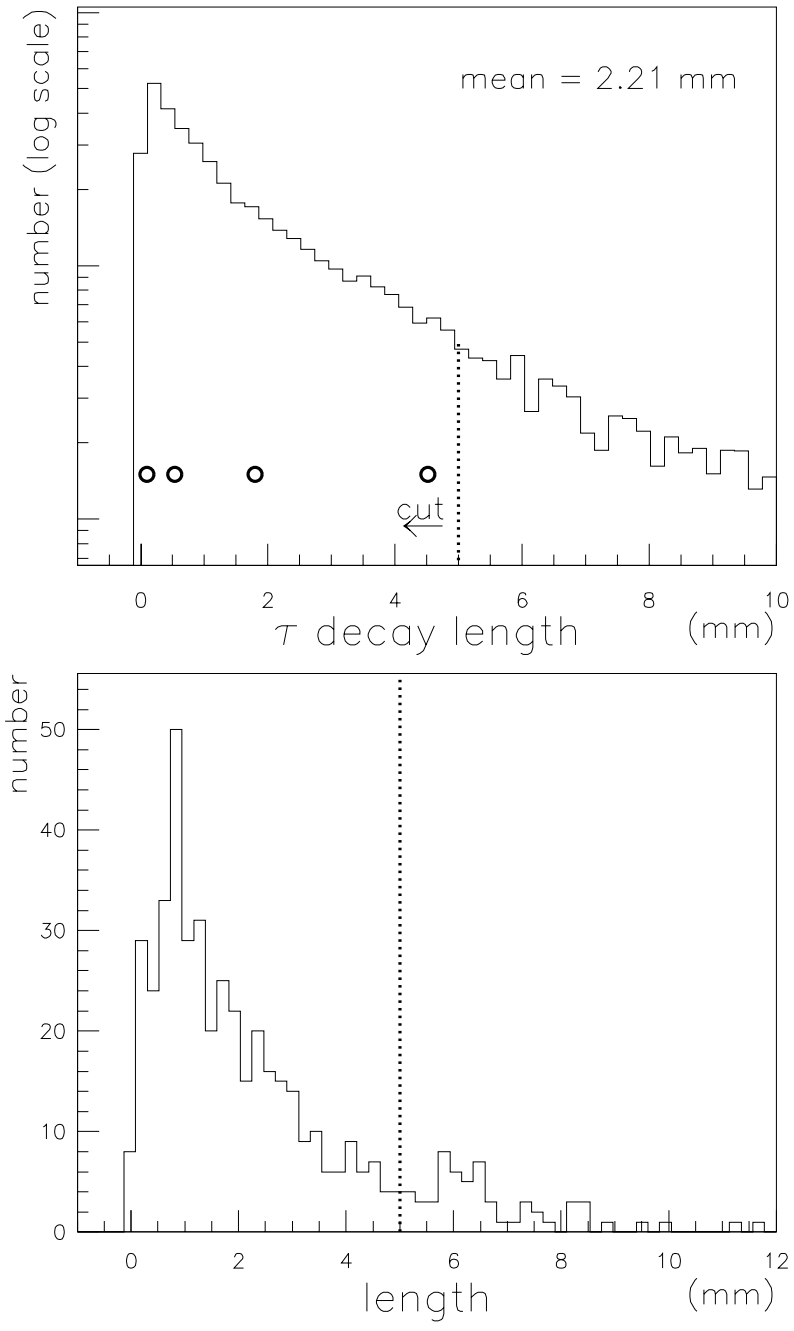

Figure 5-2 Top: Decay length distribution for taus from simulated ν_τ interactions. Also shown are the values for the four events which pass all selection criteria. Bottom: Distribution of lengths for all kinks found in the data set.

volume. A Monte Carlo simulation shows that 81% of the all tau decays have lengths shorter than 5 mm. Figure 5-2 shows the distribution of decay lengths for the taus in Monte Carlo generated ν_τ charged-current interactions.

Tau track -daughter track angle selection

The angle of the daughter track with respect to the tau track is calculated using a straight line fit of the last three segments of the parent track and the first three segments of the daughter track. In the cases where the parent track is less than three segments in length the vertex position is included in the fit. In order that the selected kinks are well defined, a minimum angle of 10 mrad is required .

This criteria selects approximately 84% of tau decays. Figure 5-3 shows the distribution of decay angles for the single charged tau decays.

Daughter track - interaction vertex impact parameter selection

The impact parameter of the daughter track is calculated by projecting it back to the neutrino interaction vertex. The shortest distance between the projected daughter track and the tau's initial position is a Lorentz invariant measure of the tau lifetime. Selecting events where the impact parameter is less than 500 μm corresponds to 5.7 mean lifetimes of the tau. This selection retains 97% of tau decays. The distribution of impact parameter for simulated ν_τ interactions is shown in Figure 5-4.

Tau daughter momentum selection

The momentum of the daughter track is found from either the deflection of the track by the analysis magnet or, in the case where the track does not pass through the magnet, by the multiple scattering in successive emulsion plates within the module.

Requiring a track to have momentum greater than 1 GeV/c retains 96% of simulated tau events as can be seen in that shows a distribution of daughter momenta for simulated single charged tau decays Figure 5-5.

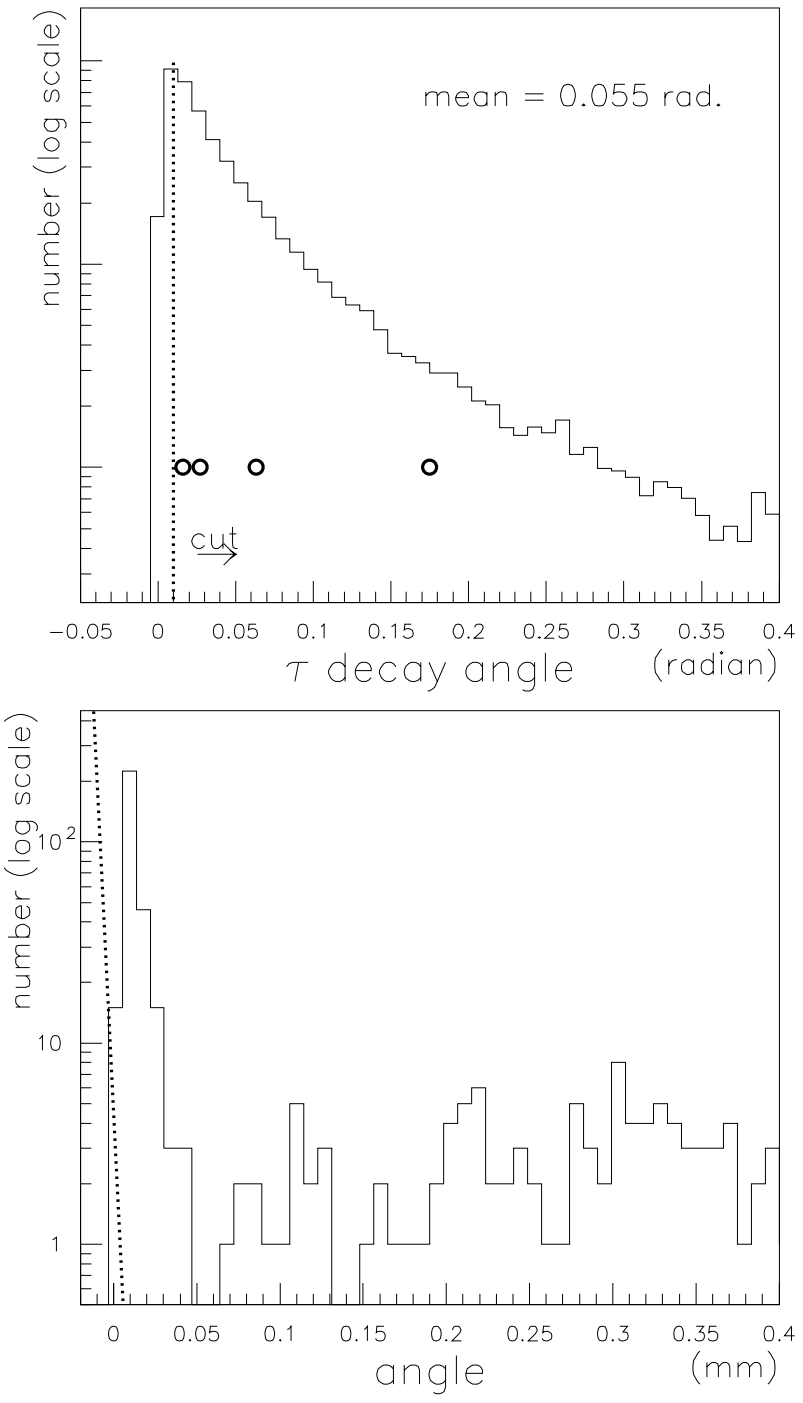

Figure 5-3 Top: Decay angle distribution for the single charge decays of taus from simulated ν_τ interactions. Also shown are the values for the four events which pass all selection criteria. Bottom: Distribution of kink angles for all kinks found in the data set with lengths less than 5 mm.

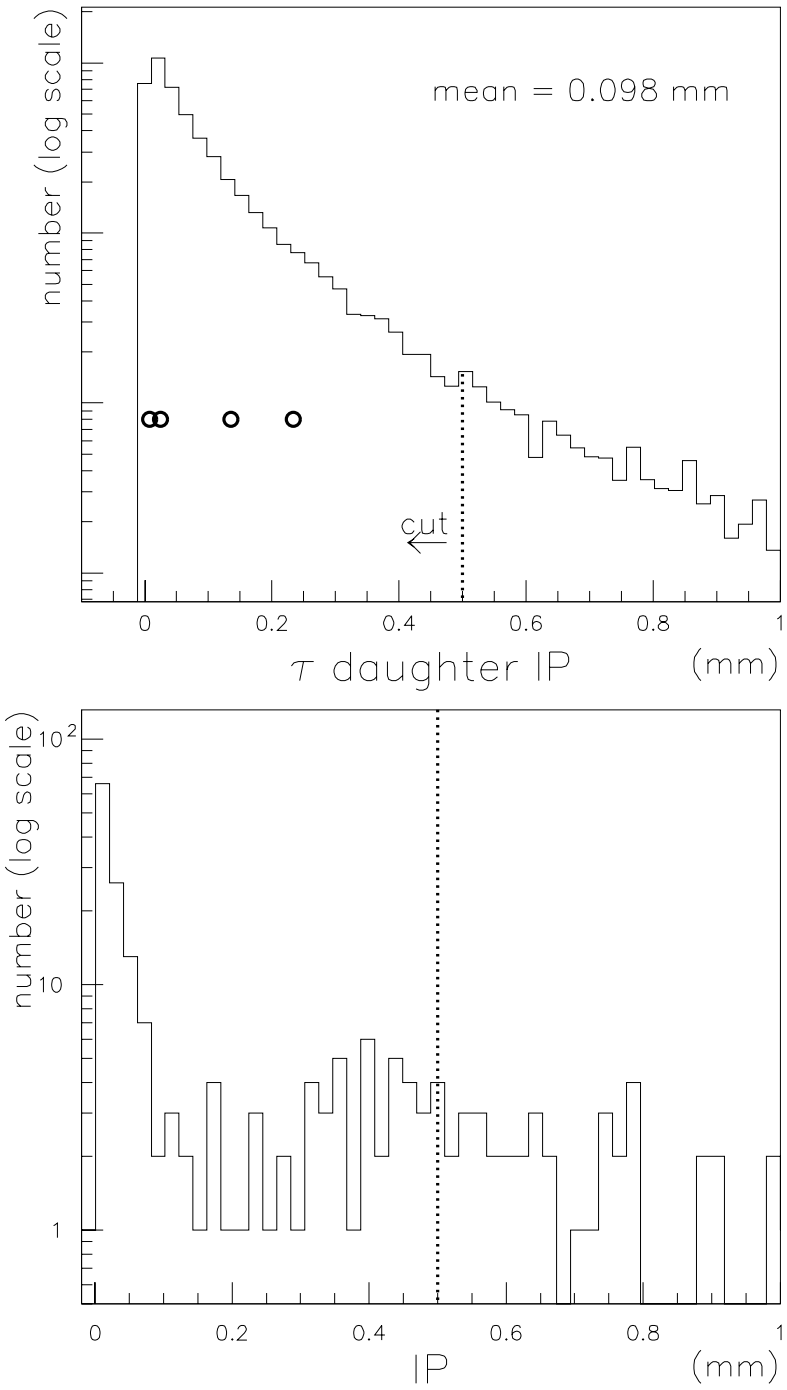

Figure 5-4 Top: Impact parameter distribution for the single charge decays of taus from simulated ν_τ interactions. Also shown are the values for the four events which pass all selection criteria. Bottom: Distribution of impact parameter for all kinks found in the data set with lengths less than 5 mm and kink angles greater than 10mr.

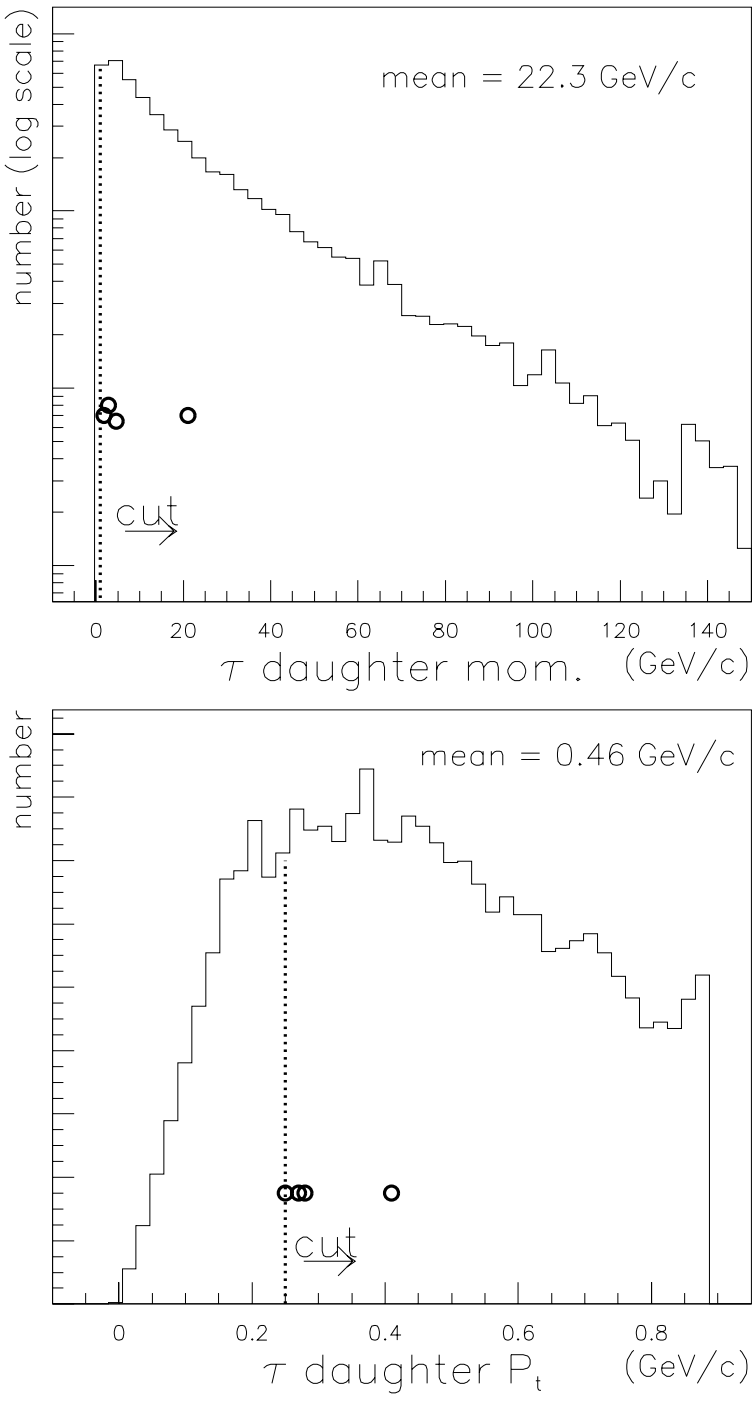

Figure 5-5 Top: Daughter momentum distribution for the single charge decays of taus from simulated ν_τ interactions. Bottom: transverse momentum distribution for the single charge decays of taus from simulated ν_τ interactions. Also shown are the values for the four events which pass all selection criteria.

Tau daughter transverse momentum selection

Since the kink is the result of a massive decay, a requirement is also placed on the transverse momentum of the daughter, P_t , which is defined as follows:

$$P_t = P_{Daughter} \cdot Sin\theta_{kink}$$

Θ is the angle of the daughter trajectory with respect to the tau direction.

The decay track's P_t is required to be greater than 250 MeV/c and this criteria accepts 78% of simulated tau decays. This selection also reduces potential backgrounds caused by scattering interactions of primary particles which are discussed in section 6.4.4. The cut value is the same that is used in a separate experiment (also discussed in 6.4.4) which measured the rate of these scatters. Figure 5-5 shows a distribution of P_t for Monte Carlo simulated single charged tau decays. Figure 5-6 compares the distribution of transverse momentum for the expected background and the distribution for the data events. The data events shown are those that have passed the maximum length, minimum angle, impact parameter and momentum criteria.

It can be seen in Figure 5-6 that there are five events that pass the maximum length, minimum angle, impact parameter and momentum criteria. Only four of these kinks have no primary electron or muon in the event and constitute the tau signal. The fifth high P_t kink has a primary electron, and the kink is most likely caused by the single charged decay of either a D^+ or D^- produced in a ν_e charged-current interaction.

The efficiency of all these criteria at selecting tau decays is found by applying them to a large set of simulated tau decays. The fraction fulfilling the criteria is found separately for the electron, muon and hadron decay modes. The average of these fractions, weighted by the individual branching ratios, is the fraction of all single charged tau decays which pass the selection criteria. The fractions of events that pass all selection criteria , as well as the overall efficiency of the tau decay selection process is shown in are listed in table Table 6-1.

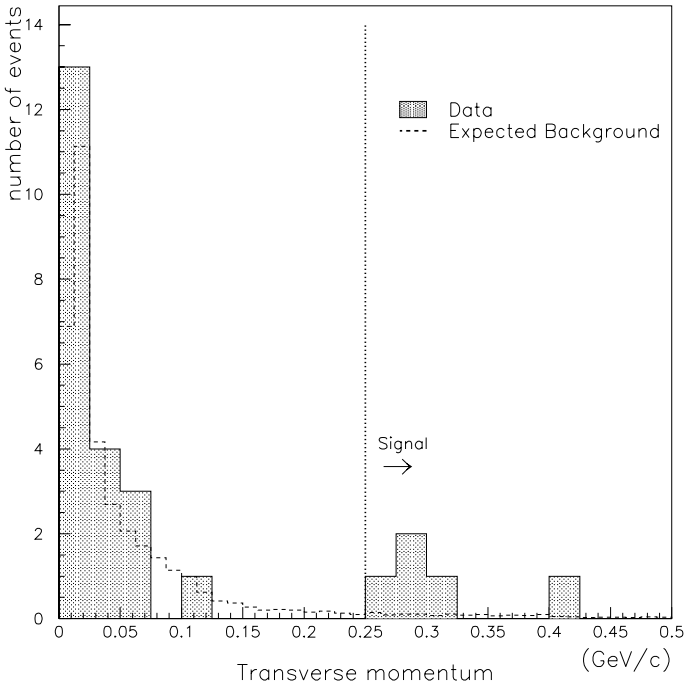

Figure 5-6 P_t distribution for data events passing minimum angle and momentum criteria. Also shown is the distribution for the expected background.

Decay mode	Branching ratio (%)	Fraction selected	Total Efficiency
$\tau \rightarrow e$	17.84 ± .06	.555	
$\tau \rightarrow \mu$	17.37 ± .06	.556	
$\tau \rightarrow$hadron	50.14 ± .07	.501	
All 1-Charge	85.35 ± .07	.513	.38

Table 5-1 Fraction of simulated tau decays which passed the tau selection criteria and the resulting efficiency (fraction selected × branching ratio)

5.2 Tau events

When the selection criteria are applied to the data set of 203 neutrino events, four are selected.

The values of the decay length, kink angle, daughter momentum, transverse momentum and impact parameter or the our events are shown in Table 5-2 . These four

events are the tau-neutrino interaction signal. Since the set of tau events is small, each event is discussed individually. The emulsion segments near the interaction vertex and decay kink for each selected event are shown in Figure 5-7 through Figure 5-11

Event	3024-30175	3333-17665	3263-25102	3039-01910
Parent length (μm)	4590 ± 10	550 ± 20	1950 ± 10	290 ± 10
Decay angle (mrad)	93 ± 0.6	90 ± 2.0	130 ± 0.5	13 ± 0.9
Transverse mom. (GeV/c)	$0.27^{+.14}_{-.07}$	$0.41^{+.14}_{-.08}$	$0.25^{+.20}_{-.09}$	$0.28^{+.10}_{-.08}$
Daughter mom. (GeV/c)	$2.9^{+1.5}_{-0.8}$	$4.6^{+.1.4}_{-0.4}$	$1.9^{+2.2}_{-0.7}$	$21^{+.14}_{-0.6}$
Impact Parameter (μm)	136 ± 3	25 ± 1	234 ± 1	7 ± 1

Table 5-2 Values of selection criteria for events passing tau selection.

5.2.1 Selected event 3024-30174

Event 3024-30175 is found in emulsion module ECC1 and has three charged primary tracks as shown in Figure 5-7. Tracks 1, 2 and 4 all originate from a single vertex position where the neutrino interacted. Track 2 is made up of 6 collinear segments and is identified as the tau lepton produced in the charged-current interaction. Track 3 begins in the next emulsion layer downstream of the last segment of Track 2 of and is the charged daughter of the tau decay. When projected towards each other, the distance of closest approach between Tracks 2 and 3 is 0.8 μm while the uncertainty from projection errors

the two tracks is 0.7 microns. This is completely with an intersection. This intersection can then be understood as the place where the tau decays, which is in the plastic base separating two emulsion layers..

All three final tracks are observed in the spectrometer, confirming that they all are the result of a single event in the emulsion. The daughter track is associated with a shower in the scintillating-fiber tracker as is identified as an electron.

5.2.2 Selected event 3039-01910

Figure 5-8 shows event 3039-01910 that is found in emulsion module ECC1. The interaction results in six primary tracks, none of which are identified as a muon or an electron.

Track 7 is identified as the tau lepton. It is recorded as a single segment in the up-stream side of emulsion plate 10, the first plate downstream of the interaction vertex. The first recorded segment of track 2 is in the next downstream emulsion layer and is the charged daughter of the tau decay. The distance of closest approach between the projections of track 7 and track 2 is 2.5 ± 2.1 microns. The relatively large uncertainty of the impact parameter is due to the projection error of track 7. Track 7 is made of only one emulsion segment which is 70 μm downstream of the fitted interaction vertex position. The projection is a straight line fit of the segment and the vertex, and since the distance between them is small, the uncertainty in the projection is magnified. The impact parameter is consistent with an intersection. All the final tracks are observed in the scintillating-fiber tracker.

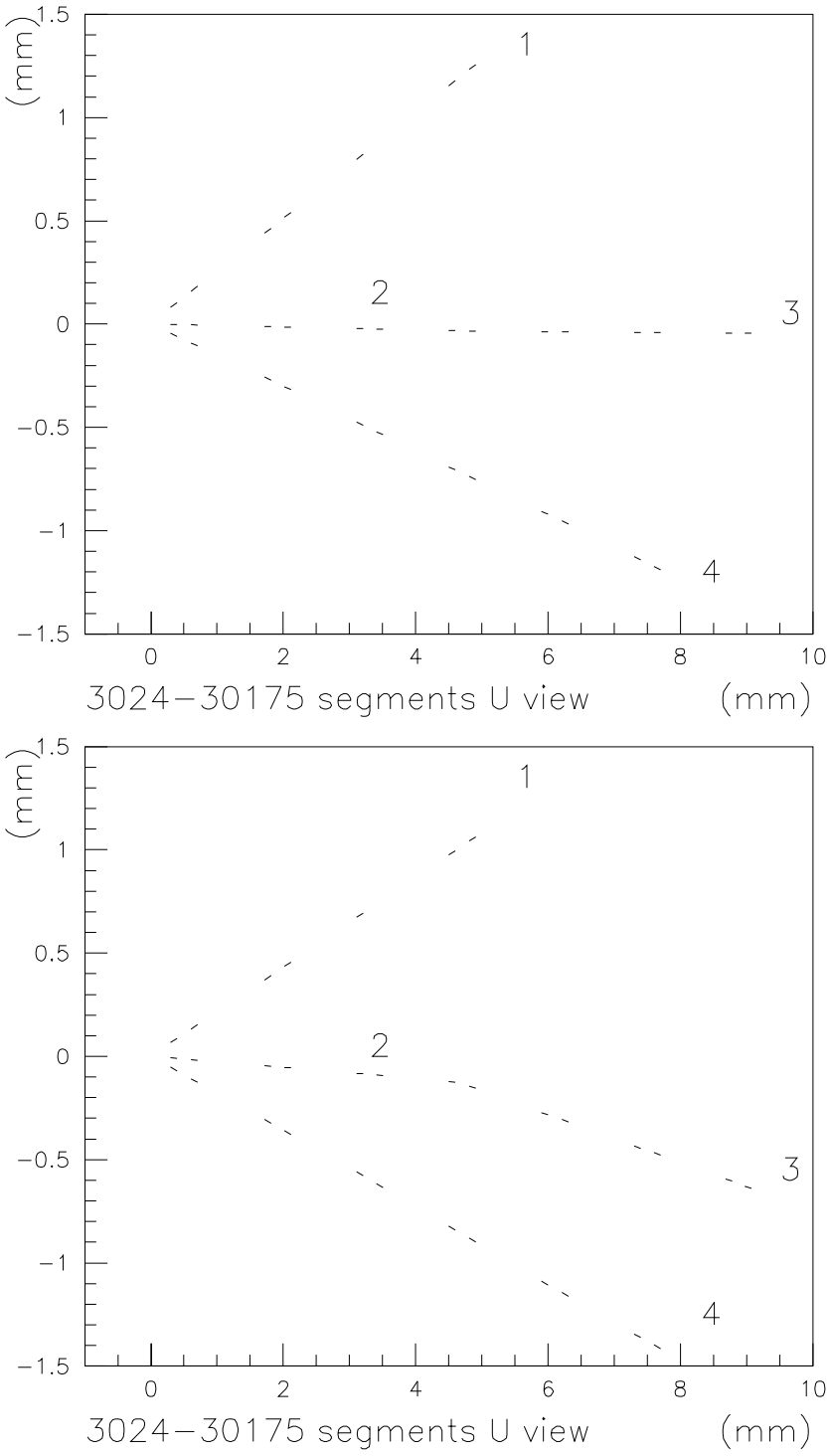

Figure 5-7 Emulsion segments of event 3024_30125

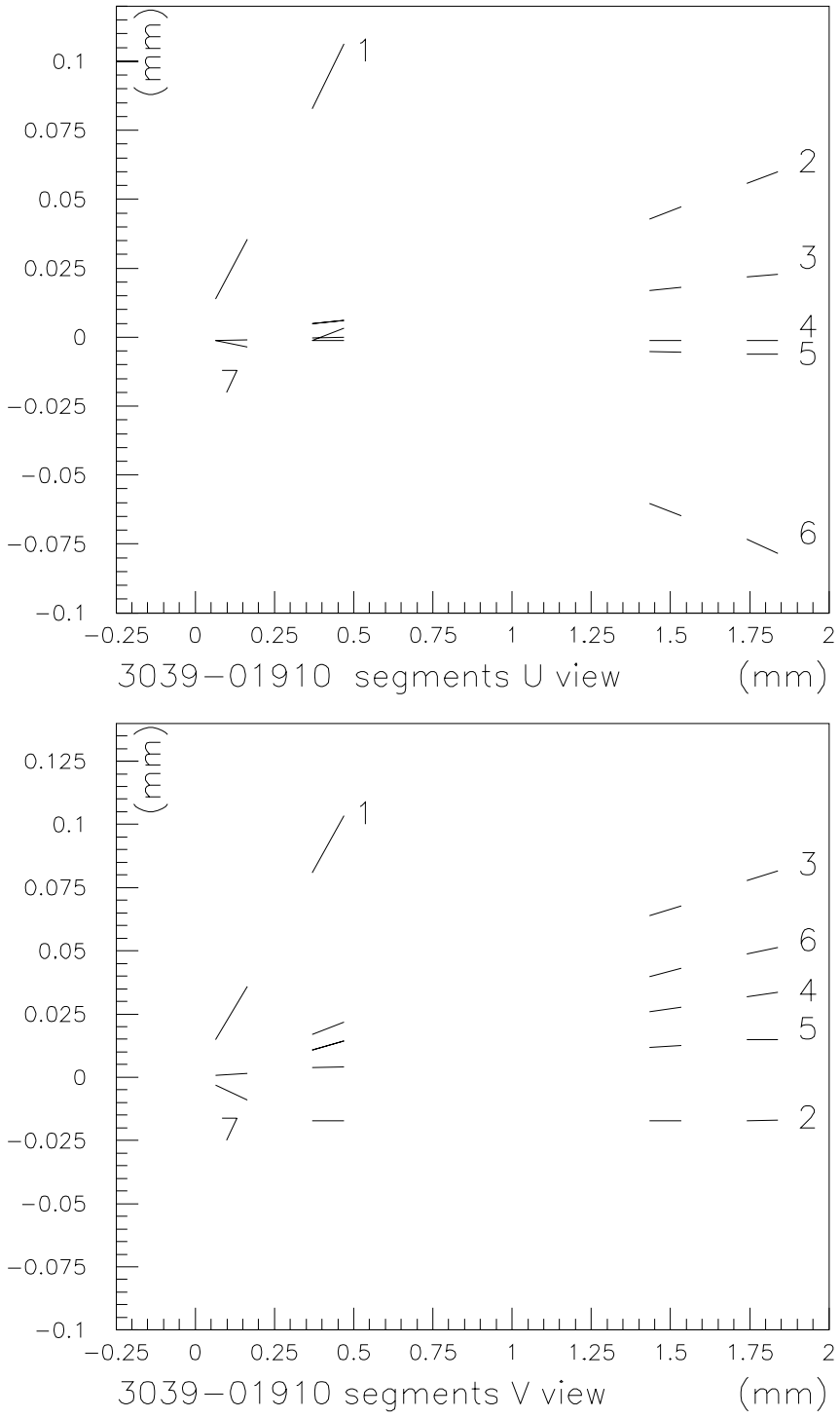

Figure 5-8 Emulsion segments of event 3039-01910

5.2.3 Selected event 3263-25105

Event 3263-25105 is observed in module E/B1 and has three primary tracks. The emulsion segments of the interaction and decay kink are shown in Figure 5-9. Tracks 1, 2 and 3 all originate from a single vertex position. Track 1 is the tau lepton and is composed of two segments. The daughter of the tau, track 4, starts in the next downstream emulsion layer. This track goes to the end of the scan volume. Tracks 1 and 4 have a distance of closest approach of 1.0 ± 0.8 μm.

The daughter track is identified as an electron by pair production that occurs further downstream in the emulsion module and by the resulting shower which develops in the scintillating-fiber tracker.

5.2.4 Selected event 3333-17665

Figure 5-10 and Figure 5-11 show event 3333-17665. This is an interaction with six charged primary tracks, none of which are identified as a muon or an electron found in emulsion module E/B2.

Track 1 consists of a single segment and is the tau. The first recorded segment of the daughter, track 3, is in the next downstream emulsion layer. These two tracks have a distance of closest approach of 1.3 ± 1.2 microns. The decay of the tau occurs within the plastic base of an emulsion sheet and all five final tracks are observed in the scintillating-fiber tracker.

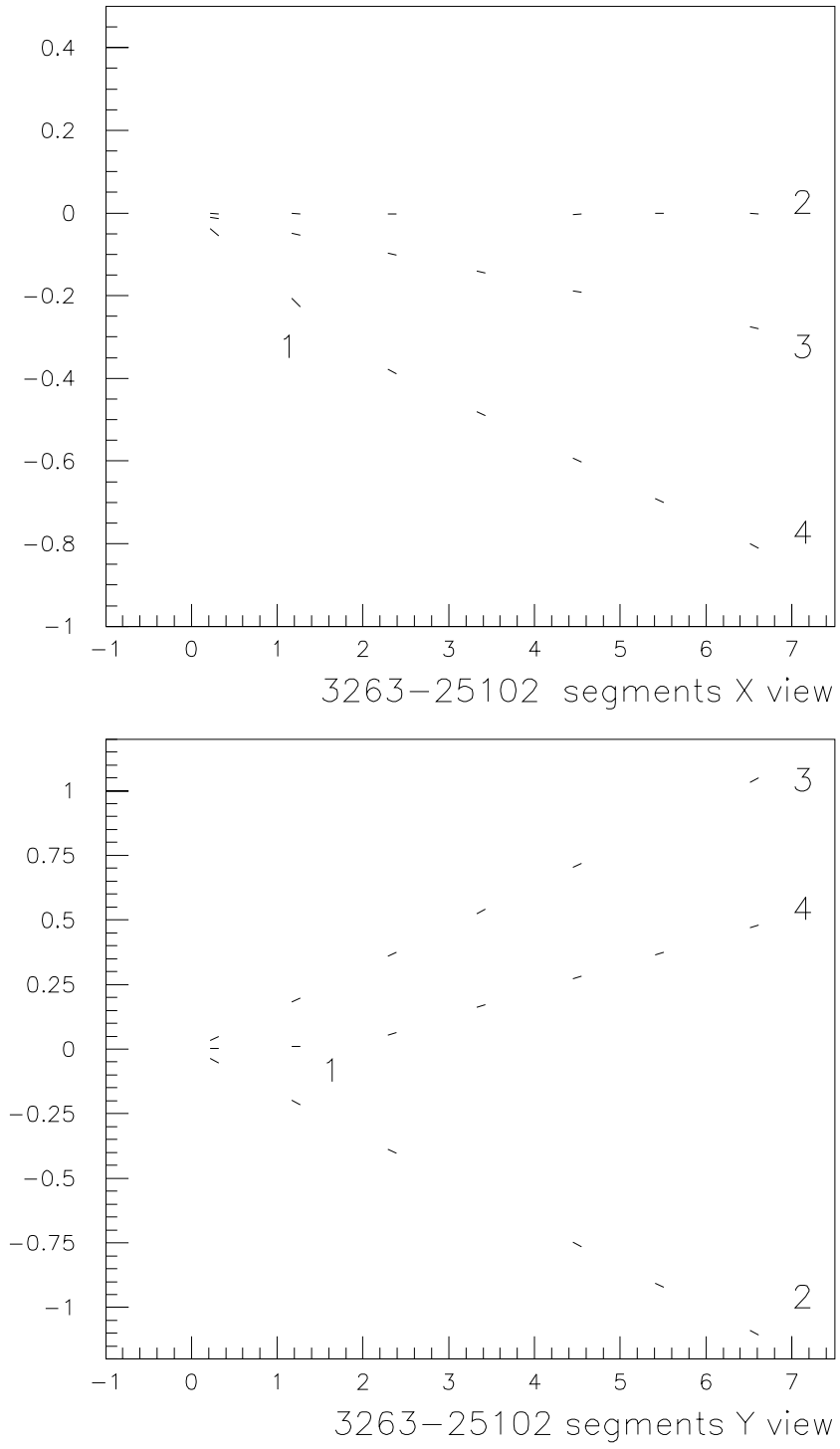

Figure 5-9 Emulsion segments of event 3263-2504

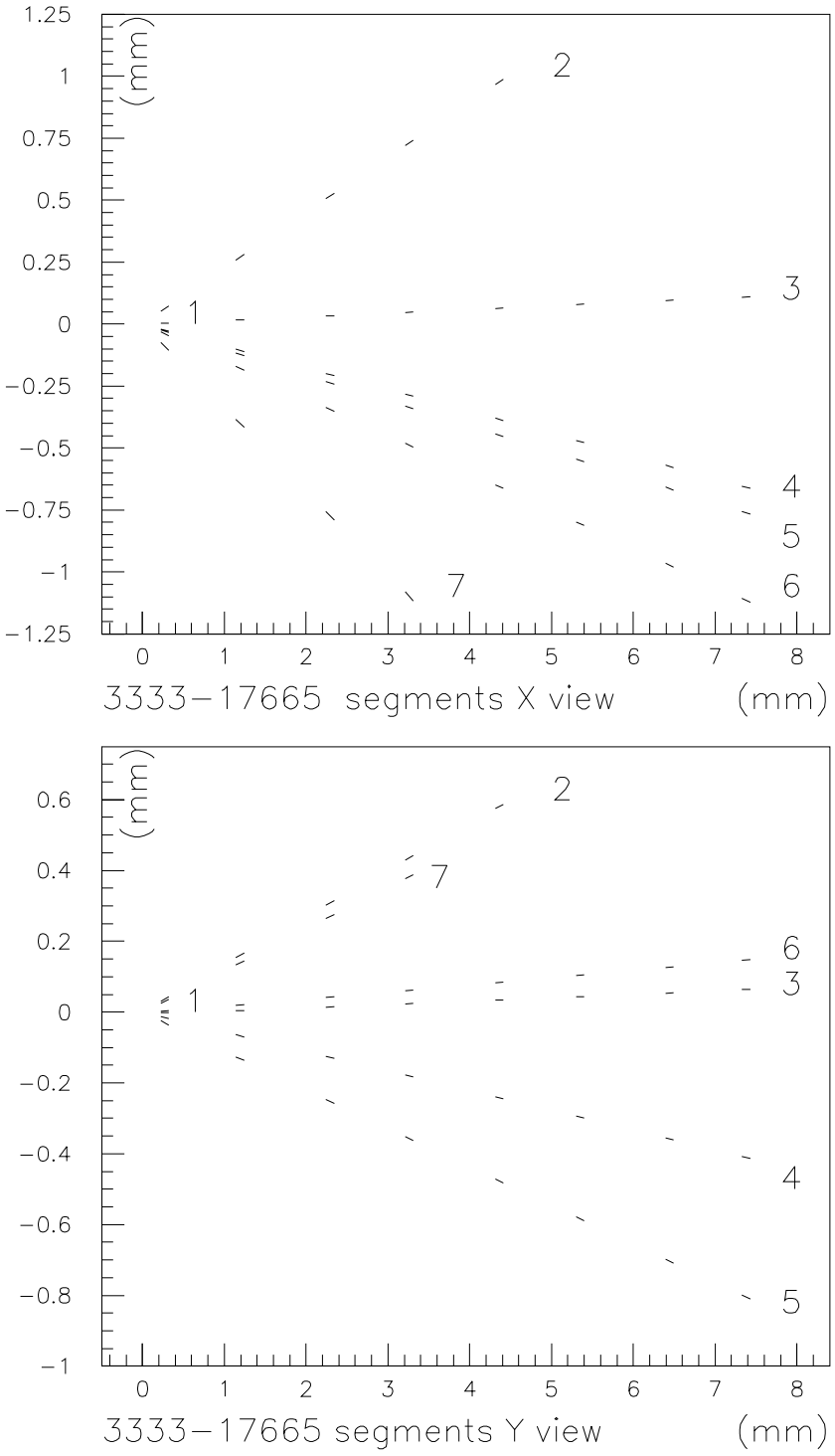

Figure 5-10 emulsion segments of event 3333-1766

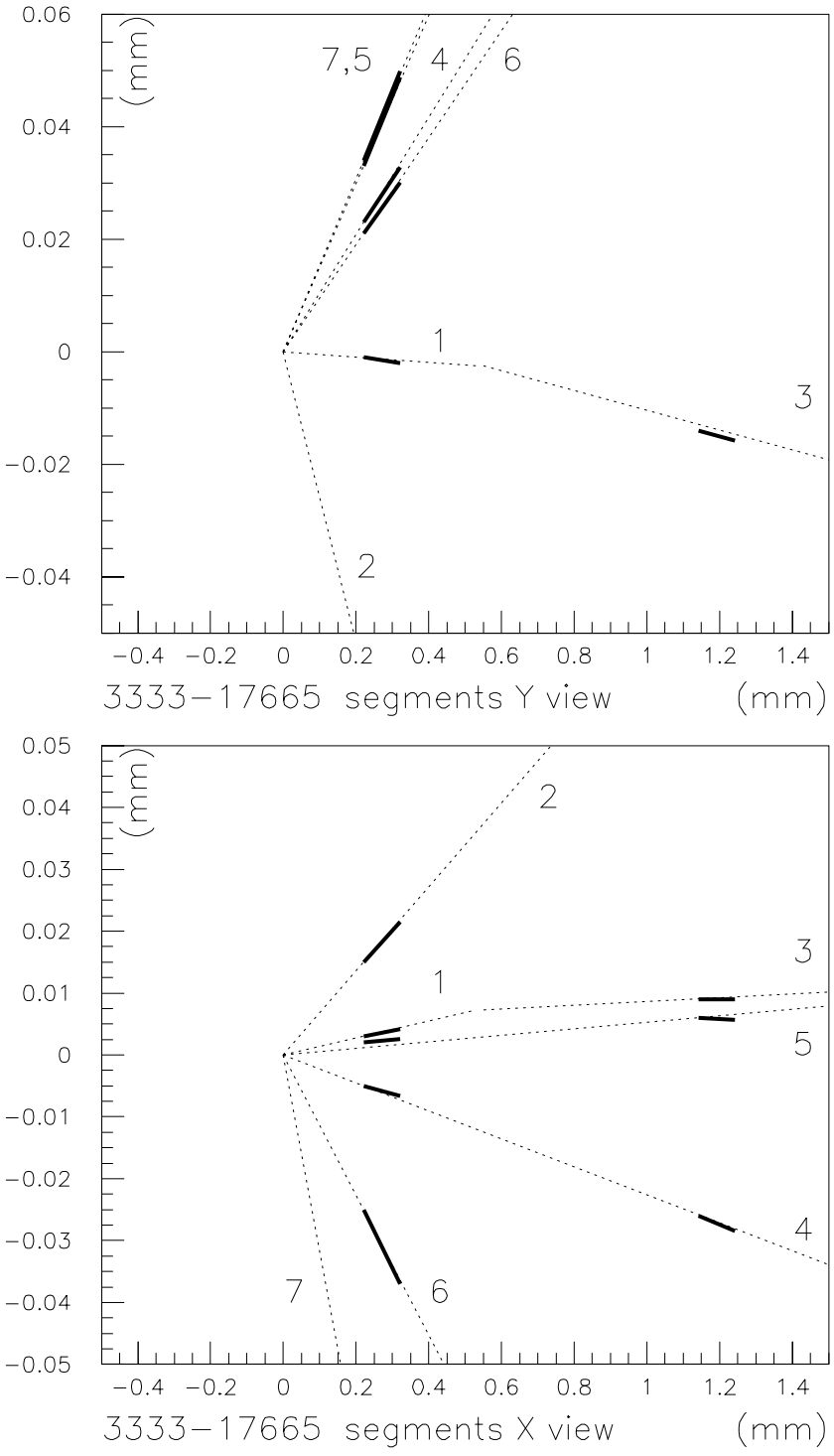

Figure 5-11 Emulsion segments in first two emulsion sheets of event 3333-17665

6 Expected number of tau and background events

While the four observed tau events all satisfy the selection criteria for the tau signal, it is necessary to estimate the number of tau events expected to determine that these four are consistent with standard model ν_τ interactions. Furthermore, the possibility that one or more of them might be a background process needs to be investigated.

The expected number of ν_τ charged-current interactions can be found in two different ways: either by direct calculation of interaction rate and the efficiency of identifying tau events, or from the measured ν_μ and ν_e charged-current event rates combined with the calculated ratios of the interaction rates of ν_τ to ν_e (or to ν_μ). The second method has advantages oer the first since the ν_μ and ν_e interactions can be unambiguously identified in the data. Furthermore, using these ratios also results in less uncertainty than a direct calculation of expected ν_τ events, since the systematic errors that are common in the production rate, interaction rate, and detection efficiency of ν_e ,ν_μ and ν_τ all cancel.

The number of background events is determined by calculating the fraction of ν_e and ν_μ events that pass all of the tau selection criteria. Since ν_e and ν_μ events contribute to the background at different levels, it is also necessary to determine their relative composition of the data set.

6.1 Composition of the interaction data set

The *a priori* calculation of the number of expected ν_τ events then proceeds as follows: the fraction of neutrino interactions in the data set due to ν_τ is calculated and this is scaled by the total number of events. This method is applied to ν_e and ν_μ interactions as well. The different components , F_α, of the entire data set are defined as:

$$F_\alpha = \frac{Rate_\alpha \cdot \varepsilon_\alpha^{Total}}{\sum_\alpha Rate_\alpha \cdot \varepsilon_\alpha^{Total}} \qquad \textbf{Eq. 6-1}$$

$$\varepsilon_\alpha^{Total} = \varepsilon_\alpha^{Trig} \cdot \varepsilon_\alpha^{Selection} \cdot \varepsilon_\alpha^{Location} \qquad \textbf{Eq. 6-2}$$

The subscript α corresponds to one of five types of neutrino interactions: ν_e charged-current, ν_μ charged-current (prompt sources), ν_μ charged-current (non-prompt sources), neutral-current interactions, and ν_τ charged-current. *Rate* corresponds to the expected rate of the neutrino interactions in the target and ε corresponds to the efficiency.

The efficiencies of Equation 6.2 represent the individual contributions to the total detection efficiencies; ε^{Trig} is the trigger efficiency, $\varepsilon^{Selection}$ is the efficiency to select the interaction using the spectrometer data and $\varepsilon^{Location}$ is the efficiency of locating that type of event within the emulsion using the spectrometer predictions.

The neutrino interaction rates are equal to the product of their flux at the target, the number of nuclei within the emulsion target and their interaction cross-section. The full details of the calculation of all the neutrino interaction rates are given in Appendix A. Since the number of neutrino interactions depends on the number of neutrinos produced and the available target mass, the interaction rate is calculated per protons incident on the

dump, per kilogram of target. The flux of the high energy neutrinos depends on the rate of charm-meson production in the beam dump and the branching ratio through leptonic and semi-leptonic modes. The flux of the low energy ν_μ 's depends on the rate of production and decay of π and K within the dump. Monte Carlo simulations of these processes are used to determine the number of neutrinos of each type passing through the emulsion target per incident proton.

All inputs to Equation 6-1 are discussed in the following sections.

Trigger efficiency: ε^{Trig}

The trigger efficiency is the fraction of the neutrino interactions occurring in the emulsion target that are recorded by the spectrometer. This depends on the efficiency of the trigger counters at detecting the charged tracks and the efficiency of the trigger criteria to recognize events that are neutrino interactions.

The efficiency of the scintillating trigger counters has been discussed in Section 4.1.1 and is greater than 97%

The overall efficiency of the entire trigger system at identifying possible neutrino interactions is estimated with a Monte Carlo simulation. The efficiency varies with the number, angular distribution and energy of the particles produced in the interaction. These, in turn, depend on the energy and the type of neutrino interaction. Since lower energy neutrinos produce fewer charged particles the interactions of non-prompt ν_μ's have a lower trigger efficiency than do prompt. Likewise, neutral-current interactions produce fewer charged particles and thus the trigger efficiency for neutral-current interactions is also lower .

All five types of neutrino interactions were simulated with the LEPTO event generator[32] and a GEANT[33] detector response Monte Carlo. In this simulation, charged tracks passing through the scintillating trigger counters were recorded, as was their energy deposition in the EM calorimeter. The trigger criteria (described in section 4.1) were then applied to the events. The fraction of the simulated events fulfilling the trigger requirements is an estimate of the trigger efficiency. Table 6-1 lists these efficiencies for all types of neutrino interactions. For ν_τ events the efficiency estimated to be 97.2%.

Neutrino event selection efficiency: $\varepsilon^{Selection}$

Besides influencing the trigger efficiency, the number of primary tracks in an event also affects the efficiency of selecting neutrino interactions from those recorded in the spectrometer. As with the trigger, there is a higher efficiency for events with a greater number of primary tracks.

The process of selecting events with the event display was simulated to estimate the total selection efficiency. Events were generated, passed though the data reduction code and then selected on the visual event display by physicists just as the real data. The selection efficiency was estimated as the fraction of all simulated events which were selected in this manner. The dependence of the resulting efficiency on the number of charged tracks from the neutrino interaction for all different emulsion stations is shown in Figure 6-1.

In the figure it can be seen that the efficiency for the more downstream stations is slightly lower than that of the upstream stations. This is because the number of scintillating fiber planes that the tracks pass through is larger for the upstream modules since there are more fiber planes downstream to detect the track. This makes it easier for the offline code and the human scanner to recognize tracks from a neutrino interaction vertex.

Emulsion location efficiency: $\varepsilon^{Location}$

The total location efficiency can be found by dividing the number of events located in the emulsion , 203, by the total number selected through the spectrometer data, 898. This gives an efficiency of ~23%. However, at the time of this analysis, emulsion data had been produced for only 511 of the events that were selected through the software and visual event display. This is because many of the events selected with the spectrometer data were in regions of the emulsion where the local background track density was too high. For these events automated scanning would not result in useful data and they were not scanned. This source of inefficiency depends only on the local

muon flux which is a factor external to the interaction and, thus, effects all five types of interactions equally.

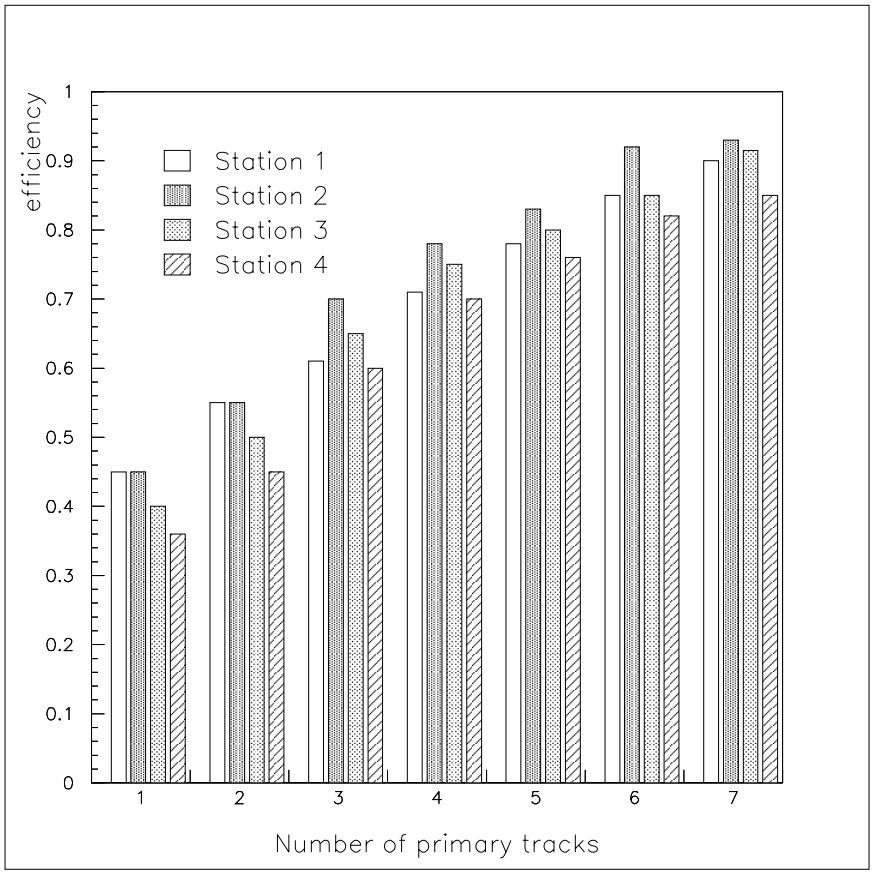

Figure 6-1 Strip and scan efficiency as a function of multiplicity and emulsion module station.

For the events that were scanned, the number of primary vertex tracks contributes to the likelihood of the event being located in the emulsion, with location efficiency increasing with the number of tracks. The dependence of $\varepsilon^{location}$ on this multiplicity is found by comparing the multiplicity distribution for the located events with that of a set of simulated events that had met the trigger, and visual selection criteria. The relative composition of this simulated set was set to be proportional to the product of the predicted rate of interaction, the trigger efficiency and the selection efficiency for the various types of neutrino interactions. Thus, the only difference between the distributions for the located events and the simulated events is due to the emulsion location efficiency. The variation of location efficiency with the number of primary tracks is found by comparing simulated and located events that have the same multiplicity. A histogram of

the location efficiencies for located events and for the simulated events are shown in Figure 6-2 .

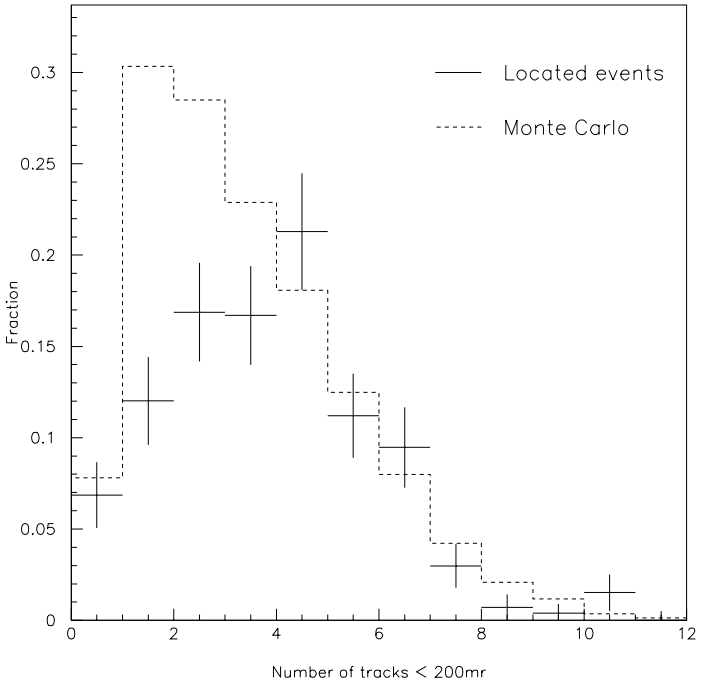

Figure 6-2 Multiplicity of primary tracks for events located in the data set and in Monte Carlo simulations. The Monte Carlo has been normalizes to the N> 3 data set.

Once the dependence of the location efficiency on the number of primary tracks is known, it can be calculated for each individual type of neutrino interaction. The location efficiency for each type of interaction is estimated by using the expected multiplicity for that event type and the efficiencies for different multiplicities i.e. :

$$\varepsilon_{\alpha}^{Location} = \sum_{i} k_{\alpha}^{i} \cdot \varepsilon^{i}$$

The sub-script α corresponds to five different types of neutrino interaction, k_{α}^{i} is the fraction of the type α with multiplicity *i* and ε^{i} is the efficiency for locating events

with that multiplicity. The $k_\alpha{}^t$ are taken from the individual multiplicity distributions that make up the entire simulated set shown in Figure 6-2.

Table 6-1 summarizes the trigger, selection and location efficiencies found for all types of neutrino interactions. The total efficiency of the entire selection process is the product of these three numbers. For ν_τ charged-current interactions the total efficiency is found to be 57%. It is again noted that the emulsion location efficiencies stated are relative, and thus the total efficiency shown in Table 6-1 are relative.

	Efficiency (%)			
	trigger	selection	location	total
ν_μ prompt charged-current	94	80	78	59
ν_μ non-prompt charged-current	67	76	67	34
ν_e charged-current	98	80	73	57
ν_{all} neutral-current	84	81	75	51
ν_τ charged-current	97	80	73	57

Table 6-1 Trigger, selection and location efficiencies for neutrino interactions

6.1.1 Estimation of the number of each type of neutrino interaction

The number of each type of neutrino interactions, N_α, making up the located data set can now be calculated using Equation 6.1:

$$N_\alpha = N_{Data} \cdot F_\alpha = 203 \cdot \frac{Rate_\alpha \cdot \varepsilon_\alpha^{total}}{\sum_\alpha Rate_\alpha \cdot \varepsilon_\alpha^{total}} \qquad \textbf{Eq. 6-3}$$

This ratio must be used since the total efficiency does not include the fraction of neutrino events that were identified with spectrometer data but whose emulsion was not scanned.

The total detection efficiencies are those in Table 6-1 and the neutrino interaction rates are taken from Table A- and Figure A-8-4 in Appendix A. Table 6-2

summarizes the results. The total number of expected ν_τ interactions calculated in this manner is 6.9 ± 2.3.

6.2 Expected number of ν_τ from measured number of ν_e and ν_μ

As an alternative to the *a priori* method, the expected number of ν_τ events can be calculated using the actual number of ν_μ and ν_e observed.

	Rate (kg^{-1} $proton^{-1}$)	ε^{Total}	F_α	Expected #
ν_μ prompt CC	$2.3 \pm 0.5 \times 10^{-18}$	.59	0.22 ± 0.005	45 ± 10
ν_e CC	$2.7 \pm 0.6 \times 10^{-18}$	.57	0.25 ± 0.006	51 ± 11
ν_μ non-prompt CC	$4.4 \pm 0.7 \times 10^{-18}$	.34	0.26 ± 0.004	50 ± 9
ν NC	$3.0 \pm 0.8 \times 10^{-18}$	.51	0.23 ± 0.006	51 ± 13
ν_τ CC	$0.37 \pm 0.13 \times 10^{-18}$	.57	0.035 ± 0.012	6.9 ± 2.3

Table 6-2 Expected number of neutrino interaction in the located data set.

6.2.1 The number of ν_μ charged-current events

In the set of located interactions, there are 71 that have primary muons and are thus identified as ν_μ charged-current interactions. The primary muons are identified by four or more co-linear hits in the six planes of the muon identification system that are linked through the drift chambers to an emulsion track from the neutrino interaction vertex. To find the actual number of ν_μ charged-current interactions in the data set, the number found this way has to be corrected for muon identification efficiency. The efficiency is determined by the detector acceptance and varies with the ν_μ energy. The acceptance of the muon detectors is found with simulated ν_μ charged-current events and is 73 % for muons from 'prompt' sources and 56% for 'non-prompt' sources. The overall ν_μ efficiency depends on the prompt to non-prompt ratio. Using $F_{prompt} / F_{non\text{-}prompt}$ from Table 6-2 gives an average efficiency of 63%. Thus, the corrected number of ν_μ charged-current interactions in the 203 located neutrino interactions is 113 ± 13. This

is slightly higher than but consistent with the calculated expectation of 95 ± 13 from the *a priori* calculations.

6.2.2 Number of prompt ν_μ and ν_e charged-current interactions

In order to proceed with the calculation of the number of ν_τ interactions, the number of neutrinos from prompt sources needs to be determined. Theses are the ν_μ and ν_e produced from the decay of charmed mesons. A measurement of the ratio of the number of 'non-prompt' to the number of 'prompt' ν_μ charged-current interaction is made using the observed primary muon momentum spectrum. The total number of ν_e, all of which are assumed to be from 'prompt' sources, is found from the energy spectrum in the EM calorimeter. The number of prompt neutrinos in the located data set was the subject of a Kansas State thesis[28] , the results of which will be used here.

This ratio the number of prompt ν_μ events to the total number of ν_μ was found therein by fitting the sum of the muon momentum spectra from simulations of both sources to the total muon momentum spectrum measured with the analysis magnet. This ratio was then used as an input to a fit of the calorimeter data which calculated total fraction of the located data set due to prompt neutrinos.

Since the calorimeter's signal for ν_μ charged-current events and neutral-current events is similar, the calorimeter is best at distinguishing ν_e charged-current events. On average, the primary electron from these events deposit a greater energy than do either of the other event types. For this reason, several constraints were imposed on the fit to the calorimeter data. The first was that number of neutral-current events is 0.21 ± 0.03 of the total number of events. This is the ratio expected taking into account the relative cross-sections for neutral current and charged-current interactions and the estimated selection and location efficiencies. Second, the ratio of ν_e to prompt ν_μ $= 0.96 \pm 0.01$, which is the ratio of their estimated total selection efficiencies. Finally, the ratio of ν_τ to ν_μ charged-current events = $0.089 \pm .0.016$.

The result of this fit gives a total of 58 ± 7 prompt ν_μ charged-current interactions. The fit has a χ^2/dof = 11.2/8 [28]. This result agrees with the *a priori* calculation of 45 ± 10. The actual number of ν_e charged current interactions in the set

of located events was found to be 59 ± 6 events which is also consistent with the value of 51 ± 11 obtained the previous calculation. Since the result of 58 ± 7 prompt ν_μ events and 59 ± 6 ν_e events relies on actual measurements taken from the experiment, they are expected to be more accurate than the *a priori* calculation and they will be used for all subsequent calculations in this thesis.

The number of ν_e events in the located data set was confirmed with the results of an artificial neural network[34]. The input variables for the network were; the number of scintillating-fiber hits, the number of tracks reconstructed in the scintillating fiber, the number of DC hits, the number of DC tracks, the total EM calorimeter energy, the number of clusters in the EM calorimeter, the average cluster energy and the number of hits in each of the MID walls. The network selected 62 of the located events as ν_e charged-current interactions.

6.2.3 Ratios of N_τ to N_μ and N_τ to N_e

The expected number of ν_τ charged-current interactions can be calculated from the actual number of prompt charged-current interactions in the data set. The ratio of the number of tau events, N_τ, to the number of prompt events, N_l ,,can be written as:

$$\frac{N_\tau}{N_l} = \frac{Rate_\tau \cdot \varepsilon_\tau^{Total}}{Rate_l \cdot \varepsilon_l^{Total}} \qquad \textbf{Eq.6-4}$$

Here the subscript l stands for either ν_e or prompt ν_μ . The interaction rates for ν_τ, ν_e and prompt ν_μ are derived in the appendix and are given by equations A-2 and A-4. The ratio of these rates is given by:

$$\frac{Rate_\tau}{Rate_l} = \frac{\dfrac{\sigma(pW \to D_s)}{\sigma(pW)_{total}} \cdot Br(D_s \to \nu_\tau) \cdot 2 \cdot \int \eta(E) \cdot k(E) \cdot dN/dE \, dE}{\displaystyle\sum_i \frac{\sigma(pW \to C_i)}{\sigma(pW)_{total}} \cdot Br(C_i \to \nu_l) \cdot \int \eta_l(E) \cdot dN_l/dE \, dE}$$

$$= \frac{\left\langle \frac{\sigma(D_s)}{\sigma(D^0)} \right\rangle \cdot Br(D_s \rightarrow \nu_\tau) \cdot 2 \cdot \int \eta(E) \cdot k(E) \cdot dN/dE \, dE}{\sum_i \left\langle \frac{\sigma(C_i)}{\sigma(D^0)} \right\rangle \cdot Br(C_i \rightarrow \nu_l) \cdot \int \eta_l(E) \, dN_l/dE \, dE} \qquad \textbf{Eq. 6-5}$$

The sum in the denominator is over the three charm mesons, $C_i = D^0, D^{+/-}$ or D_s, η(E) is the fraction of neutrinos with energy E produced in the charm meson decay that pass through the target, k(E) is the kinematic threshold for heavy lepton production, and the integral is over the energy spectrum of the produced neutrinos. In the last expression the D^0 production cross-section has been factored out and only the ratios of cross-sections $\sigma(D_s)/\sigma(D^0)$, $\sigma(D_s)/\sigma(D^+)$ and the branching fractions of the charmed mesons remain. The contribution due to the phase space distribution of the charm decays to the total uncertainty of this ratio is minimized since acceptance functions, η, appear in both numerator and denominator.

The ratios $\sigma(C^i)/\sigma(D^0)$ are taken from Table A-1 and the branching ratios are taken from Table 3-1. The integrals depend on the parameterization of the phase–space distributions for charm meson production which are discussed in the appendix. They are evaluated with Monte Carlo simulations of charm meson production and a subsequent decay through neutrino modes. The parameters for the phase space distribution are varied through their uncertainty and the integral is calculated by simulating the production of one hundred thousand neutrinos and projecting them to the emulsion target.

A distribution of the value of the ratio for 3000 simulations, each of one hundred thousand neutrinos, is shown in Figure 6-3. From this distribution, the most probable value of the ratio and it's spread are found.

6.2.4 Expected number of ν_τ interactions

The expected number of ν_τ charged-current interactions, N_τ, can now calculated using the observed number of ν_e and ν_μ charged-current interactions:

$$N_\tau = N_e \cdot \left[\frac{R_\tau}{R_e} \right] \cdot \frac{\varepsilon_{\nu_\tau}^{total}}{\varepsilon_{\nu_l}^{total}} \qquad \textbf{Eq. 6-6}$$

The interaction rate ratio ν_τ / ν_e is $0.139^{+.030}_{-.027}$ as shown in Figure 6-3 . The number of ν_e interactions is taken from section 6.2 and is $N_e = 59 \pm 6$. The total location efficiency for ν_e and ν_τ events are taken from Table 6-1 and are both 0.57. The predicted number of ν_τ charged-current interactions is then $N_\tau = 8.2 \pm 1.8$

Similarly, the interaction rate ratio ν_τ to ν_μ is taken from the distribution in Figure 6-3 is $0.163^{+.030}_{-.027}$. The number of prompt ν_μ charged-current interactions is measured to be $N_\mu = 58 \pm 7$ as shown in Table 6-2 The ratio of location efficiencies is .57/.59 giving the number of ν_τ interactions $N_\tau = 9.1 \pm 1.9$.

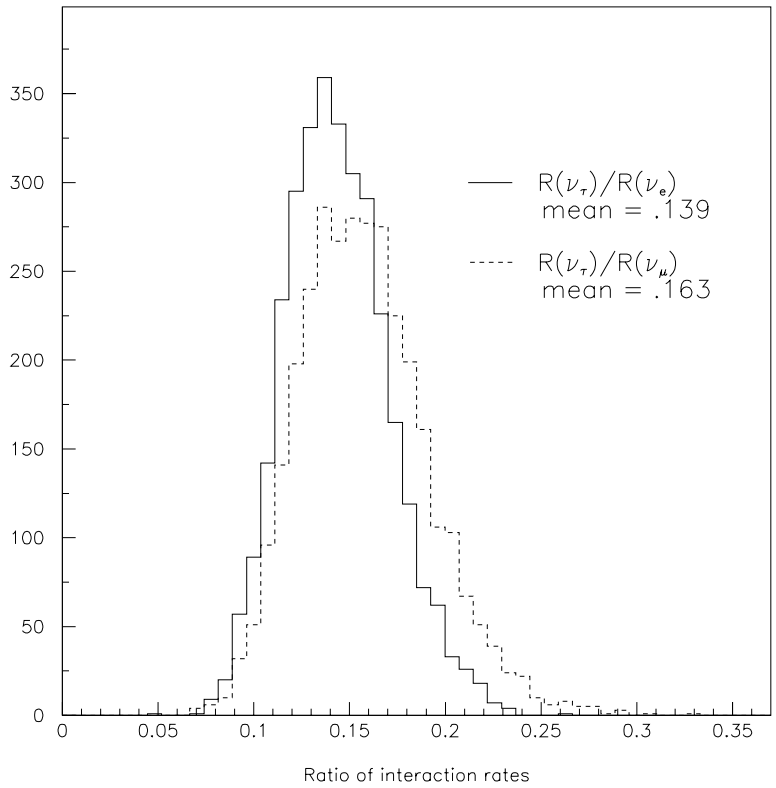

Figure 6-3 Histogram of the ratio of interaction rates: ν_τ to ν_e and ν_τ to ν_μ found using three thousand Monte Carlo simulations to solve Eq. 6-4.

The average of the two results found from N_μ and N_e is 8.6 ± 1.9. The number of ν_μ and ν_e ware not found independently so the uncertainty shown is the larger of the two. The difference in the two results also gives an estimate of the systematic error. The

final result of $8.6 \pm 1.9 \pm 0.9$ (sys.) is consistent with the *a priori* result of 6.9 ± 2.3 shown in Table 6-2. As calculation of the former used measured values, it should be more reliable than the *a priori* calculation, and therefore will be used for the remainder of this thesis.

6.3 Expected number of ν_τ signal events

The expected number of observed tau decays passing all the selection criteria can now be calculated using the number of ν_τ charged-current interactions in the data set, N_τ , the branching ratio for the single charge decay modes, BR_i ,and the fraction of each type of decay which pass the selection criteria, $P_{\text{selection } i}$.

$$N_{signal\ i} = N_\tau \times BR_{\ i} \times P_{selection\ i} \qquad \textbf{Eq. 6-7}$$

Using the total number of expected ν_τ interaction in the data calculated in the previous section, the single charged branching ratios taken from Table 2-1, and the selection efficiency in Table 6-1, the total number of events passing the selection criteria is 3.9 ± 0.95. Table 6-3 shows the expected number of each type of signal event.

Decay mode	Branching ratio (%)	Number of decays	$P_{\text{selection}}$	Number selected
$\nu_\tau \rightarrow$ electron	17.84 ± ..06	1.5 ± 0.4	.55	0.84 ± 0.21
$\nu_\tau \rightarrow$ muon	17.37 ± .06	1.5 ± 0.4	.56	0.84 ± 0.20
$\nu_\tau \rightarrow$ hadron.	50.14 ± .07	4.3 ± 1.0	.50	2.2 ± 0.48
All single charge	85.35 ± .07	7.7 ± 1.8	.52	3.9 ± 0.95

Table 6-3 Expected number of identified τ decays for $8.6 \pm 1.9 \pm 0.9$ ν_τ interactions.

6.4 Backgrounds to the ν_τ events

The number of background events expected is calculated to compare with the number of tau signal events observed and the number of tau events expected.

There are three sources of backgrounds which could contaminate the tau signal; the first is primary tracks incorrectly associated with another track in the emulsion record, the second is primary particles other than taus that undergo single charge decays, and the third are secondary interactions of primary particles which result in only one visible track in the emulsion. All three of these processes result in a kinked track topology which may fake the tau signal. However, these backgrounds only contribute for neutral-current events and charged-current events where the primary muon or electron is not detected.

6.4.1 Random association backgrounds

The first source of background events are instances when a low momentum primary particle (a stopping track from the interaction vertex) is associated with a random track that begins close to where the primary track stops. If the projections of these two tracks appear to intersect their combination can be mistakenly identified as a kink.

The vast majority of particles whose trajectories are recorded in the emulsion are high momentum muons that traverse the entire emulsion stack and thus the scanned volume. The only tracks that actually begin or end in the scanned volume are from delta rays, electron-positron pairs from gamma conversion or low energy particles produced in neutrino interactions that range out before exiting the local scan volume.

The data set, however, contains many tracks, which appear to begin or end in the emulsion record. These are due to inefficiencies in the procedure to link emulsion segments to form tracks. For instance, segments from two almost parallel muons may be linked such that the downstream segments of one are assigned to the upstream segments of the other. This leaves the upstream segments of the first and the downstream of the second as a "stopping" and a "starting" track in the scan volume.

The number of false kinks from this source can be calculated from the density of starting tracks in the data set ($\rho_{\sigma tarting}$), the number of stopping tracks from primary vertices ($N_{stopping}$), the maximum distance allowed for association (r) and the probability that the event passes the tau selection criteria ($P_{selection}$).

$$N_{random} = \rho_{saarting} \times \pi \times r^2 \times N_{starting} \times P_{selection} \quad \textbf{Eq. 6-8}$$

There are 177 stopping primary tracks in all events, including 44 single segment tracks. The average density of starting tracks is found by the software using a area with a radius of 500 μm around the vertex positions and is 3.8 tracks per mm^2. However, the majority of these starting tracks are due to mis-linking of segments as described above and would be identified as such during the manual eye-scan of the emulsion. The fraction of these that are mis-linked and are actually penetrating is estimated using events in which a manual eye-scan of the emulsion was performed. In a separate search ,76 candidate intersections that were identified in the software were eye-scanned and it was found that only 17 were not caused by mis-linked penetrating tracks. The 76 intersection candidates were distributed uniformly throughout the modules and thus $17/76 = 22 \pm 5\%$ represents the average fraction of starting tracks found by the linking-software in the emulsion data which are in fact penetrating. The true density of starting tracks is then $(.22)\times(3.8\ mm^{-2}) = 0.84\ mm^{-2}$. The number of starting tracks which come within 5 microns of all the stopping primary tracks is the total expected number of the random association kinks and is $.012 \times P_{selection}$.

An upper limit on $P_{selection}$ is the fraction of events within the data set which have no muon or electron identified from the primary which represents only one of the tau selection criteria. This fraction is 0.48 and, therefore, an upper limit on the total number of background events in the sample due to random association is $0.012 \times 0.48 = 0.006$ events.

It is noted that this is an upper limit since; firstly the distance of 5.0 μm is approximately 4 times greater than the average distance between parent track and daughter track of the signal events and, secondly, only one of the tau selection criteria are applied.

6.4.2 Decay backgrounds

Another background to the tau signal is the single charge decay of other primary particles. Any particle produced in a neutrino interaction that decays within the scan

volume through a channel producing only one charged daughter will be indistinguishable from a tau decay provided that no detected primary electron or muon. Since the data set contains neutral-current interactions and lepton identification efficiency is not 100% for charged-current interactions this background must be examined.

The most common primary particles that decay are pions and kaons. The majority of the charged tracks from any neutrino interaction are due to pions, however their decay is kinematically forbidden from passing the tau selection criteria. The π's dominant decay mode to $\nu_\mu + \mu$ has an maximum available transverse momentum of 30 MeV/c which is a factor of 8 smaller than the selection limit made on tau decays.

The single–charge kaon decay modes $\nu_\mu + \mu$ and $\pi^0 + \pi^+$ have a maximum transverse momentum of 247 and 205 MeV/c, respectively, and a small over-estimate of the π's or μ's momentum would allow them to be included in the tau sample. However the lifetime of the kaon is long enough that the probability of one decaying within the 5 mm length acceptance interval is very small. The number of a kaons in each of ten thousand simulated ν_e and ν_μ interactions is $\bar{n}_k = 0.31$, and the average momentum is ~8.2 GeV/c. The probability of an 8 GeV/c kaon decaying in 5mm is 6.4×10^{-5}. A conservative upper limit on $P_{\text{selection}}$ is the product of the fraction with no lepton and the fraction of kaon decays within 5 mm: $0.48 \times (6.4 \times 10^{-5}) = 3.1 \times 10^{-5}$. This leads to an estimate of the number of background kaon decays in the data set to be:

$$N_{\text{kaon}} = 203 \times \bar{n}_k \times P_{\text{selection}} = (203) \times (.31) \times (3.1 \times 10^{-5}) = 0.002$$

The only significant source of single charge decay backgrounds comes from the decay of charm particles. This background warrants thorough analysis and is the subject of the next section. The production and decay of bottom particles is a negligible source of background due to the small production cross-section: it is ~ 1000 times smaller than that of the charm particles [35]

6.4.3 Charm decay backgrounds.

The charmed particles produced in ν_e and ν_μ charged-current interactions are the largest source of background to the tau signal. The charmed mesons, D and D_s, and the baryon Λ_c all have masses and lifetimes similar to the tau's and all have a significant fraction of single charge decay modes [27]. The masses of the D^+, D_s and Λ_c are 1869.3 ± 0.5, 2112.4 ± 0.7 and 2284.9 ± 0.6 MeV/c^2 respectively, while the tau's is 1777.03 ± 0.3 MeV/c^2. The lifetimes of the D^+, D_s and Λ_c are 1.051 ± 0.013 , 0.496 ± 0.010 and 0.206 ± 0.012 picoseconds, while the tau's is 0.2906 ± 0.0011 picoseconds. The single chare decay modes are shown in Table 6-4 and

Table 6-5. Charm particles are produced in approximately 7% of the neutrino interactions at E872 energies which is close to the same rate as tau production.

Although charm production is possible in neutral-current interactions, the cross-section is small and therefore this process contributes negligibly to the charm background. The neutral-current cross-section for a charm anti-charm pair is 0.002 of the charged-current charm cross-section [36].

The number of charm decay backgrounds from charged-current interactions is given by Equation 6-9

$$N_{Charm} = N_{cc} \cdot \sum_i \left(\int F_i(E) \cdot \frac{dN}{dE} dE \times BR_i^{1-charge} \times P_i^{selection} \right) \qquad \textbf{Eq. 6-9}$$

Here N_{cc} is the number of charged-current interactions in the data set, the index i represents one of three charm particles [D D_s or Λ_c], F_i is the fraction of neutrino interactions producing the charm species i, $BR^{1\text{-charge}}$ is the single charged decay branching fraction, and $P^{selection}$ is the probability that the charm decay will pass the tau selection criteria. Since the rate of charm particle production varies with energy, it is found by integrating over the energy spectrum of the interacting neutrinos.

The number of background events from charm decay is calculated from the total number of each type of charm particle produced and then simulating their decay to find

the fraction which pass the tau selection criteria. The inputs to Equation 6-8: F_i , $P^{selection}$, and N_{cc}, $BR^{1\text{-charge}}$ are discussed below.

D_s meson	
Channel	Frac. (%)
K^0 e ν_e	6.7 ± . 9
K^0 μ ν_μ	7 .0 ± 3
$\overline{K}^*(892)^0$ μ ν_μ	1.6 ± . 2
$\overline{K}^*(892)^0$ e ν_μ	1.5 ± . 2
$\overline{K}^*(892)^0 \pi^0$ μ ν_μ	<.4
$\overline{K}^*(892)^0 \pi^0$ e ν_e	<.4
φ μ ν_μ	< 1.3
φ e ν_e	<.8
π^0 μ ν_μ	.3± . 1
π^0 e ν_e	.3± . 1
η μ ν_μ	<.3
η e ν_e	<.3
$K^0 \pi^+$	2.9 ± . 3
$\overline{K}^*(892)^0 \pi^+$	.6 ± . 07
$a(1430)^0\pi^+$	1.2 ± . 1
$\pi^+\pi^0$	.2 ± . 07
$K^0 K^+$	.7 ± . 1
φ π^+	.6 ±. 06
$\overline{K}^*(892)^0 K^+$	.3 ± . 05
$\overline{K}^0 \pi^0 \pi^+$	1.3 ±. 1.1
$\overline{K}^0 \overline{K}^0 K^+$	1.8 ± . 8
$\overline{K}^*(892)^0\pi^0 \pi^+$	1.4 ± . 5
$\overline{K}^0\rho^+$	6.6 ± . 2.5
$\overline{K}^0 K(892)^+$	3.2 ± 1.5
$\overline{K}^*(892)^0 \rho^+$	.7 ± . 4
$\overline{K}^0$ a(1260)	.4 ± . 09
$\overline{K}^*(892)^0 K(892)^+$	.9 ± . 4

D^+ meson	
Channel	Frac. (%)
η e ν_e	1.8 ± .2
η μ ν_μ	1.8 ± .2
. $\tau\nu_\tau$	6.3 ± . 4
. $\mu\nu_\mu$	.5±. 2
φ μ ν_μ	.7±.2
φ e ν_e	.7±.2
$\overline{K}^0 K^+$	3.6 ± 1.1
φ π^+	1.2 ± . 3
$K(892)^0 K^+$	1.1 ± . 3
$f(980)^0 \pi^+$	.6 ± . 3
η π^+	1.2 ± . 3
η(958) π^+	.6 ± . 2
$\overline{K}^0 K^*(892)^+$	4.3 ± 1.4
η $\pi^0\pi^+$	3.1 ± . 3
$\overline{K}(892)^0 K^*(892)^+$	1.9 ± .8
ρ^+ η	7.7 ± 2.2

Table 6-4 Single charge decay modes of the D_s and D^+ mesons. For modes that contain resonances or particles that decay strongly, the fraction has been scaled to the decays which result in one charged particle.

Λ_c baryon	
Channel	Frac. (%)
$\Lambda\ \eta\pi^+$	1.3± .4
$\Lambda\mu\nu_\mu$	2.0 ± .7
$\overline{K}^0$ p	2.3 ± . 6
$\overline{K}$*(892)^0 p	.5 ± . 1
$\overline{K}^0\pi^0$ p	3.3 ± 1.0
$\overline{K}^0\pi^0\eta$	.8 ± .3
$\Lambda\pi^+$	.9± .3
Λ K^0 $\overline{K}^+$	.6± .2
$\Sigma\pi^+$	1.0± .3
$\Sigma\pi^+\pi^0$	1.8± .8
$\Sigma^+\pi^0$	1.0± .3
$\Sigma^+\eta$	.4 ± .2
Ξ K$^+$	.4 ± .1

Table 6-5 Single charge decay modes of the Λ_c baryon.. For modes that contain resonances or particles that decay strongly, the fraction has been scaled to the decays which result in one charged particle.

Number of charged current interactions: N_{cc}

The total number of charged-current ν_μ and ν_e events in the data set has been calculated in Section 6.1. and are 95 ± 14 and 59 ± 6, respectively, or the total number of charged-current interactions is thus 154 ± 15.

Charm production fraction: F_i

The LEPTO event generator [32] was used to estimate the rate of charm particle production in neutrino-nucleon interactions. The ratio of charm particle production to the total neutrino charged-current interaction rate is shown in Figure 6-4 using bins of 5GeV for neutrino energy, ranging from 0 to 250GeV. The LEPTO output was scaled by 1.15 to match the results of two experiments that have measured the total charm

production in neutrino interactions. When this distribution is integrated over the energy spectrum for E872's neutrino beam, the average charm particle production fraction is .066±.008. This total includes both neutral and charged charm. Since the charm decay background only results from charged charm decays the distribution of charm particle species which are produced must be known.

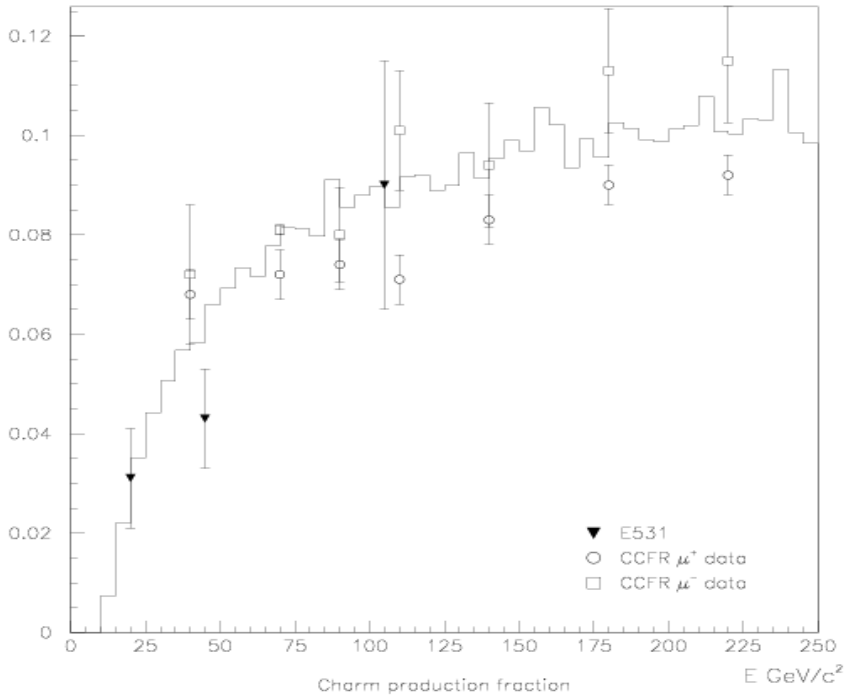

Figure 6-4 Total charm production in neutrino-nucleon interactions. The results of the LEPTO simulation and two experiments are shown.

The relative production fractions for different charm species were measured in E531 and recalculated [37] using an improved measurements of the D, D_s and Λ_c lifetimes [27]. For charm produced at E872 energies these fractions are .57± .10, .24 ± .06 .09 ± .03 and .10 ± .03 for D^0, D, D_s and Λ_c respectively.

Single charge charm decays : *BR* $^{1\text{-charge}}$

The fraction of charm particles that decay through single charge decay modes are shown in Table 6-4 and

Table 6-5. Summing the listed values results in 43.7 ± 4.6% for the D meson and 38.6 ± 3.1% for the D_s meson. A direct measurement of single charge decays for charmed meson by MARKII [38] gives 38.4 ± 3.2% for the D and 37 ± 10% for the D_s. In order to calculate a conservative upper limit for the number of charm decay background events, the values from summing individual modes are used.

The branching fractions of the Λ_c baryon have not been studied as thoroughly as the D and D_s. In order to define a fraction of single charge decays one can calculate the sum of the fractions of multi-prong decays that have been measured and subtract this number from one. The sum of Λ_c decays resulting in more than one charged particle is 35.4 ± 3.7% giving an upper limit to the single charge branching fraction $BR^{1\text{-charge}}$ = 64.6 ± 3.7%. The measured single charged decays are scaled such that the sum is equal to 64.6%.

Fraction of charm decays passing tau selection criteria: $P^{\text{selection}}$

A simulation of charm particle decay is used to find the fraction of charm decays which fulfill the tau selection criteria and can fake the tau signal. The decay modes used in the simulation are those listed in Table 6-4 and Table 6-5.

A large set of neutrino interactions simulated with the LEPTO event generator are used. Interactions that produce charm particles are propagated through the detector and those events triggering the spectrometer are then subjected to the tau selection criteria. The fraction of triggering events that pass the selection criteria gives $P^{\text{selection}}$.

Simulation of primary muon identification in ν_μ charged-current events producing charm is straight-forward: identification is done on an event-by-event basis using the minimum of four collinear hits in the muon identification system. One hundred thousand charm events were simulated and the fraction which triggered the spectrometer and did not have their muon identified was found to be 0.25 for 'prompt' ν_μ and 0.35 for 'non-prompt'. The overall fraction of all expected ν_μ charged-current interactions that do not have their primary muon identified is 0.31

For ν_e events, the detection of the primary electron is not simulated on an event-by-event basis. Instead the fraction of events whose primary electron is not identified is

estimated for all ν_e charged-current interactions that produced charm. It is assumed that electron identification is only done through detection of e^+/e^- pairs, and the fraction ν_e events that produce charm and whose primary electron does not pair produce before the end of the target module is found. The vertex positions of the found events are known, thus the distribution of the amount of material downstream in the module are known. By integrating over this distribution, the average probability that a primary electron does not pair produce and is not identified is 0.30.

The composition of the neutrino beam used in the simulated interactions is that found in sections 6.21 and 6.2.2; the ratio of ν_e to prompt ν_μ equals 59/58 and the ratio of prompt ν_μ to non-prompt ν_μ equals 58/(113-58). For one hundred thousand simulated charm events of each species , the average fraction of decays meeting the tau selection criteria are 13.2%, 13.8% and 9.6% for D, D_s and Λ_c respectively. The slightly lower fraction of Λ_c passing the selection is due to their shorter lifetime; a greater fraction of these decays are not long enough to fulfill the single visible segment requirement.

	D	D_s	Λc	All charged charm
# produced	2.54 ± 0 .70	0.97 ± 0.35	1.01 ± 0.33	4.5 ± 0.9
BR→ 1-charge	0.46 ± .03	0.37 ± .03	0.65 ±.04	-
$P_{\text{selection}}$	0.132	0.138	0.096	-
# of background events	0.154	0.043	0.063	0.27 ± .04
Charm → electron	0.029	0.0033	0.0020	0.034 ± .006
Charm → hadron	0.029	0.0040	0.0020	0.041 ± .007
Charm → hadron	0.096	0.036	0.059	0.191 ± .038

Table 6-6 Number and type of expected backgrounds from charm decay in the set of 203 located neutrino interactions

Table 6-6 shows the expected number of each type of charged charm particle produced, the number decaying through single charge modes resulting in an electron , a muon or a hadron, and the fraction of those decays that pass the tau selection criteria and are background events.

In all, the total number of backgrounds from charm decays is 0.27 ± 0.04

6.4.4 Secondary interactions of a primary particle

Background events may also result from the interaction of a primary particle. If the interaction is elastic, or if only one resulting particle is detected, the observed topology is identical to that of a kinked track. This background is dominated by hadronic interactions and, like any background, only occurs in events in which no primary electron or muon is detected.

The number of background events due to Coulomb multiple scattering is limited by the maximum amount of material between any two measurements of a particles trajectory. The 1mm steel plates in the ECC type targets correspond to 0.057 radiation lengths and the probability of a particle undergoing multiple scattering resulting in trajectory change which passes the tau selection criteria is very small. The plastic bases of ECC sheets are 5.8×10^{-4} and 2.3×10^{-3} radiation lengths for ECC200 and ECC800, respectively. A Monte Carlo simulation of Coulomb multiple scattering of primary particles was performed to estimate the number of this type of background event. Multiple scattering of five hundred thousand primary particles from all types of neutrino interactions were propagated through 1mm steel with the GEANT detector simulation and the angular deviation was recorded. As with all simulations, the momentum of the particle was smeared with a Gaussian distribution of $\sigma(\Delta p/p) = 30\%$ to account for the uncertainty in the measurement. Figure 6-5 shows the transverse momentum distribution for all scatters greater than 10 mrad and a momentum of greater than 1 GeV/c. These requirements correspond to two of the tau selection criteria.

From this set, only 4 events having a scatter of more than 250 MeV/c were found that passed the above criteria. This gives an average number of scatters per millimeter of steel, $R_{\mathrm{Fe}} = 8.0 \times 10^{-6}$/mm

The number of background events from multiple-scattering can then be calculated:

$$N_{multiple\_scatter} = L_{Fe} \times R_{Fe} \times P_{selection} \qquad \textbf{Eq. 6-10}$$

$$= 1320 \text{ mm} \times 8.0\text{x } 10^{-6}/\text{mm} \times 0.48 = .005 \text{ events.}$$

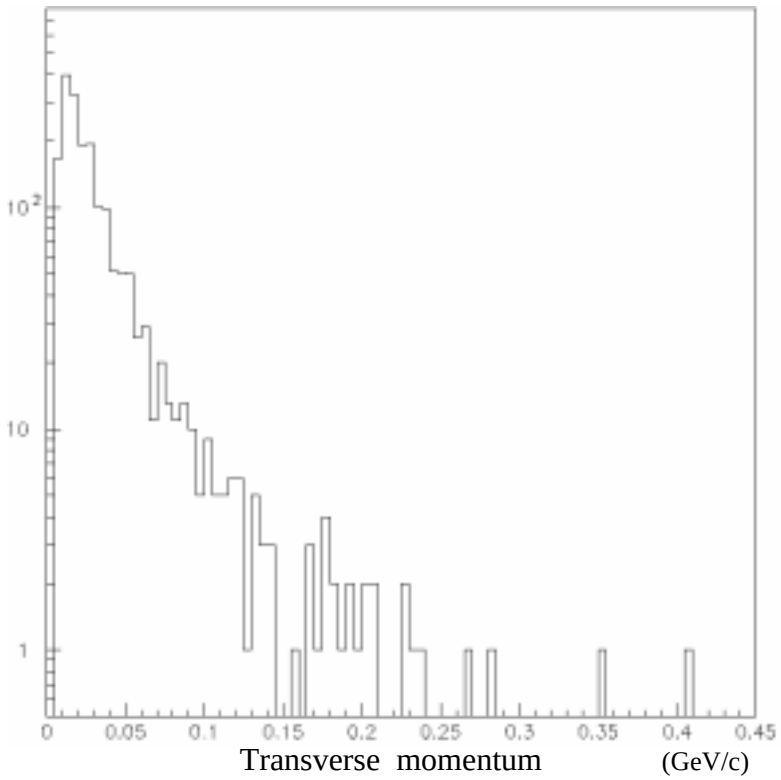

Figure 6-5 Distribution of transverse momentum for 500,000 primary particles traversing 1 mm of steel. Only those with angular deviations greater than 10 mrad are shown.

In this equation L_{Fe} is the total path length of all tracks in steel, R_{Fe} is the number of scatters per meter of steel and $P_{\text{selection}}$ in this case is the probability of an interaction having no identified electron or muon. The number of multiple scatters in the plastic bases of the target is only a small fraction of this number since, compared to the steel, they represent only a fraction of the number of radiation lengths.

A hadronic interaction may also fake a tau decay if the interaction results in only one visible particle in the emulsion record. For interactions occurring within the bulk emulsion this is limited to elastic collisions which do not result in nuclear fragmentation. Usually these interactions result in many short tracks that are caused by nuclear break up. These short tracks are clearly visible in the emulsion when viewed by eye and thus

these types of interactions cannot be mistaken as decays. However, in some instances the nucleus remains intact and it is possible for the interaction to result in only one track. In bulk emulsion these are the only types of hadronic interactions that can result in a background.

For interactions that occur in the steel plates or plastic base, it is possible for only one track to be visible even when nuclear fragmentation occurs. Low momentum fragments may range out before reaching an emulsion layer and, thus, only the high momentum hadron is visible in the emulsion. If this occurs, the kink caused by the deviation of the hadron's trajectory can be mistaken as a decay and may result in a background.

Since the probability of interaction is proportional to the path length through the target material, the number of backgrounds of this type depends on the total length of all the primary tracks scanned. The number of background events from this source, N_{int} is estimated from a combination of this length, the probability of a individual hadron undergoing an interaction that results in a single observable particle, and the probability of the observed kink passing the selection criteria.

$$N_{\text{int}} = \frac{L_{primary}}{MFP_{1-charge}} \times P_{selection} \qquad \textbf{Eq. 6-11}$$

In this equation $MFP_{\text{1-charge}}$ is the mean-free-path between interactions resulting in only one charged track, $L_{\text{primaries}}$ is the total length of primary tracks and $P_{\text{selection}}$ is the probability of passing the selection criteria.

There are 923 primary tracks in the data set. Since only kinks occurring after the first emulsion measurement and within 5 mm of the interaction vertex pass the selection criteria, the relevant path length is from the first emulsion sheet downstream of the interaction vertex to a distance of 5 mm. For the 923 primary tracks, the sum of these lengths is 427 cm. The total distances in different materials for all events is shown in Table 6-7. This total is an over-estimate of total effective path length of hadrons, since for all charged-current interactions there is at least one lepton in the event.

Material traversed by primary tracks	Path length (cm)
ECC TargetModules	
Fe	171.7
Acrylic Base	74.7
Emulsion	28.0
Bulk Target Modules	
Acrylic Base	14.1
Emulsion	105.5

Table 6-7 Total path lengths of primary tracks in lengths in the different target materials

Hadronic interactions in bulk emulsion

In bulk sections of the target modules, an interaction must result in 'white star' kink to be a background. A 'white star' kink is an interaction in which there is no detectable nuclear fragmentation and the only final track visible is that of the initial hadron. These types of interactions appear in emulsion as kinks and are indistinguishable from single charge decays.

White star kinks were studied in the CHARON[39] emulsion experiment and it was found that the average mean-free-path between these kinks in a bulk emulsion target is 134±90, 47± 16 and 49±18 meters for 2GeV/c 3Gev/c and 5GeV/c pions respectively. These mean-free-paths represent kinks which have a transverse momentum greater than 250MeV/c which is the same as the selection criteria used in this analysis. For the expected spectrum of primary hadrons in this experiment, the average mean-free-path is 47 ± 21 meters.

The probability of a white star interaction rapidly decreases with P_T so an upper limit on the number of interaction passing the selection cuts is found using the limiting value of 250MeV/c for kinks of this type. An upper limit on the total number of background events due to interactions in the bulk emulsion as with equation 6-11:

$$\frac{L_{bulk}}{MFP_{white-star}} \times P_{selection} = (1.38\text{m}) / (47 \pm 21\ \text{m}) \times (0.48) \qquad \textbf{Eq. 6-12}$$

$$= 0.014 \pm 0.006 \text{ events}$$

Here L_{bulk} is the total path length of primary particles in emulsion, $MFP_{\text{white-star}}$ is the mean-free-path of 'white star' kinks found in CHARON, and $P_{\text{selection}}$ is taken as the fraction of events with no muon or electron. It is noted that the CHARON data is limited to pions of 5GeV/c or less whereas the expected distribution of hadrons resulting from neutrino interaction in E872 has a large tail of higher energy particles (~ 40 % have an energy greater than 5GeV). It is assumed here that the mean-free-path for particles of greater momentum is equal to those in the 5GeV/c measurement.

Hadron interactions in ECC targets

In the acrylic and steel of the ECC targets, background events may be caused by 'white star' interactions as well as interactions in which other hadronic activity does exists but is sufficiently small as to not produce a detectable track in the next downstream emulsion layer. The majority of an ECC's mass and volume is due to steel and it is possible for low energy tracks from a hadronic interaction occurring in the steel to be undetected in the adjacent emulsion. These type of interaction are termed 'gray star' and were also studied by CHARON.

In the CHARON experiment, 'gray star' kinks were defined as any interaction that contained a visible blob, nuclear recoil or Auger electron leaving the interaction point and only one high energy particle coming from the interaction point The mean-free-path of these types of interactions resulting in a P_t of greater than 250MeV/c was measured to be 14±4 , 27± 9 and 23±13 meters for 2, 3, and 5 GeV/c pions respectively. The effective mean-free-path for hadrons from the neutrino interactions in E872 is calculated in the same manner as white star kinks, convoluting the expected primary hadron spectrum with these mean-free-paths. The result is $\text{MFP}_{\text{grey-star}} = 21 \pm 8$ m in emulsion.

To translate these results to the ECC environments the mean-free-paths of the target in the CHARON experiment are scaled to that of the E872 target material.

CHARON's target consisted of bulk type emulsion which corresponds to a longer mean-free-path than in steel and a shorter mean-free-path than in acrylic. The mean-free-path for a nuclear interaction process occurring in a mixture is found by taking the weighted sum of the interaction cross-section and scaling by the density;

$$\lambda_j^{-1} = \mathrm{N_A} \cdot \sum_i w_i \cdot \sigma_i \cdot \mathrm{A}_i^{-1} \qquad \textbf{Eq. 6-13}$$

$$MFP_j = \frac{\lambda_j}{\rho_j} \qquad \textbf{Eq. 6-14}$$

Here N_A is Avagadro's number, w_i is the fraction of the weight associated with nucleus i and A_i is the atomic weight. The cross-section for a nuclear interaction scales as A^{α} where α is measured to be .77.[40] The ratio of mean-free-paths becomes:

$$\frac{MFP_J}{MFP_{Emul}} = \frac{\rho_{Emul} \cdot \sum_i^{Emul} w_i \cdot \mathrm{A}_i^{1-\alpha}}{\rho_J \cdot \sum_i^{J} w_i \cdot \mathrm{A}_i^{1-\alpha}} \qquad \textbf{Eq. 6-15}$$

Here ρ_j is the density of material *j* in g/cm^3. Besides emulsion, the two other materials in ECC target plates are the acrylic base which has a density of 1.18gcm^{-3} and steel which has a density of 7.87 gcm^{-3}. The composition of emulsion is given in Table 3-3

The mean-free-paths of 'whitestar' and 'gray star' kinks are calculated for acrylic and steel using the results for emulsion measured by CHARON. The results are listed in Table 6-8. In acrylic and steel both 'white star' and 'gray star' kinks can result in background events. Therefore, for these materials the mean-free-path of a background kink is the sum of 'white star' and 'gray star' mean-free-paths.

	Emulsion (m)	Fe (m)	Acrylic (m)
White star	47 ± 21	22 ± 10	88 ± 40
Gray star	21 ± 8	9.6 ± 3.9	40 ± 16
Background kink	47 ± 21	6.7 ± 2.7	27 ± 11

Table 6-8 Mean-free-paths of white star and gray star kinks for the target material.

Using these mean-free-paths and the total path length in each material the number of expected backgrounds from interactions in steel and acrylic can now be calculated with Equation 6-10. The results are $N_{\mathrm{Fe}} = .12 \pm .05$ and $N_{\mathrm{acrylic}} = .014 \pm .006$

These calculations assume only that no muon or electron is seen in the event, and that the P_t of the interaction is greater than 250 MeV/c. These represent two of the tau selection criteria and therefore the results are an upper limits on the number of expected interaction backgrounds.

Simulation of hadron interaction background in ECC targets

Simulations of hadrons interacting in an ECC type target are also used to estimate the number of hadronic interaction background events.

The simulations use a spectrum of pions, protons and kaons derived from neutrino-nucleon interactions using the LEPTO event generator[32]. The particles are transported through three plates of ECC800 material and the interactions are simulated with the GEISHA[33] hadronic interaction simulator. The automated emulsion scanning is simulated by recording the position of all charged particles if they completely traversed 100 microns of any emulsion sheet. As with the automated scanning, only track segments less than 400 mrad from the normal to the emulsion plate were recorded. The primary interactions were assumed to occur only in the steel of the ECC type module and were therefore uniformly distributed throughout.

Background events are selected from these simulated interactions if: 1) they have one and only one recorded segment downstream of the interaction position and 2) the track causing the recorded segment differs in angle by more than 10 mrad from the trajectory of the primary hadron. The final momentum of the simulated hadron is

smeared by a Gaussian distribution with an width $\sigma(\Delta p/p) = 30\%$ to account for the resolution of the momentum measurement. The remaining selection criteria on impact parameter and momentum of the resulting particle are then applied to the events.

Simulated charged-current events [5.7 M tracks]		
	Steel	Acrylic
Total path length	11300 m	11500 m
Number of kinks	1473	463
Kinks/m	.130 ± .003	.040 ± .002
Simulated neutral-current events [1.0 M tracks]		
	Steel	Acrylic
Total path length (m)	1990	2020
Number of kinks	270	71
Kinks/m	.136± .008	.035±.004
Average mean-free-path (m)	7.63 ± .017	25.6 ± 1.3

Table 6-9 Number of kinks found in simulated hadronic interactions occurring within ECC steel plates

Since the steel in the ECC800 is the same thickness as in the ECC200 it follows that the number of kinks per meter in steel calculated with the simulation using ECC800 is the same for the ECC200. The plastic base of the ECC200 is thinner than that of the ECC800 and there is less material in which a particle created in an interaction can range out before being detected in the emulsion layer. Therefore it is more likely for gray star interactions within the plastic to be identified by low momentum tracks in ECC200 than ECC800. For this reason, the number of kinks calculated per meter found using ECC800 is a conservative upper limit on the expected value in ECC200.

The total number of background events of this sort is calculated in the same manner as the previous section, using equation 6-10 with the mean-free-path found in the Monte Carlo simulation and the total path length shown in. The number of background events are: $N_{\mathrm{Fe(simulation)}} = .107$ and $N_{\mathrm{acrylic(simulation)}} = .014$

This number of expected background events due to hadronic interaction is consistent with the calculation using CHARON's results which are N_{Fe} = .12 ± .05 and $N_{acrylic}$ =. 015 ± .006. The Monte Carlo calculation incorporates all of the tau selection criteria and is thus it's results will be used for all further calculations.

6.4.5 Summary of background events

The number of background events expected from the random association of tracks, from single charge decays and from secondary interaction of primary particles is summarized in Table 6-10. The total of 0.41 ± 0.04 expected background events gives a signal to background ratio ~10.

Background Source	N_{kinks}	$P_{selection}$	comment	$N_{background}$
Random association	.012	.48	Measured track density	<0.006
Light meson decay	.004	.48	Monte Carlo	<0.002
Charm → electron	.29	.10	Monte Carlo	0.034 ± 0.007
Charm → muon	.29	.10	Monte Carlo	0.041 ± 0.008
Charm → hadron	1.51	.10	Monte Carlo	0.191 ± 0.04
Multiple scatter	.011	.48	Monte Carlo	<.005
Interaction: Bulk	.017	.48	CHARON data	0.016 ± 0.005
Interaction: Fe	.223	.48	CHARON and Monte Carlo	$0.107 \pm 2 \times 10^{-4}$
Interaction: Acrylic	.031	.48	CHARON and Monte Carlo	$0.015 \pm 8 \times 10^{-4}$
Total				0.41 ± 0.04

Table 6-10 Summary of expected backgrounds to tau signal

6.5 Expected and observed number of signal events

The expected number of observed ν_τ events is 3.9 ± 0.95 as shown in section 6.3 while the expected number of background events due all sources is 0.41 ± 0.04. The total predicted signal is thus:

$N_{\text{signal (predicted)}} = N_{\text{tau}} + N_{\text{background}} = \ 4.3 \ \pm \ 1.0$ events

The number of observed signal events in the data set is 4, and is in good agreement with the expectation of 4.3 ± 1.0.

To compare the prediction with the observation, the probability of observing 4 or more events when the expected signal is 4.3 is calculated using Poisson statistics:

$$P(N_{observed} \geq 4 \mid N_{predicted}) = \sum_{n=N_{obs}}^{\infty} e^{-N_{predicted}} \frac{N_{predicted}^{n}}{n!} \qquad \textbf{Eq. 6-16}$$

Assuming that the uncertainty on the predicted number of signal events is Gaussian, it can be include in the calculation of this probability by modifying Equation 6-14:

$$P(N_{observed} \geq 4 \mid N_{predicted}) = \int_{0}^{\infty} \left[\frac{1}{\sqrt{2\pi\sigma}} \cdot e^{\frac{-(x-N_{predicted})^2}{2\sigma^2}} \sum_{N_{observed}}^{\infty} e^{-x} \frac{x^n}{n!} \right] dx \qquad \textbf{Eq. 6-15}$$

In this expression $\sigma = 1.0$ is the uncertainty in the total number of predicted signal events. The result is $P(N_{\text{observed}} \geq 4 \mid 4.3 \pm 1.0) = \ 0.60$.

A simple estimate of the probability that all four observed signal events are from background sources and that no ν_τ events were observed can be found with a Poisson distribution with a mean equal to the number of expected background events:

$$P(N_{observed} \geq 4 \mid \mu = 0.41) = \sum_{n=N_{obs}}^{\infty} e^{-\mu} \frac{\mu^n}{n!} \quad = \ 4.04 \times 10^{-4}$$

It can be concluded from this small probability that it is highly unlikely all four of the observed events are from sources other than ν_τ interactions and that consequently at least one ν_τ charged-current interaction has been observed. Nevertheless, since the number of signal events is small, a more detailed analysis of each event as to whether it is

from a ν_τ or background source is possible. An individual analysis of all four signal events is the subject of the next chapter.

7 Discussion of result

Since the number of signal events is small, it is practical to examine each event individually and to evaluate the probability of it being caused by a ν_τ interaction or a background process. The advantage of this approach is that more information about the event can now be taken into account than was used for the tau event selection. It is possible to calculate the probability that an individual event is due to a tau decay or a background since some characteristics which were not used in the tau selection process effect the likelihood that the event is caused by a specific type of background process. This evaluation is the subject of this chapter.

The analysis is done in two steps. The first step is to calculate the likelihood that each signal event is consistent with a tau decay and is a measure of the absolute probability that the event caused by a ν_τ interactions. The second step is to calculate the relative probability that each event is caused by a tau and not a background.

7.1 Likelihood of tau decay

The likelihood that a signal event is caused by a tau decay is estimated by comparing it with a large set of simulated ν_τ events. The signal event is characterized by a set of three parameters (discussed below) and the fraction of simulated events which are less likely than one having the same values of the parameters measured in the signal event quantifies the likelihood that the signal event is consistent with a ν_τ interaction.

For this analysis the parameters used to characterize each event are; the polar angle imbalance, $\Delta\Phi$, the production angle of the tau, $\Theta_{prim,}$ and the decay length L_d. All these parameters are independent of the decay of the tau and therefore compliment the tau event selection criteria which were based on the topology of single charge decays. These parameters rely only on measurements made with the emulsion data and are therefore precise.

The polar angle imbalance is a measurement of the momentum balance between tau lepton and all other particles created in neutrino-nucleon charged-current interactions. Conservation of momentum requires that the sum of the transverse momentum of the tau and all other primary particles must be equal as illustrated in Figure 7-1. The polar angle of each track is measured using the projection of the unit momentum vector onto the transverse plane. The polar angle imbalance of the event is defined as the difference between the polar angle of the tau track and the average polar angle for all other tracks. These definitions are shown in Eq. 7-2 and 7-3.

$$\Phi_i = Tan^{-1}\left(\frac{\tan\theta_y}{\tan\theta_x}\right) \qquad [\theta_y \geq 0]$$

$$\Phi_i = Tan^{-1}\left(\frac{\tan\theta_y}{\tan\theta_x}\right) + \pi \qquad [\theta_y < 0] \qquad \textbf{Eq. 7-1}$$

$$\Delta\Phi = Tan^{-1}\left(\frac{\sum_{i\neq\tau}\sin\Phi_i}{\sum_{i\neq\tau}\cos\Phi_i}\right) - \Phi_\tau \qquad \textbf{Eq. 7-2}$$

This method is used since it is impossible to measure the momentum of the particles coming from an interaction and use strict momentum conservation.

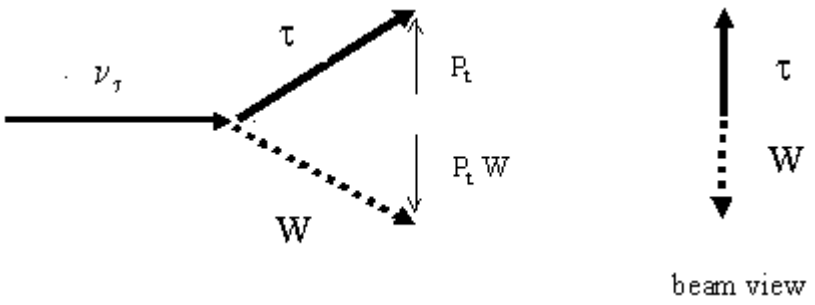

Figure 7-1 Transverse momentum balance between the tau and other particles produced in the event

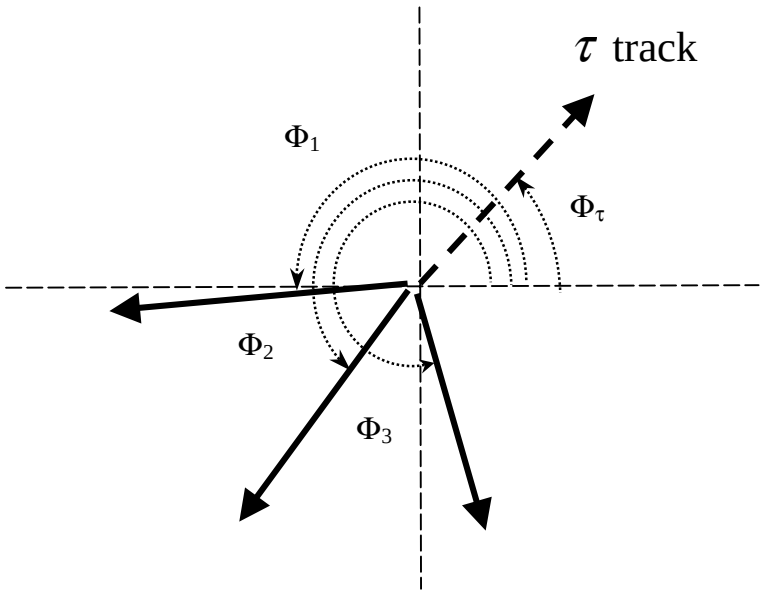

Figure 7-2 Definition of phi angle for primary tracks. The view is along the beam direction.

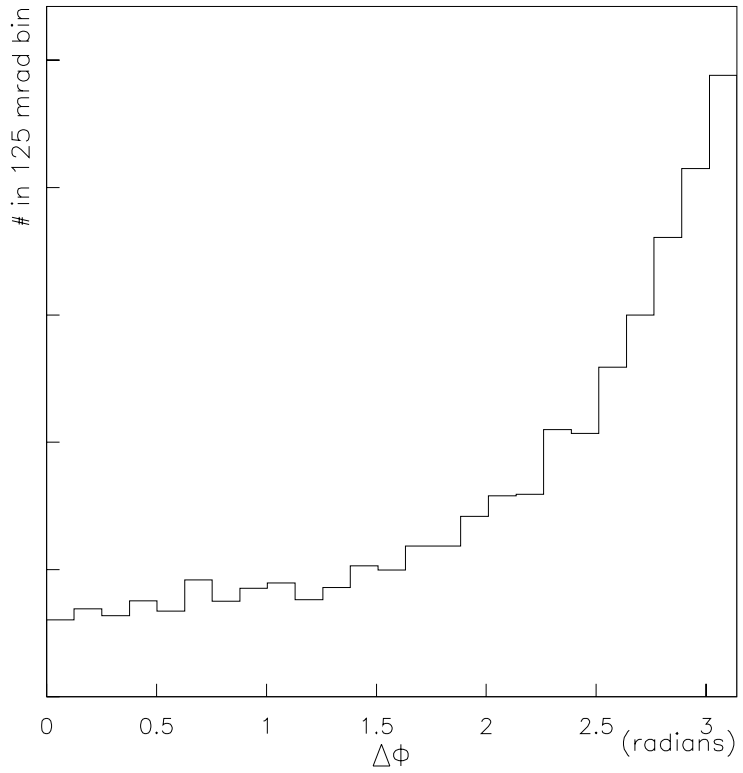

Figure 7-3 Distribution of polar angle imbalance for tau tracks in simulated events

The distribution of $\Delta\Phi$ calculated in this way is still sharply peaked at π radians as shown for Monte Carlo simulated events in Figure 7-3. The uncertainty in the value of $\Delta\Phi$ is due to the uncertainty of the Φ measurement which depends on the absolute angle of the track relative to the neutrino direction. An estimate of the uncertainty in the polar angle difference, $\sigma(\Delta\Phi)$, is the uncertainty in the average polar angle, $\sigma(\overline{\Phi})$ using all tracks in the event. For the entire set of 203 interactions, the average of the uncertainty in $\overline{\Phi}$ was found to be $\langle\sigma(\overline{\Phi})\rangle$ = 9 mrad. Therefore the average uncertainty in the polar angle difference is $\langle\sigma(\Delta\Phi)\rangle \approx$ 9 mrad.

The second parameter used, Θ_{prim} is the angle between the neutrino and the tau . The primary angle is defined as:

$$\Theta_{prim} = \cos^{-1}\left(\hat{P}_{tau} \circ \hat{P}_{neutrino}\right) \qquad \textbf{Eq. 7-3}$$

The production of taus in high-energy ν_τ charged-current interactions is mainly in the forward direction giving a distribution of $\Theta_{primary}$ that is peaked near 0. The neutrino direction is calculated from the position of the interaction in the emulsion module and the center of the beam dump where all neutrinos are assumed to originate. This assumption introduces a maximum uncertainty of 1.5 mrad for events occurring in the outer edge of the target. The distribution of Θ_{prim} for taus in simulated ν_τ interactions is shown in Figure 7-4.

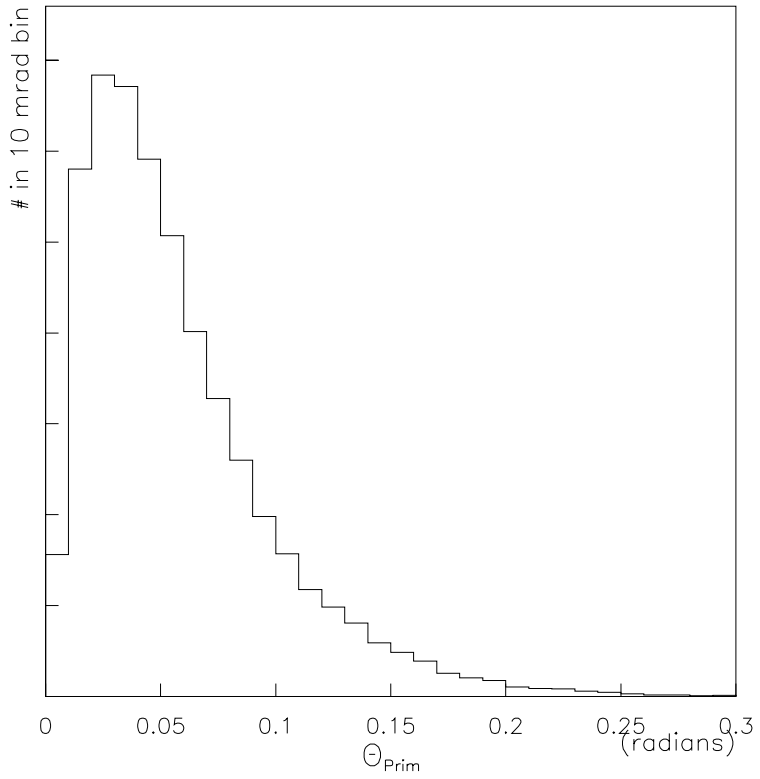

Figure 7-4 Distribution of primary angle for simulated taus

The third parameter is the decay length of the tau. The decay length has been discussed in section 5.1 and the distribution of decay lengths is shown in Figure 5-2.

7.1.1 Probability density and likelihood

The probability of finding an event within a small volume of parameter space is defined by Equation 7-6

$$P[\vec{x}, \vec{x} + \delta x] = \Pi(\vec{x}) \cdot |\delta x| \qquad \textbf{Eq. 7-4}$$

Here $\vec{x}$ is the vector of the three parameters $\Delta\Phi$, Θ_{prim} and L_d and $\Pi(\vec{x})$ is the probability density at $\vec{x}$. The probability density $\Pi(\vec{x})$ is found from the probability by :

$$\Pi(\vec{x}) = \lim_{\delta x \to 0} \frac{P[\vec{x}, \vec{x} + \delta x]}{|\delta x|} \approx \frac{P[\vec{x}, \vec{x} + \Delta x]}{|\Delta x|} \qquad \textbf{Eq. 7-5}$$

To find the fraction of events which are less likely than those at a given $\vec{x}$, one integrates over all parameter space where the probability density has a value that is less than $\Pi(\vec{x})$. This process is analogous to constructing a confidence region in a multi-dimensional space. In this analysis the probability density is found using a large set of simulated ν_τ interactions.

Each generated tau event has an associated weight that corresponds to the product of probability of neutrino generation and interaction. The probability of generation is the likelihood that the neutrino would have the trajectory assigned by the simulation given the available phase space available. The probability of interaction is proportional to the neutrino's interaction cross-section which increases with neutrino energy. The precise relation between cross-section and energy is discussed in Appendix A. For this analysis one billion simulated events were used to fill a parameter space spanning 50 bins in $\Delta\Phi$ from 0 to π, 100 bins in θ_{prim} from 0 to 400 mrad and 200 bins in L_d from 0 to 2cm. The weights of all events in each bin are summed and the probability density of the bins are then calculated by Equation 7-6

$$\Pi(\vec{x}) = \frac{\sum_{in\_i} weight}{voume_i \times \sum_{all} weight} \qquad \textbf{Eq. 7-6}$$

The fraction of events that are less likely than the one at $\vec{x}$ is found by summing the weights over all bins having a value of Π_i less than the bin that contains $\vec{x}$ as shown in fo equation 7-8.

$$L(\Pi(\vec{x})) = \frac{\sum_{\Pi_i < \Pi(\vec{x})} weight}{\sum_{all} weight} \qquad \textbf{Eq. 7-7}$$

The three dimensional parameter space can be graphically represented by projections onto three separate two dimensional spaces. Contours of equal probability-density for these sub-spaces are shown in Figure 7-5, Figure 7-6 and Figure 7-7. The contours shown are for probability density values such that the fraction of evens that are more likely are 50%, 75%, 90% and 99%.

In order to minimize errors associated with finite bin size, the values of probability density for the signal events was calculated by interpolating between bins. The probability density for each bin was assigned to the position in parameter space corresponding to the center of that bin. The 27 bins closest to the measured values of the signal event were fit to a smooth hyper-surface using the MINUIT minimization package.[41] The fit function was evaluated at the measured values of $\Delta\Phi$, θ_{prim} and L_{d} and the probability density of the measured event was then taken the value of the fit function.

The uncertainty in the value of the probability density calculated with this method is a result of the uncertainties in the measured values of the parameters and the uncertainties of the value of the fit function. The fit uses the uncertainty of the probability density for each bin as inputs. These are assumed to be entirely statistical, depending on the number of events the bin :

$$\sigma(\Pi(i)) \propto \sigma(wgt_i) = \frac{wgt_i}{\sqrt{N_i}} \qquad \textbf{Eq. 7-8}$$

where N_i is the number of events in bin *i*.

The uncertainty in the fraction of events which are less likely, σ(L), is found numerically by calculating the sums $L(\Pi(\vec{x}) \pm \sigma(\Pi(\vec{x})))$. The contribution to this uncertainty from the of sum itself is negligible since it is proportional to $(N_{\Pi<\Pi(\vec{x})})^{-1/2}$ where $N_{\Pi<\Pi(\vec{x})}$ is the total number of events in all bins with a lower probability density: for all four candidate events this is less than 1%.

The results of this analysis for the four candidate events are summarized in It is seen that two of the events, 3333-17665 and 3039-01910, are completely consistent with being caused by a tau, 3024-30175 is more likely than ~5% of simulated taus and one event, 3263-25102, is more likely than only .025 % of simulated taus. Despite passing the selection cuts, it is unlikely that event 3263-25105 is a ν_τ charged-current interaction and is most likely a background event. This will be shown in the next section where relative probabilities are discussed .

Event	Probability density (rad $^{-2}$ mm^{-1})	Fraction of ν_τ events less likely
3024-30175	.345 ±.063	.049 ±.008
3039-01910	2.75±.13	.832 ± .013
3263-25105	.017±.005	$2.5\times10^{-3} \pm 9.0\times10^{-4}$
3333-17665	2.36±.105	.789 ± .014

Table 7-1 probability density and fraction of simulated events less likely for the four signal events

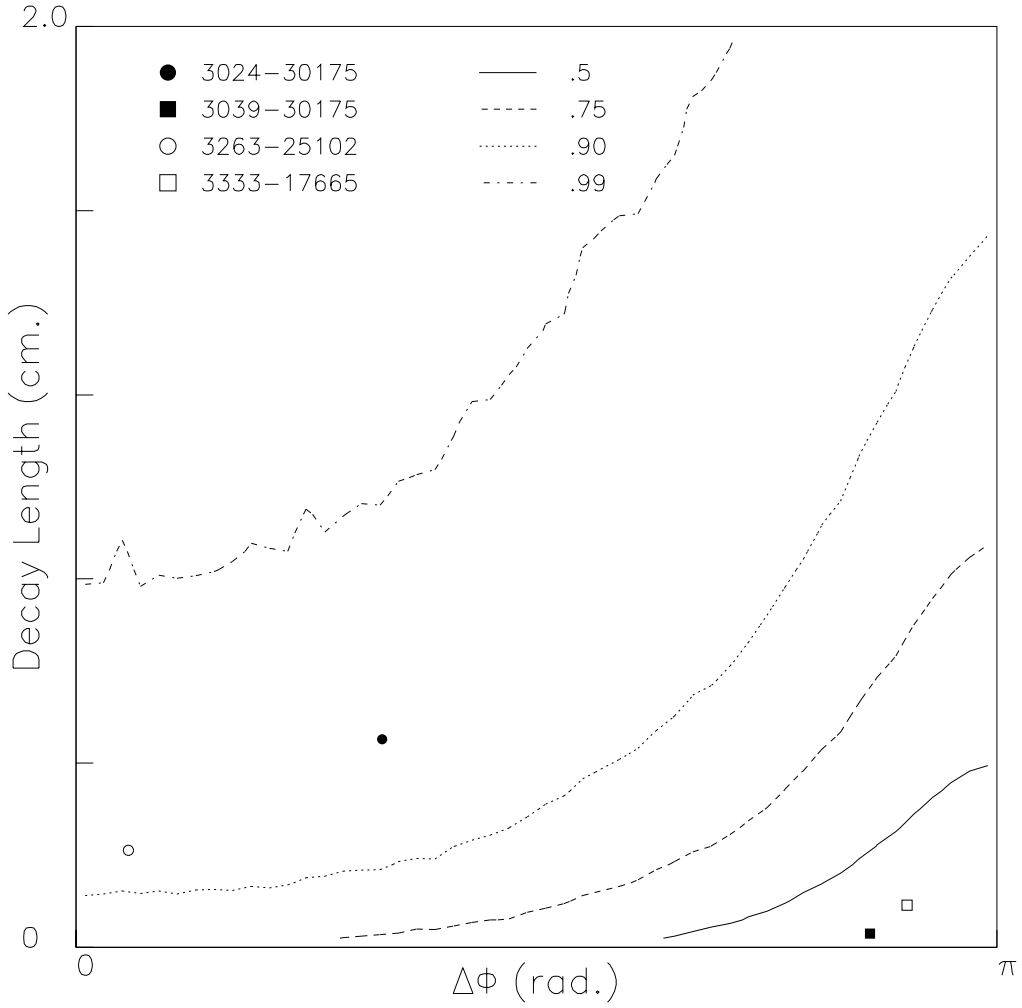

Figure 7-5 Contours of equal probability for a projection of the probability density onto the phi and decay length plane. The contours define areas that contains the stated fraction of events: i.e. the area inside the contour labeled .5 contains 50% of the events.

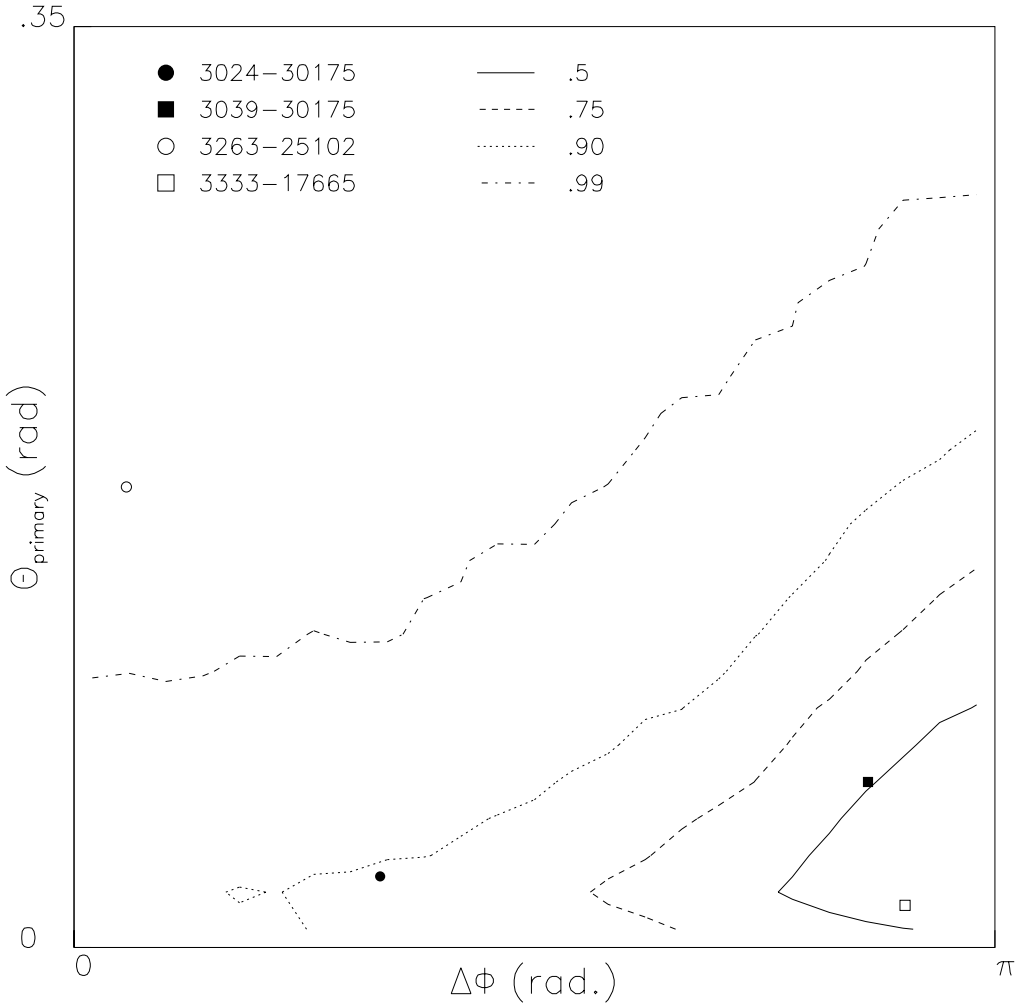

Figure 7-6 Contours of equal probability for a projection of the probability density onto the delta-phi and deprimary angle plane. The contours define areas that contains the stated fraction of events: i.e. the area inside the contour labeled .5 contains 50% of the events

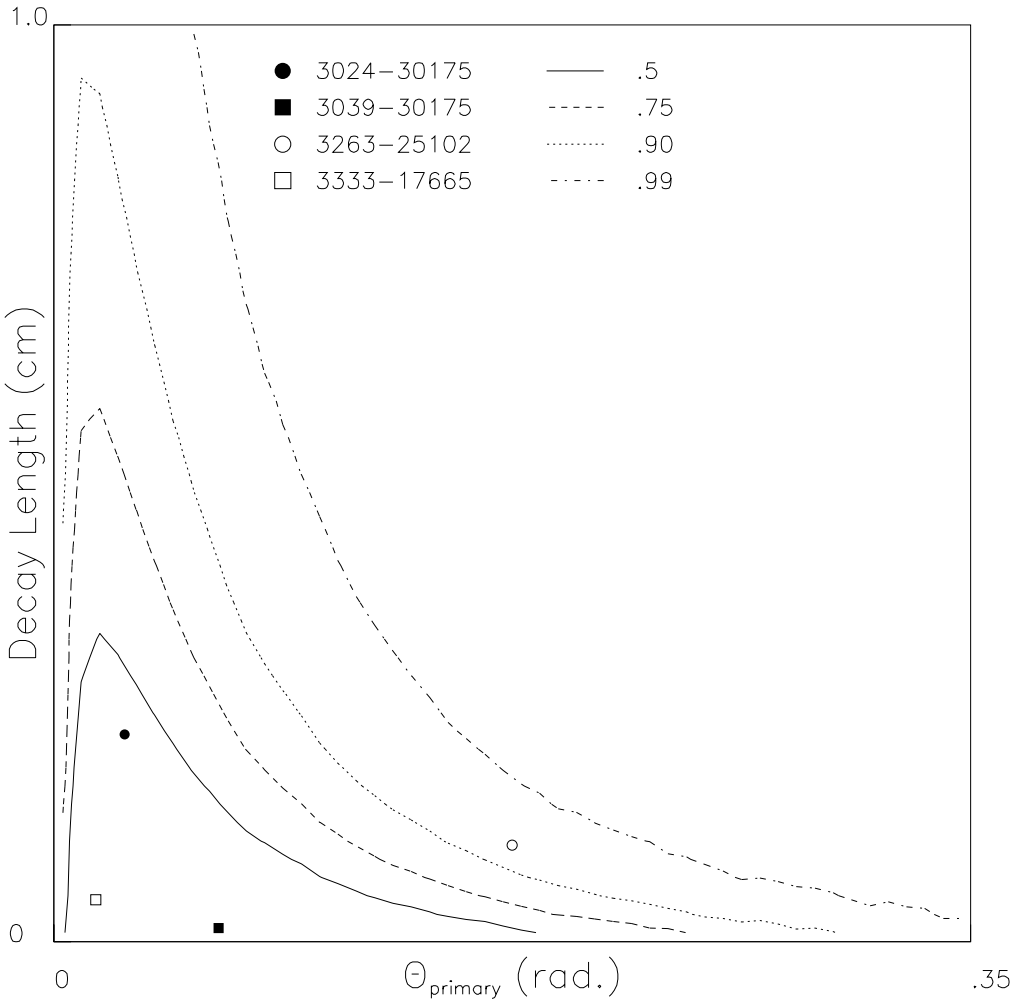

Figure 7-7 Contours of equal probability for a projection of the probability density onto the primary angle and decay length plane. The contours define areas that contains the stated fraction of events: i.e. the area inside the contour labeled .5 contains 50% of the events.

7.2 Relative probability of ν_τ or background source

The second step of the individual event analysis is to find the relative probability that each event is caused by a ν_τ interaction or a background source. As a signal event must be caused by either a tau decay or a background source, the relative probability that it is either can be found using Bayes theorem[42] as in equation 7-11:

$$P(tau \mid \vec{x}) = \frac{A_{tau}\Pi(\vec{x} \mid tau)}{A_{tau}\Pi(\vec{x} \mid tau) + \sum_{bkg} A_{bkg}\Pi(\vec{x} \mid bkg)} \qquad \textbf{Eq. 7-9}$$

As in the previous section, $\vec{x}$ here represents the characteristics of the event. A_i is the prior probability of hypothesis *i* and $\Pi(\vec{x} \mid hyp)$ is the probability density of each hypothesis evaluated at the measured value of $\vec{x}$. The prior probability is any *a priori* knowledge of the likelihood of the hypothesis. The hypotheses considered for this evaluation are tau decay and the dominant backgrounds which are charm decay and hadronic interaction. These account for 97% of all expected background events.

In this case a vector of five parameters is used to classify the event:

$$\vec{x} = (\Delta\Phi, \Theta_p, L_d, \Theta_{kink}, P_d)$$

The five parameters include the three used in the previous analysis, $\Delta\Phi$, Θ_{prim}, and L_d, as well as kink angle between the daughter track and the tau track, Θ_{kink}, and daughter momentum, P_d. These two parameters are included since they have significant discrimination between tau and background events. In principle a larger set of parameters could be used but these contain most of the information of the event. The parameters $\Delta\Phi$, Θ_{prim}, L_d are discussed for tau events in 7.1.1, Θ_{kink} and P_d are discussed below.

The probability density at $\vec{x}$ is calculated using simulated data for each hypothesis. It is determined from the fraction of simulated events which lay within a small region of parameter space surrounding the point $\vec{x}$.

The prior probabilities of each hypothesis are event specific and quantify any prior knowledge of this hypothesis. In general they are equal to the product of the expected flux of neutrinos, the expected interaction cross-section, the trigger, selection and location efficiencies, the probability of the process resulting in kinked track and the probability that the event passes the tau selection criteria. This is the same process as calculating the total number of expected background. However, the probability of some background process varies with the event's position within the detector and the type of daughter particle. These two factors are taken into account when calculating the prior probabilities A_i.

Phi imbalance: $\Delta\Phi$

The parameter $\Delta\Phi$ is a measure of the transverse momentum balance of the event and is described for ν_τ CC events in section 7.1.1. The particles that produce a kink in background events are not constrained to this momentum balance. For background events, $\Delta\Phi$ is the result of the random distribution of primary tracks and thus it's expected distribution broad and not peaked like the tau's. Figure 7-8 shows the $\Delta\Phi$ distributions for tau and background events.

Primary angle: Θ_{prim}

The opening angle of the primary track provides significant discrimination between the hadronic interaction background and tau events. The particles causing interaction background kinks are lower energy and in general have much larger opening angles than taus from ν_τ charged-current interactions. The distribution of opening angle for charm particles, however, is very similar to that of taus. Figure 7-9 shows the distribution of opening angle for simulated tau, primary charm particles and primary hadrons.

Decay length: L_d

For interaction background events the decay length is defined as the distance from the neutrino interaction vertex to the interaction position. This is the distance that

would be mistaken as the tau's particles path length. For charm background events, the decay length is that of the charm. The distribution of this distance for interactions in any given medium is essentially flat, except for a linear decrease after 1mm. This decrease is the result of the maximum impact parameter selection couples with the wide distribution of kink angles. For tau and charm decays the decay length follows decreasing exponentials convolved with the expected momentum distribution. They and are both strongly peaked at 0 length. Decay length distributions for simulated tau and charm events and the distributions of length in simulated interaction events are shown in Figure 7-10.

Daughter momentum: P_d

For all three hypotheses, the daughter momentum is the momentum of downstream portion the kinked track. This parameter provides significant distinction between tau events and interaction backgrounds which have significantly lower momentum. Distributions of daughter momentum for all types of events are shown in Figure 7-11.

The uncertainty in the measured value of the momentum comes from the limited number of segments used in multiple scattering analysis and the relatively modest amount of material between scatter measurements. Since the amount of scattering undergone by a particle decreases with momentum, the uncertainty in the measured value of momentum is larger for higher momentum particles.

Kink angle: Θ_d

As with daughter momentum, this parameter provides greatest distinction between tau events and interaction backgrounds. The kink angle for tau and charm decays are similar since the mass available for decay is similar. The decay angles for tau and charm events are generally smaller than the kinks producing interaction background events. The distribution of kink angle for all types of events is shown in Figure 7-12.

The uncertainty in the measured value of this parameter depends on how well both the upstream and downstream portion of the kinked track are reconstructed. Events

with multi-segment parent tracks therefore have much smaller uncertainties than do single segment parents. In all candidates the uncertainty is less than 2 mrad

The values of the parameters for all signal events are shown in Table 7-2

Event	3024-30175	3333-17665	3263-25102	3039-01910
Phi imbalance (rad)	$1.090 \pm .005$	$2.835 \pm .080$	$.104 \pm .0005$	$2.710 \pm .029$
Primary angle (mrad)	28 ± 2	91 ± 2	169 ± 2	67 ± 3
Decay length (μm)	4592 ± 10	550 ± 3	1947 ± 3	290 ± 8
Kink angle (mrad)	93 ± 0.6	90 ± 2.0	130 ± 0.5	13 ± 0.9
Daughter mom. (GeV/c)	$2.9^{+1.5}_{-0.8}$	$4.6^{+.1.4}_{-0.4}$	$1.9^{+2.2}_{-0.7}$	$21^{+.14}_{-0.6}$

Table 7-2 Parameters used in individual event analysis

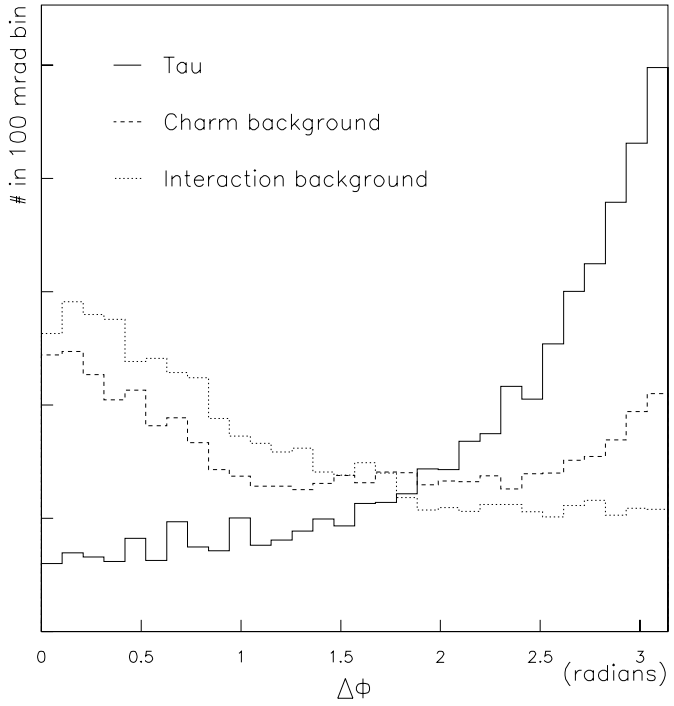

Figure 7-8 Phi imbalance distribution for simulated tau, charm and interaction events

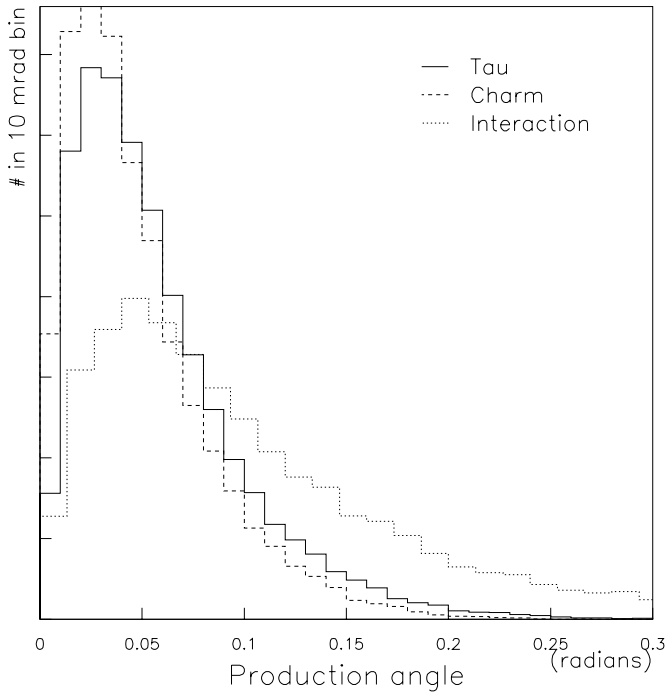

Figure 7-9 Production angle distributions for simulate tau, charm and interaction events.

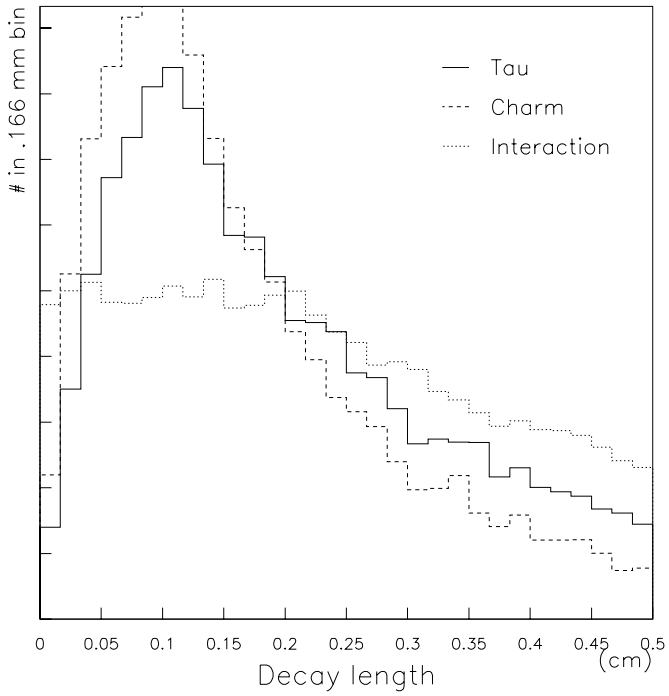

Figure 7-10 Decay length distributions for simulated tau, charm and interaction event

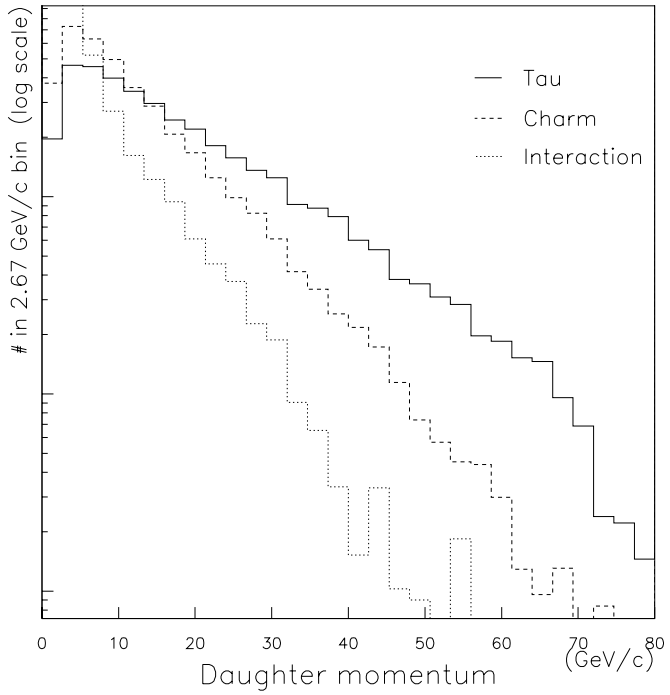

Figure 7-11 Daughter momentum distributions for simulated tau, charm and interaction events.

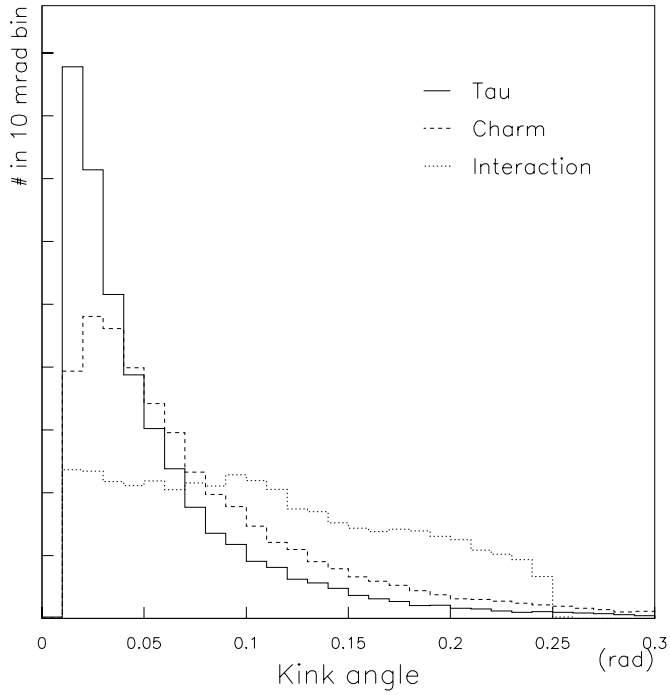

Figure 7-12 Kink angle distribution for simulated tau, charm and interaction events

7.2.1 Probability density

Unlike the previous analysis, the probability density here is not calculated over the entire parameter space but only in a region surrounding the measured values of each event. The probability density is calculated in two parts. This is because the relative uncertainty in the measured value of the daughter momentum is large compared to the uncertainty in the other parameters. A separate method must be used to calculate it's contribution to the total probability density. The probability density is factored in the following way:

$$\Pi(\vec{x}) = \Pi(\Theta_{prim}, \Delta\Phi, L_d, \Theta_{kink}) \times \Pi(P_d) \qquad \textbf{Eq. 7-10}$$

Here $\Pi(\Theta_{prim}, \Delta\Phi, L_d, \Theta_{kink})$ represents the probability density at the measured values of the event in a space of only four dimensions corresponding to the four parameters $\Delta\Phi$, Θ_p, L, and Θ_{kink}. This is equal to the fraction of simulated events which have parameter values within a small span of each of the four parameters. $\Pi(P_d)$ is the expected probability density at the measured value of P_d for events that are within this small four dimensional volume in $\Delta\Phi$, Θ_p, L, and Θ_{kink} space. Calculation of $\Pi(P_d)$ takes into account the relatively large uncertainty in the measured value of P_d and is described below.

For the parameters $\Delta\Phi$, Θ_p, L, and Θ_{kink} the span of each parameter making up the volume is chosen to include a minimum of two sigma uncertainty of the measured value. The interval is centered on the measured values of the parameters except when they are close to the upper or lower limits and this is not possible. A complete simulation of the process is carried out and the fraction of all Monte Carlo events with parameter values within the volume are recorded. The probability density is calculated by dividing this fraction by the size of volume which is equivalent to applying Eq. 7-7

$\Pi(P_d)$ is calculated by first approximating the probability density function, $\Pi(p)$, over the entire range of daughter momentum for the simulated the events that are within the small four dimensional volume. The average probability density for small intervals of momentum is found for the entire span of momentum for these events. This is done by

normalizing a histogram of the momentum to one and then dividing the contents of each bin by the width of the bin. This results is a plot of probability density versus momentum and is an approximation of $\Pi(p)$ at several discrete points.

The measured value of the daughter momentum is the most likely of a spread of possible true values, $\mathcal{P}$. The value of the probability density is calculated by convoluting the probability density function, $\Pi(p)$, with the measurement $\mathcal{P}$:

$$\Pi(P_d) = \int_0^\infty \Pi(p) \cdot \mathcal{P}\, dp \qquad \textbf{Eq. 7-11}$$

Since $\Pi(p)$ is approximated only at discrete points, the integral is replaced by a sum;

$$\Pi(P_d) = \sum_i \Pi(p = p_i) \cdot \mathcal{P}(p = p_i) \cdot \Delta p \qquad \textbf{Eq. 7-12}$$

Here the sum is over all values of momentum for which the probability density function has been approximated and Δp is (p_{i+1} - p_i). The spread in measured values is known to be the result of a Gaussian distribution of 1/p with $\sigma(1/p) = .3/P_d$.

As an example, Figure 7-13 shows $\Pi(p)$ for simulated tau decay events that have $\Delta\Phi$, Θ_p, L_d, and Θ_{kink} close to the measured values of event 3039-19110. The uncertainty of the measurement of the daughter momentum, $\mathcal{P}$, is also shown. The result of the sum in equation 7-12 , and , hence the value of the probability density is $\Pi(P_d) = .044$ $(Gev/c)^{-1}$. The span of the other parameters used in defining the four dimensional volume as well as their measured values are shown in Table 7-3. The total probability density as found with Equation 7-10 is $\Pi(\vec{x}) = 19.7\ (Gev/c)^{-1}(rad)^{-2}(mm)^{-2}$.

This method of calculating the probability density is used for all hypotheses appropriate for each events. These values, along with the prior probabilities, are then input to Equation 7-2 to calculate the relative likely hood of each hypothesis. The prior probability, the probability density calculation and the results of Equation 7-2 are discussed for each event below. The results are also summarized in Table 7-9

Parameter	Measured value	Span
$\Delta\Phi$	2.710 ± .030 rad	2.63 rad - 2.83 rad
Θ_{prim}	67 ± 3 mrad	57 mrad – 77 mrad
L_d	290 ± 8 μm	240 μm - 340 μm
Θ_{kink}	90 ± 2 mrad	80 mrad- 100 mrad

Table 7-3 Measured values and spread of parameters $\Delta\Phi$, Θ_p, L_d, and Θ_{kink} used to calculate the probability density for event 3039_01910.

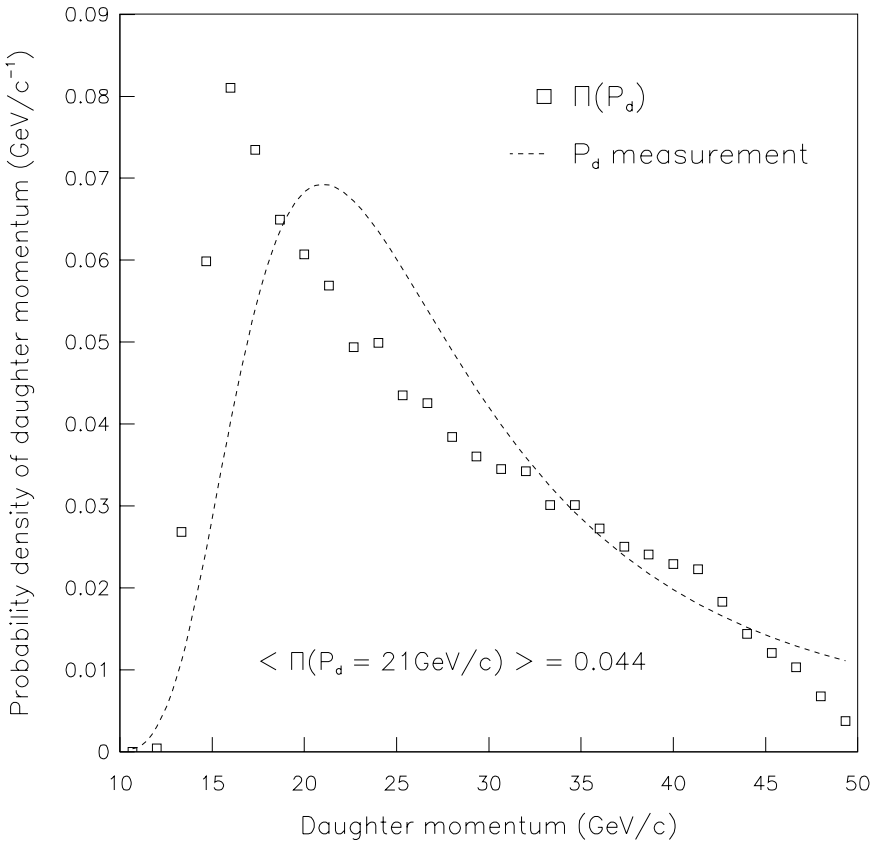

Figure 7-13 Π(p) and $\mathcal{P}$ (the spread in the measured value of P_d) for event 3333-19110.

7.3 Analysis of event 3024-30175

Event 3024-30175 is described in section 5.2.1. The daughter particle is identified as an electron and the 93 mrad kink occurs within a plastic base of an ECC800 emulsion sheet. The two hypotheses which would explain this event are either tau decay to electron or charm decay to an electron. The Baysean analysis described in section 7.2 is used to determine the relative probability of each of these hypotheses.

A third possible cause of the event is a ν_e charged-current interaction whose primary electron undergoes a large Columb scatter. This would explain the fact that none of the other primary tracks are identified as electrons, however the likelihood of a scatter of this magnitude is shown to be four orders of magnitude smaller than the other two hypotheses and will consequently be ignored. In section 6.4.4 the expected number of events with multiple scatters of sufficient magnitude to pass the tau selection criteria was found for all primary particles scattering only the steel plates. It was shown that the number of expected events is less than. 0.006. The number of primary electrons scattering within the plastic bases was not shown and will be briefly calculated here.

The total number of primary electrons undergoing Columbic scatters resulting in kinks that fulfill the tau selection criteria in either the 800 μm or 200 μm plastic bases is calculated with equation 7-13.

$$N_{scatter} = N_e \times N_{layer} \times S_{layer} \qquad \textbf{Eq. 7-13}$$

Here N_e is the number of ν_e charge-current interaction expected in the data set, N_{layer} is the number of either ECC800 or ECC200 plastic bases traversed by the primary electrons and S_{layer} is the probability of a primary electron scattering more than 10 mrad and having a transverse momentum greater than the0 .25 GeV/c selection limit.

A Monte Carlo simulation is used to calculate *S* by transporting primary electrons from simulated ν_e charged-current interactions through various layers of target material. Figure 7-14 shows the distribution of transverse momentum of 50 million simulated electrons that pass through either 200 and 800 μm. of plastic base. Only electrons that undergo a scatter of greater than 10mr and which have a momentum of

greater than 1.0 GeV/c are shown. The results of equation 7-13 are summarized in Table 7-4. The number of ν_e events in either the ECC200 or ECC800 target types is found using the expected number of ν_τ charged current interactions found in section 6.2.2 section multiplied by the fraction of all located events that are within that target type.

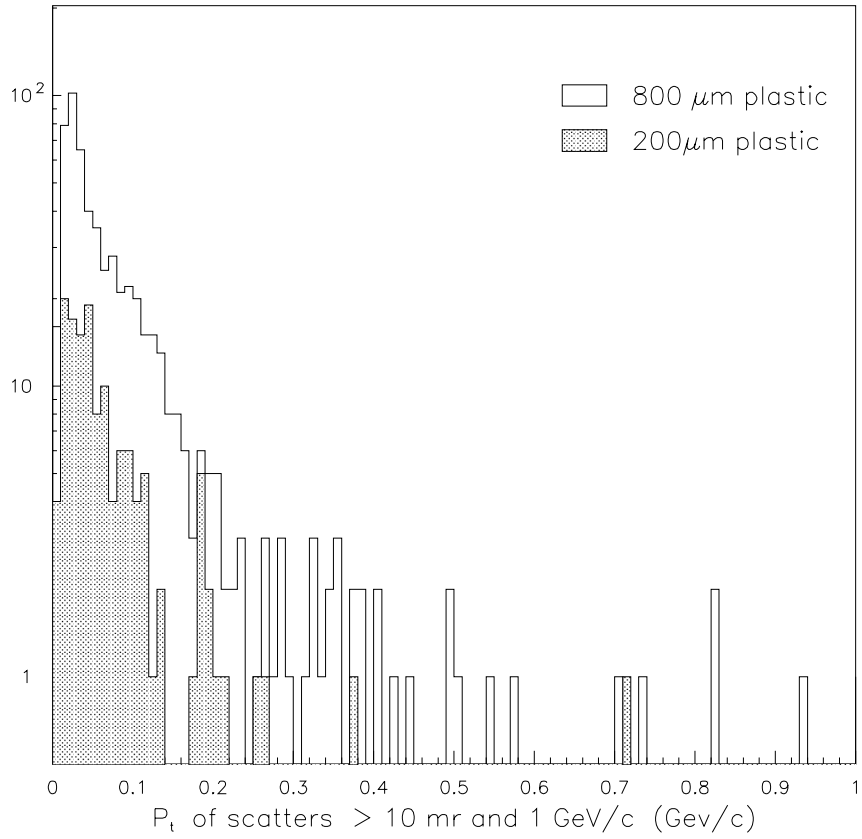

Figure 7-14 Transverse momentum distribution of scatters passing 10mr kink and 1GeV/c momentum cut. Distribution results from 50 M simulated scatters

Base type	N_e	⟨layers⟩	Expected number of scatters per layer	$N_{scatter}$
200 μm	17	4	8×10^{-8}	4.5×10^{-6}
800 μm	16	2.5	7.4×10^{-7}	2.9×10^{-5}

Table 7-4 Number of expected primary electron kinks passing tau selection criteria

The probability of a primary electron from a ν_e charged-current interaction causing a kink in the base of an ECC200 emulsion layer and passes the tau selection criteria is 4.5×10^{-6} as shown in Table 7-4. This hypothesis is 4 orders of magnitude less likely than other hypotheses and will not be considered as a possible cause for this event.

The reaming two hypothesis of tau decay and charm decay are discussed below.

The prior probability of any hypothesis is equal to the expected number of events of that hypothesis divided by the total number of expected signal events. Since the total number o expected signal events is common to the prior probabilities of all hypotheses and does not effect the result of Equation 7-3, the prior probability will be defined simply as the number of expected events for that hypothesis.

The prior probability that event 3024-30175 is a tau decay is equal to the number of expected τ to electron decay events that pass the tau selection criteria. This has already been calculated in 6.3 and is taken from Table 6-3 : $A_{\tau\rightarrow e} = N_{\tau\rightarrow e} = .854$.

The number of expected charm to electron events in the data set is taken from Table 6-6: $N_{charm\rightarrow e} = 0.034$. However, the calculation of this expectation uses the average probability that no primary muon or electron will be identified. For event 3024_30175 it is known that there are the equivalent of 0.57 radiation lengths of material downstream of the interaction vertex. This is slightly larger than the average of 0.97 radiation lengths which was used to calculate the number of charm events passing the tau selection criteria. In this event the probability of a primary electron being identified is higher than average and thus the probability of it being a background nuee ν_e events is lower than average. The prior probability of it being a charm decay background is lower than the number of charm decay events calculated in section 6.4.3. For an event with 0.57 radiation lengths of material downstream of the interaction vertex, the prior probability that it is from a charm decay to electron is $A_{charm \rightarrow e} = 0.044$.

The number of radiation lengths downstream does not effect the prior probability of the tau hypothesis since in tau events, there are no primary muons or electrons to be detected.

The relative probabilities that event 3024_3075 is due a ν_τ interaction and tau decay or charm decay is found with equation 7-11 and are .671 and .329 respectively. The inputs and results of eq 7-11 are summarized in Table 7-5

Hypothesis	Prior Probability	Probability density	Probability
Tau $\rightarrow$ electron	.854	.172	.671
Charm $\rightarrow$ electron	.044	2.07	.329

Table 7-5 Results of event probability analysis for event #3024_30175

7.4 Analysis of event 3333-17665

Event 3333-17665 is described in section 5.2.2 The daughter particle is identified as an electron and the kink occurs within a plastic base of an ECC800 emulsion sheet. As with event 3024-30175, the two hypotheses which would explain this event are tau decay to electron and charm decay to electron.

The prior probability that the event is a tau decay is equal to the number of expected tau to electron decays taken from Table 6-3 : $A_{\tau\rightarrow e} = N_{\tau\rightarrow e} = .854$. The prior probability that the event is a charm decay is found in the same manner as that for event 3024-30175. For this event there are 1.77 radiation lengths remaining in the modules downstream of the interaction vertex. This means the identification of a primary electron in ν_e charged-current interactions is more likely than average and thus the probability of it being a charm decay in a ν_e event with an undetected primary electron is lower than average. Thye expected number of charm to electron decays is listed in section 6.4.3 and is $N_{\tau\rightarrow e} = 0.034$. The prior probability of this event being a charm decay with no detected primary lepton is: $A_{\text{charm}\rightarrow e}$ 0.022

The relative probabilities that event 3333_17665 is due to a tau decay or charm decay is found with equation 7-11 and are .981 and .019 respectively. The inputs and results of eq 7-11 are summarized in Table 7-6.

Hypothesis	Prior Probability	Probability density	Probability
Tau $\rightarrow$ electron	.854	14.1	.981
Charm $\rightarrow$ electron	.028	2.42	.019

Table 7-6 Results of event probability analysis for event #3333_17665

7.5 Analysis of event 3039-01910

Event 3039_01910 is also described in section 5.2.2 It differs from events 3024-30175 and 3333-17665 in that the track downstream of the kink is identified as an hadron. Subsequently there are three hypotheses which would explain this event; ν_τ interaction and tau decay to a hadron, charm decay to a hadron and the secondary interaction of a primary hadron. In this event the kink occurs within the plastic base of an ECC200 emulsion sheet.

The prior probability that the event is a tau decay is proportional to the number of expected tau to hadron decays in the data set. This is taken from Table 6-3: $A_{\tau\rightarrow hadron} = N_{\tau\rightarrow hadron} = 2.1$

The number of expected charm to hadron decays is taken from Table 6-6 and is $N_{charm\rightarrow hadron} = 0.19$. In this event there are 0.96 radiation lengths remaining downstream in the module which approximately equal to the average of 0.97. Therefore the prior probability of this event being due to a charm decay to a hadron is equal to the calculated number charm to hadron decays : $A_{\,charm\,\rightarrow\,hadron} = N_{charm\,\rightarrow\,hadron} = 0.19$

The number of background events caused by hadron interactions occurring in the acrylic bases is taken from Table 6-6 , $N_{Aacrylic} = 0.015$. The prior probability of the event being caused by a hadron interaction in an event that has no detected primary electron or muon is thus : $A_{interaction\ (Acrylic)} = 0.015$

The inputs and results of equation 7-11 for event 3039-01910 are summarized in Table 7-7.

Hypotheses	Prior Probability	Probability Density	Probability
Tau $\rightarrow$ hadron	2.1	16.7	.977
Charm $\rightarrow$ hadron	.19	7.8	.023
interaction	.015	2.6	3.0×10^{-4}

Table 7-7 Results of probability analysis for event 3039_01910

7.6 Analysis of event 3263-25102

Event 3263-251-2 is also described in section 5.2.2. It has two distinguishing characteristics; first, the track downstream of the kink is identified as a hadron, and, second, the kink occurs within a steel plate of an ECC800 emulsion layer. There are three hypotheses which would explain this event. These hypotheses are; tau decay to hadron, charm decay to hadron, and the secondary interaction of a primary hadron.

The prior probability that the event is a tau decay is proportional to the number of expected tau to hadron decays and is taken from Table 6-3: $A_{\tau\rightarrow hadron} = N_{\tau\rightarrow hadron} = 2.1$

The number of expected charm to hadron decays is taken from Table 6-6 and equals 0.19. In this event there are 1.13 radiation lengths remaining downstream in the module compared to the average of 0.97. As with event 3039_01910, there is a greater than average probability of a primary electron being detected, and thus a smaller probability of the event being caused by a ν_e interaction that has a no detected primary electron. The prior probability of this event being due to a charm decay to a hadron is : $A_{\text{charm}\rightarrow\text{hadron}} = 0.17$

The number of background events caused by hadron interactions occurring in the steel plates is taken from Table 6-6 , $N_{steel} = 0.107$. The prior probability of this event being caused by an interaction is also effected by the lepton identification probability and is thus lower than the number of expected hadron interaction background events calculated in section 6.4.4. The prior probability of the event being caused by a hadron interaction in an event that has a no detected primary lepton is: $A_{\text{interaction (steel)}} = 0.101$

The inputs and results of equation 7-11 for event 3039-01910 are summarized in Table 7-7

Hypotheses	Prior Probability	Probability density	Probability of hypothesis
Tau $\rightarrow$ hadron	2.2	0.011	.144
Charm $\rightarrow$ hadron	.17	0.27	.267
Hadron interaction	.10	0.98	.589

Table 7-8 Results of probability analysis for event 3039_01910

This event is most likely an interaction background. The low evaluation of probability density for the tau hypothesis is due primarily to the parameters $\Delta\Phi$ and $\Theta_{prim.}$ It can be seen from Figure 7-6 that less than 1% of tau decays have $\Delta\Phi \leq 0.1$ while simultaneously having $\Theta_{prim} \geq 175$ mrad.

Table 7-9 summarizes the results of equation 7-10 and gives the relative probability of the three hypotheses for each observed signal event.

The results of the relative probability calculation confirm what was found in section 7.1; that three of the observed signal events are most likely caused by tau decay, and one event , 3263-25101 is most likely not.

7.7 Observation probability

Since the four observed signal events are independent, the probability that all four are background events is the product of the individual probabilities that each is caused by a background process. Using the probabilities listed in Table 7-9 the probability that all four are background is :

$$P(N_{background} = 4) = P(N_\tau = 0) = \prod_i (\sum_{bkg} P_{bkg}) = 1.2 \times 10^{-4} \qquad \textbf{Eq. 7-14}$$

This probability can be compared with the result 4.04×10^{-4} found in section 6.5 using only the total expected number of tau and background events. The difference in the two values that are calculated reflects the fact that the individual event analysis takes into account more information than whether or not the event has passed the tau selection criteria. Specifically, the material in which the kink occurs and the lepton identification efficiency effect the likelihood that the event is a background or not.

Hypothesis	3024_30175	3333_17665	3039_01910	3263_25102
Charm → μ	0	0	0	0
Charm → e	.329	.019	0	0
Charm → hadron	0	0	.023	.267
Hadron interaction	0	0	3.0×10^{-4}	.589
$\tau \rightarrow \mu$	0	0	0	0
$\tau \rightarrow$ e	.671	.981	0	0
$\tau \rightarrow$hadron	0	0	.977	.144

Table 7-9 Summary of individual event probabilities

The probability that at least one ν_τ charged-current interaction is in the set of observed signal events is found with Equation 7-20:

$$P(N_\tau \geq 1) = 1 - P(N_{background} = 4) = 1 - 1.2\times10^{-4} = .99986 \qquad \textbf{Eq. 7-15}$$

From this small probability it follows conclusively that FNAL experiment E872 has observed the first charged-current interactions of the tau neutrino.

8 Conclusion

For the first time the charged-current interactions of the tau neutrino have been observed. Four events selected from a set of neutrino interactions in an emulsion target have track topologies consistent with the decay of tau lepton that has been produced in ν_τ charged-current interactions. The number of ν_τ interactions found is in agreement with standard model predictions.

In this analysis the expected number of ν_τ interactions was found in two ways, both of which gave consistent results. The first method used an *a priori* calculation of the interaction rates for all neutrinos in the beam. These rates were then corrected for the different detection and location efficiencies for each type of neutrino interaction. The resulting fraction of all located events due to ν_τ was predicted to be 0.035 ± 0.012, giving an expectation of 6.9 ± 2.3 events in the data set of 203 neutrino interactions. In the second method, the number of ν_τ interactions was calculated using the observed number of ν_μ and ν_e interactions that were caused by neutrinos from charm meson decays and the expected ratio of interaction rates R_τ / R_e and R_τ / R_μ. There are 59 ± 6 ν_e and 58 ± 7

ν_μ interactions respectively and the interaction rate ratio was calculated to be $0.163^{+.030}_{-.027}$ for ν_μ and $0.139^{+.030}_{-.027}$ for ν_e. When calculated using this method, the average number of expected ν_τ interactions was $8.6 \pm 1.9 \pm 0.9$ (sys.)

The ν_τ signal was defined by criteria based on the single charge decay of the tau, which are produced in ν_τ interactions. Theses criteria accept .52 of all ν_τ events, giving an expected signal of 3.9 ± 0.95 events. Backgrounds included in the signal were caused by charm decay, secondary interactions, and random association of tracks in ν_μ and ν_e interactions. The expected number of background events due to all of these sources was calculated to be 0.44 ± 0.04 giving a total expected signal of 4.3 ± 1.0 events.

In addition, each of the four signal events was analyzed to find the probability that it was due to a ν_τ or a background source. A Baysean analysis using five parameters describing the event and a probability density found through Monte Carlo simulation was used to calculate the relative probability that each signal event was caused by a ν_τ or either of the two dominant background sources of charm decay or secondary interaction.

Results of this analysis showed that there are three events which are most likely caused by ν_τ interactions. These events have relative probability of being ν_τ interactions equal to .977, .981, and .671 while having probability of being due to background processes equal to .023, .019, and .329 respectively. The Baysean analysis also shows that one signal event is most likely not a tau, having relative probability of being caused by a ν_τ interaction equal to .144 versus .856 for being a background. The results of the analyses done on the four signal events combine to give a probability of .99986 that at least one of them is a ν_τ interaction.

Appendix A. Expected rate of neutrino interactions.

Assuming the ν_τ behaves as standard model particle, the expected number of tau-neutrino interactions in the emulsion target can be calculated. The number of expected ν_τ interaction in the target is used along with selection and identification efficiency to check the number actually observed. The expected rate of ν_μ and ν_e interactions is used to predict the number of background events.

A.1 Expected rate of ν_τ interactions

The rate of ν_τ charged-current interactions in the emulsion target is given by:

$$R = \phi \cdot \sigma \cdot N \qquad \textbf{Eq. A 1}$$

Here ϕ is the flux of ν_τ through the emulsion target, σ is the average cross-section of a ν_τ charged-current interaction and *N* is equal to the number of nucleons in the target. The number of nucleons can be expressed as $N = N_A \times \text{mass}_{\text{target}}$ (grams) with N_A = Avagadro's number = 6.02×10^{23}.

Since the source of ν_τs in the neutrino beam is the decay of the D_s, the flux at the target is calculated from the production and decay of the D_s:

$$\phi = N_{proton} \cdot \frac{N_{\nu_\tau}}{proton} \cdot \frac{\eta}{Area} \qquad \textbf{Eq. A 2}$$

$$= N_{proton} \frac{\sigma(pW \rightarrow D_s)}{\sigma(pW)_{Tottal}} \cdot BR(D_s \rightarrow \nu_\tau + \tau) \cdot 2 \cdot \frac{\eta}{Area}$$

In these expressions $\sigma(pW \rightarrow D_s)$ is the D_s production cross-section in 800GeV/c proton-Tungsten interactions, $\sigma(\text{pW})_{\text{total}}$ is the total proton-Tungsten interaction cross-section, *BR* is the branching fraction to ν_τ, η is the acceptance fraction of the emulsion target and the factor of 2 takes into accounts for the fact that every charged tau produced in a D_s decay subsequently decays creating an $\overline{\nu}_\tau$ as well.

The cross-section and acceptance vary with neutrino energy and must be calculated using the energy spectrum of produced ν_τs. The complete expression of the ν_τ interaction rate per kg of target material per proton incident on the Tungsten dump is given by Equation A-3.

$$R(kg^{-1} proton^{-1}) = \frac{\sigma(pW \rightarrow D_s)}{\sigma(pW)_{Tottal}} \cdot BR(D_s \rightarrow \nu_\tau + \tau) \cdot 2 \cdot \int \eta(E) \cdot \sigma(E) \cdot \frac{dN}{dE} \cdot dE \qquad \textbf{Eq. A 3}$$

In this expression *dN/dE* is the energy distribution of produced ν_τ and the integral is over the energy spectrum of all ν_τs produced. Each term in this expression is discussed below.

Proton tungsten cross-section: σ(pW) total

The total cross-section for proton–Tungsten interactions is calculated by scaling the cross-section of proton-proton interactions. The nuclear dependence of proton-nucleus cross-section is parameterized as $\sigma = \sigma_0 \cdot A^{\alpha\bullet}$[43] where $\alpha\bullet$=0.71 ± 0.03.[44] This is approximately the power law expected (α = 2/3) by nucleon surface exposure. The proton-nucleon total cross-section for 800 GeV/c protons is measured to be 37.6 mb [27] and hence the proton-tungsten cross-section is calculated to be 1.52 ± 0.26 barns.

D_s production cross-section : $\sigma(pW \to D_s)$

Since there has been no direct measurement of the D_s production cross-section in 800GeV proton interactions and it must me inferred from the cross-section of either D^+ or D^0 production cross-section and the ratio of $\sigma_{D_s}/\sigma_{D^+}$ or $\sigma_{D_s}/\sigma_{D^0}$ as in Equation 8-4;

$$\sigma(pW \to D_s) = \left\langle \frac{\sigma_{D_s}}{\sigma_D} \right\rangle \cdot \sigma_{D800\,GeV} \cdot A^{\alpha} \qquad \textbf{Eq. A 4}$$

Here the $\sigma_{D800\ GeV}$ is the cross-section per nucleon and A^{α} is the nuclear dependence of D production in 800 GeV proton interactions. The ratios of $\sigma_{D_s}/\sigma_{D^+}$ and $\sigma_{D_s}/\sigma_{D^0}$ has been measured in several experiments and both are consistent over a wide range of energies. Table A-1 lists the ratios measured.

Three experiments have measured the D^0 and D^+ production cross-section with 800 GeV/c protons. The results are listed in table A-2. Using the mean cross-section values from Table A-2 , the cross-section ratios from Table A-1 and equation 8-4 gives the D_s cross-section of 3.5 ± 0.6 μb from the D^0 data and 9.4 ± 2.5 μb from the D^+ data. Since the measurement from E789 dominate the mean only its result will be used. E789's measurement of D^0 cross-section gives a D_s production cross-section of 3.5 ± 0.7 μbarns/nucleon. This value will be used for all subsequent calculation in this thesis. Four of the experiments listed in Table A- have used different target material to measure the

nuclear dependence for D production. Their results are listed in table A-3. All of these measurements are consistent with a linear dependence on atomic number.

Experiment	E (GeV)	Beam	D_s/D^+	D_s/D^0	D^+/D^0
CLEO [45]	10	$e^+ e^-$	.77±.35	.32±.14	.38±.10
NA32 [46]	250	Pion	.47±.20	.24±.10	.51±.15
WA92 [47]	350	Pion	.39±.12	.16±.05	.42±.05
E653 [48]	600	Pion	-	-	.4±.1
E653 [49]	800	Proton	-	-	.8±.4
E691 [50]	100-275	Gamma	.27±.09	.14±.04	.51±.11
E769 [51]	250	$Pion^+$	.62±.15	.28±.07	.44±.06
E769 [51]	250	Proton	.47±.31	.27±.18	.42±.05
E769 [51]	210	$Pion^-$	-	-	.27±.06
E791	250	Proton	-	-	.57±.22
Mean			.40±.06	.18±.03	.41±.02

Table A-1 Measured values of the production cross-section ratio for charm mesons

Experiment	$\sigma(D^0)$ (μb/nucleon) [# events]	$\sigma(D^+)$ (μb /nucleon) [# events]
E653 [48]	38±13 [128]	31±14 [18]
E743 [52]	13±6 [10]	21±6 [46]
E789 [53]	18.5±3.5 [>4000]	-
Mean	18.2± 2.9	23±6

Table A-2 Cross-section of D^0 and D^+ production in 800GeV/c proton-nucleon interactions

Experiment	Target material	α
WA82 [54]	Si, W	.92 ± .06
WA92 [55]	Cu, W	.95 ± .07
E769 [56]	Be, Cu, Al, W	1.00± .06
E789 [57]	Be, Au	1.02 ± .04
Mean		.99 ± .03

Table A-3 Values of parameter α for the nuclear dependence of D production cross-section of the form A^{α}

Branching fraction of D_s to ν_τ: $BR(D_s \to \nu_\tau + \tau)$

The branching ratio of $D_s \longrightarrow \tau + \nu_\tau$ has not been measured with high precision. The L3 experiment reports 0.074 ± 0.04 with 16 events [58]. An improvement on this measurement can be obtained by using lepton universality and the more thorough measurements of $D_s \longrightarrow \mu + \nu_\mu$.

The decay width for $D_s \longrightarrow l + \nu_l$ (where l represents either an electron or muon) is given by [27]

$$\Gamma(D_s \to l + \nu_l) = \alpha \cdot f_{D_s}^2 \cdot m_l^2 \cdot \left(1 - \frac{m_l^2}{m_{D_s}^2}\right)^2 \qquad \textbf{Eq. A 5}$$

Here f_{D_s} is the psuedo-scaler decay constant and α is the proportionality constant:

$$\alpha = \frac{G_F^2}{8\pi} m_{D_s} |V_{CS}|^2 = 9.96 \pm 0.23 \times 10^{-21}\ \text{MeV}^{-3} \qquad \textbf{Eq. A 6}$$

The uncertainty in the decay width is dominated by the value of the CKM matrix element $|V_{cs}|$. The value used is from reference 59 , $|V_{cs}| = .9891 \pm .016$. The psuedo-scaler decay constant has been measured in several experiments using both muon and tau decay channels. Table A- lists results of these measurements.

The total decay width of the D_s is $\Gamma_{tot} = (1.33 \pm 0.03) \times 10^{-9}$ Me V. The branching fraction for $D_s \longrightarrow \tau + \nu_\tau$ is equal to $\Gamma(D_s \longrightarrow \tau + \nu_\tau) / \Gamma_{tot}$. Using the average value of

f_{D_s} = 285±25, the published values [27] for G_F, $|V_{cs}|$, m_τ and m_{Ds} in equation 8-5 give a branching fraction $D_s \longrightarrow \tau + \nu_\tau$ = 6.6 ± 0.8 %.

Experiment	Decay Mode	f_{D_s} (MeV)
CLEO [60]	$D_s \longrightarrow \mu + \nu_\mu$	280±45
WA 75 [61]	$D_s \longrightarrow \mu + \nu_\mu$	238±70
BES [62]	$D_s \longrightarrow \mu + \nu_\mu$ $D_s \longrightarrow \tau + \nu_\tau$	430±160
E653 [63]	$D_s \longrightarrow \mu + \nu_\mu$	280±40
L3 [58]	$D_s \longrightarrow \tau + \nu_\tau$	309±80
DELPHI [64]	$D_s \longrightarrow \tau + \nu_\tau$	330±45
Mean		285±25

Table A-4 Measured values of the psuodo-scaler decay constant f_{Ds}

Target acceptance and neutrino spectrum: $\eta(E)$ and dN/dE

The target acceptance and the energy spectrum of ν_τ at the target depend on the angular distribution of the ν_τ in the decay of the D_s and the tau, and hence on the angular distribution of the D_s created n the dump. The differential cross-section of the D_s meson follows the empirical parameterization [65] ;

$$\frac{d\sigma}{dx_f\, dp_t^2} \propto (1 - x_F)^n \exp(-bp_T^2) \qquad \textbf{Eq. A 7}$$

Here x_F is the longitudinal momentum fraction which is calculated in the center of momentum frame as

$$x_F = \frac{2p_z}{\sqrt{s}} \qquad \textbf{Eq. A 8}$$

$$p_T = \sqrt{P_x^2 + P_y^2} \qquad \textbf{Eq. A 9}$$

Experiment	b (GeV^{-2})	n
E653 [49]	0.84 ± 0.09	6.9 ± 1.9
E743 [66]	0.80 ± 0.2	8.6± 2.0
Mean	0.83 ± 0.11	7.7 ± 1.4

Table A-5 Phase space parameterization of D production

The parameters *n* and *b* are energy dependant and determined experimentally. Table A shows the measured values of these parameters for D_s produced in 800 GeV/c proton –nucleon interactions. Since the two shown measurements are consistent with each other the weighted averages: $b = 0.83 \pm 0.11$ and $n = 7.7 \pm 1.4$ are used.

The neutrino flux at the emulsion target as well as the target acceptance is found using Monte Carlo simulation. D_s produced in proton-nucleon interactions are simulated with a transverse and longitudinal distribution given by equation A-7. The interaction position is assumed to be at the at the center of the tungsten beam dump in the transverse plane and at a position L from the front of the dump. L is taken from a distribution proportional to $e^{-L/\lambda}$, where $\lambda = 9.65$ cm. is the nuclear interaction length in Tungsten[27]. Both of the parameters *n* and *b* are varied using a Gaussian distribution with a width equal to the measured uncertainty. The D_s are projected to a decay position calculated from a randomly chosen lifetime and there the decay of the D_s to a τ and ν_τ is done isotropically. The τ decay is carried out in a similar manner; it is projected to a decay position and decayed.

Both the neutrinos resulting from the D_s decay and from the tau decay are then projected to the z position of the emulsion target 36m downstream. The target acceptance is the fraction of theses which lie with the 50cm x 50cm transverse dimensions of the target. shows the energy spectrum of both neutrino and anti-neutrinos at the target.

When using the central values of $b = 0.83$ and $n = 7.7$, the average target acceptance is found to be $\langle\eta\rangle = 7.4\%$

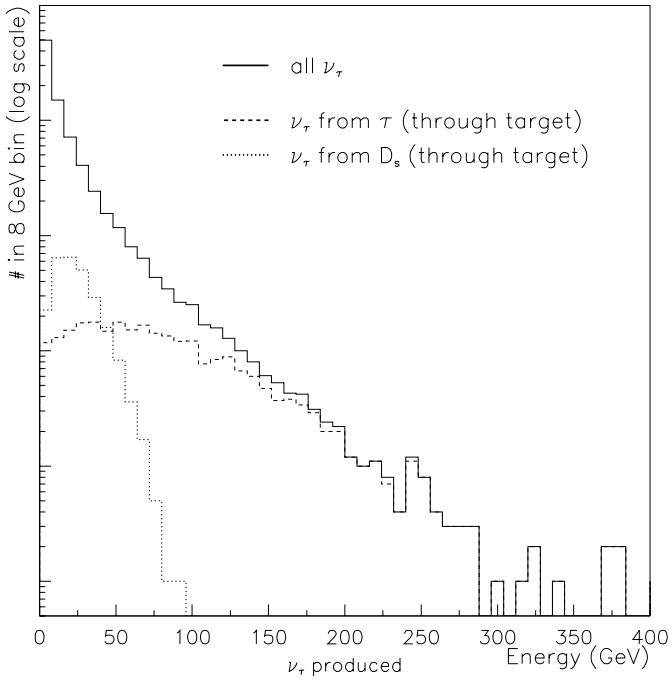

Figure A-8-1 Spectrum of ν_τ produced and those interacting in the target

ν_τ interaction cross-section : $\sigma_{\nu_\tau cc}(E)$

The charged-current cross-section of ν_τ + Nucleon interactions is predicted by the standard model to be the same as ν_μ and ν_e interactions. However, ν_τ interaction must take into account a significant kinematic factor since charged-current interactions of ν_τ result in τ, which is much more massive than the nucleon. This is not true for ν_e and ν_μ charged-current interactions since the resulting charge lepton is light ($m_l << m_N$) and the kinematic factor is essentially one.

The cross-section for ν_τ is thus given by:

$$\sigma_{\nu_\tau cc}(E) = K(E) \cdot \sigma_0 \cdot \mathrm{E}_\nu \qquad \textbf{Eq. A 10}$$

Here *K(E)* is the kinematic factor described above, and σ_0 is $d\sigma/dE$ which is assumed to be the same for all charged-current neutrino interactions. The differential cross-section has been measured extensively for for ν_e and ν_μ and is well known over a wide range of energies. The average value of σ_0 for neutrinos is $6.77 \pm .014 \times 10^{-43}$ m^2/GeV and $3.34 \pm 0 .08 \times 10^{-43}$ m^2/GeV for anti-neutrinos. Assuming an equal number of neutrinos and anti-neutrinos in the dump gives an average of $\langle\sigma_0\rangle = 5.05 \pm 0.09 \times 10^{-43}$ m^2/GeV .

The kinematic factor *K(E)* is calculated using the differential cross-section of Albright and Jarlskog[23]. The production of the massive tau lepton results in a threshold at ~5.1 GeV below which the cross-section is zero and the factor approach 1 at high energies. Figure 8-2 shows the kinematic factor for both neutrino and antineutrinos.

The probability of interaction is proportional to the cross-section and hence the spectrum of ν_τ undergoing interaction is found by multiplying the energy spectrum of the produced neutrinos and the energy dependant expression for the cross-section.. Figure A-8-3 shows the expected spectrum of ν_τ undergoing interaction in the emulsion target. The lower peak in the distribution is due to ν_τs from the D_s decay and the higher peak is due to ν_τs from the tau decay. The average energy of an interacted ν_τ is 115 GeV. For an equal number of neutrinos and antineutrinos , the average charged-current cross-section is $\left\langle \sigma_{\nu_\tau cc}(E) \right\rangle = 4.33 \times 10^{-41}$ m^2.

The total number of ν_τ charged-current interaction per proton on target per kg of is target is calculated with Equation 8-2 using the flux found in the previous section and the cross-section calculated with by Equation. 8-9.

The result is $3.71^{+1.3}_{-1.2} \times 10^{-19}$ $pot^{-1}kg^{-1}$.

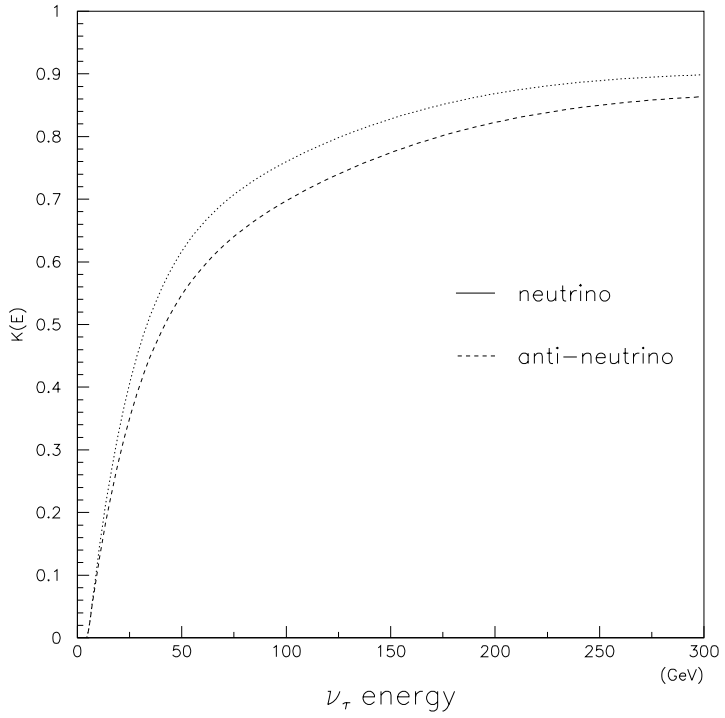

Figure A-8-2 Kinematic factor in heavy neutrino production

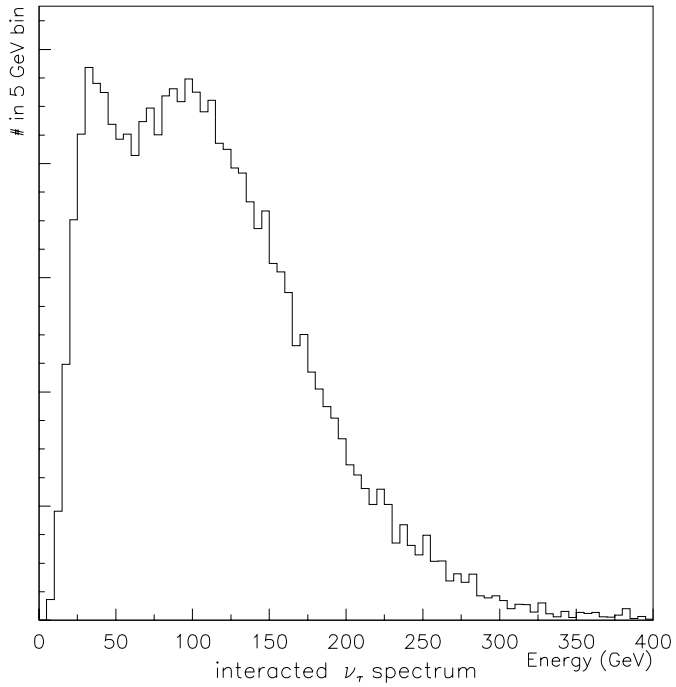

Figure A-8-3 Spectrum of interacting ν_τ

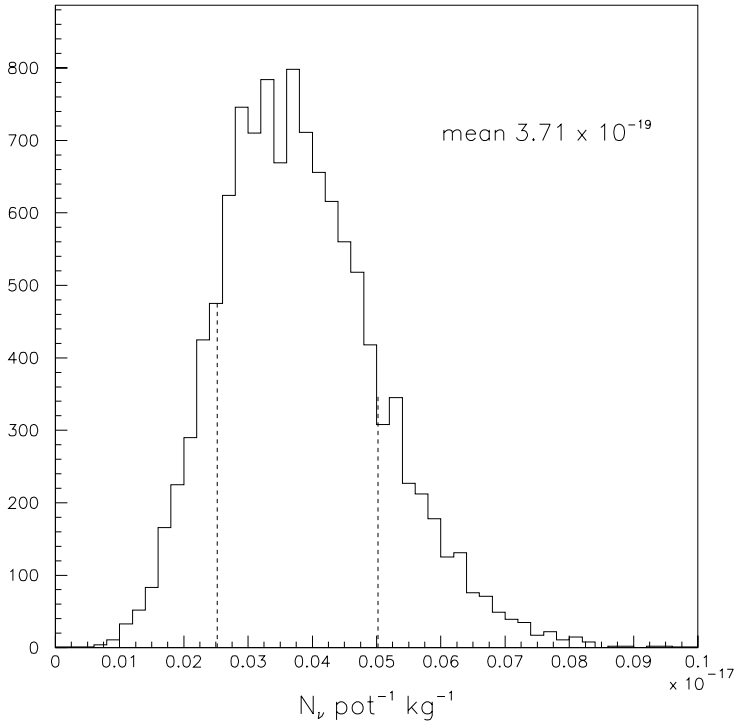

Figure A-8-4 ν_τ interaction rate for ten thousand simulations, each using one hundred thousand generated ν_τs

Parameter	Value	Contribution to rate uncertainty ($pot^{-1}kg^{-1}$)
$\alpha_{p\text{-}W}$	0.71 ± 0.03	0.59×10^{-19}
$\alpha_{D\ production}$	0.99 ± 0.03	0.59×10^{-19}
$\sigma(D^0)$	18.5 ± 3.5	0.41×10^{-19}
$\sigma(D_s)/\sigma(D^0)$	$0.18 \pm .3$	0.33×10^{-19}
$BR(D_s \rightarrow \tau)$	$0.066 \pm .008$	0.07×10^{-19}
b	$0.83 \pm .11$	0.18×10^{-19}
n	7.7 ± 1.4	0.44×10^{-19}
Monte Carlo statistics	-	0.15×10^{-19}

Table A-6 Contributions to uncertainty in ν_τ interaction rate

A Monte Carlo simulation is used to calculate the integral in the expression for the interaction rate. A series of ten thousand simulation are performed, each consisting of ~ 100K generated ν_τ. All inputs, including production cross-section, branching ratios and phase space production parameterizations are varied within their uncertainties. For each set of generated ν_τ, the number and average energy of those intersecting the emulsion target are recorded. Figure A-8-4 shows the distribution of the rates for the simulated experiments. The spread in the distribution of the calculated interaction rate results mainly from the charm meson production cross-section and phase space distribution of D_s production. Individual contributions to the total rate for each input parameter is calculated by fixing all other parameters at their central value and allowing only the parameter of interest to be varied in the simulation. The sources of the uncertainties and their contribution to the uncertainty are listed in Table A-.

A.2 Expected rate of ν_μ and ν_e interactions

The majority of neutrino interactions occurring in the target are ν_e and ν_μ. It is important to understand the flux of these neutrinos since the background to the tau signal is proportional to the number off these interactions. The primary source of high energy ν_μ andν_e are the decay of charm particles produced in the dump. $D^{+/-}$, D^0 and D_s and Λ_c all have significant leptonic and semi-leptonic decay modes. These sources are labeled 'prompt' since they result directly from charm decay. The neutrinos produced in these decays are of comparable energy to the ν_τs produced in the D_s decay. Decay of he lighter mesons resulting from the proton–tungsten interaction also contribute to the ν_μ flux. The π and K are not massive enough to produce a tau and the decay through electron mode is highly suppressed due to its small mass, thus these decays only contribute to the ν_μ component of the neutrino beam. The interaction rate of the ν_e and ν_μ from both charm and light meson sources are calculated below.

Prompt neutrino interaction rate.

The rate of prompt ν_e and ν_μ interactions can be calculated in a manner similar to that of the ν_τ. The number of interactions per proton per kg is given by Equation 8-10 with the index τ replaced by μ or e. Calculation of the flux must take into account the several species of charm which decay into neutrinos:

$$R_{\nu_\kappa} kg^{-1} proton^{-1} = \sum_i \frac{\sigma(pW \to C_i)}{\sigma(pW)_{Tottal}} \cdot BR(C_i \to \nu_l) \cdot \int \eta_l(E) \cdot \sigma_l(E) \cdot \frac{dN_l}{dE} \cdot dE_l$$

Eq. A 11

In this expression the index *l* represents either muon or electron and the sum is over all species of charm particles that are produced, ($C_{i,}$ = D^0, D^+ or D_s)*, η is the target acceptance function , σ_l is the interaction cross-section and dN/dE is the energy spectrum

Charm production and decay

The cross-section for D^0 and D_s are 18.2± 2.9 and 3.5 ± 0.6 μbarn/nucleon respectively as found in section 0. The D^+ production cross-section can be inferred from the D^0 cross-section and the ratios listed in Table A-. The result is 8.4± 1.3 μbarn/nucleon. The semi-leptonic branching ratios for the charmed mesons are taken from reference 27 and are listed in Table A-.

The charm meson production follows the same x_f and p_t parameterization as shown in section 0. The total flux and spectrum of each type of neutrino is found using a Monte Carlo simulation of production, decay and propagation to the emulsion target as was done for the ν_τ. The target acceptance, flux and interaction rate which are the result of this simulation are shown in Table A- .

*The charm baryon Λ_c also is produced , however it is not included in this sum because its production cross-section is small relative to the meson's and its semi-leptonic branching ratios of 4.5 % is smaller than the D^0, D^+ or D_s which are 7.2%, 17.5% and ~8% respectively. Both of these factors significantly reduce its contribution to the neutrino flux: at the target is calculated to be < 3% of that due to the charmed mesons.

	$\sigma(D_i)/\sigma_{tot}$	BR %	$\langle\eta\rangle$	$\langle\phi\rangle$ (m^{-2} $proton^{-1}$)
$D^+ \longrightarrow \nu_e$	2.19×10^{-5}	17.2 ± 1.9	.068	4.8×10^{-5}
$D^0 \longrightarrow \nu_e$	1.01×10^{-5}	$6.75 \pm .29$	.069	4.1×10^{-5}
$D_s \longrightarrow \nu_e$	4.20×10^{-6}	8 ± 5	.065	8.8×10^{-6}
$D^+ \longrightarrow \nu_\mu$	2.19×10^{-5}	16 ± 3	.063	4.3×10^{-5}
$D^0 \longrightarrow \nu_\mu$	1.01×10^{-5}	$6.6 \pm .8$	.064	3.8×10^{-5}
$D_s \longrightarrow \nu_\mu$	4.20×10^{-6}	8 ± 5	.064	8.6×10^{-6}

Table A-7 Flux at target and average target acceptance of prompt ν_μ and ν_e

	$\langle$Energy$\rangle$ (GeV)	$\langle\sigma\rangle$ (m^2)	Rate (kg^{-1} $proton^{-1}$)
$D^0 \longrightarrow \nu_e$	93.3	4.71×10^{-41}	1.19×10^{-18}
$D^+ \longrightarrow \nu_e$	77.3	3.90×10^{-41}	1.02×10^{-18}
$D_s \longrightarrow \nu_e$	77.5	3.91×10^{-41}	4.50×10^{-19}
ν_e total			$2.66^{+.58}_{-.55} \times 10^{-18}$
$D^0 \longrightarrow \nu_\mu$	100.5	5.07×10^{-41}	1.01×10^{-18}
$D^+ \longrightarrow \nu_\mu$	83.3	4.20×10^{-41}	$.81 \times 10^{-18}$
$D_s \longrightarrow \nu_\mu$	75.3	3.80×10^{-41}	4.51×10^{-19}
ν_μ total			$2.27^{+.52}_{-.51} \times 10^{-18}$

Table A-8 Expected interacted energy, cross-section and rate of prompt ν_e and ν_μ

Uncertainties in the total interaction rate are found in the same manner as they were for ν_τ, using multiple simulation with varied inputs to equation 8-10. The distribution of interaction rates obtained from ten thousand simulated experiments is shown in Figure A-8-5.

Interaction rate for ν_μ from sources other than charm

Neutrinos from sources other than charm decay are muon neutrinos that result from pions and kaons that decay in the dump. The light mesons are produced in great numbers in the proton-Tungsten interactions and both have significant branching fractions to ν_μ . The modes decay mode to $\nu_\mu + \mu$ account for essentially all charged pion decays and ~63% of charged kaon decays; essentially all other charged kaon decays result in at least one charged pion. Charged kaon decays result in a ν_e only ~4% of the time. The neutral K^0_L decay products include a ν_e 40% of the time and a ν_μ. 27% of the time.[27] Neutrinos from these non-charm decay sources are labeled 'non-prompt'.

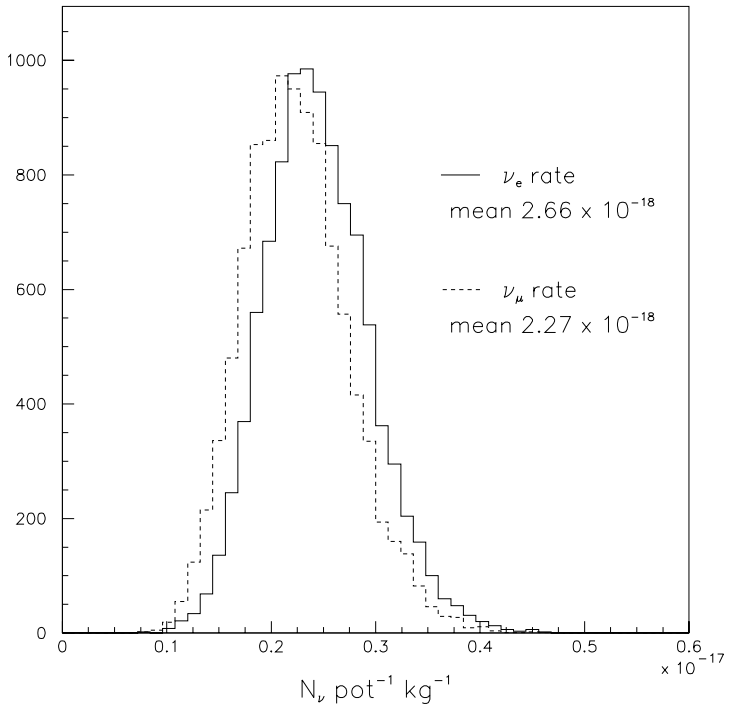

Figure A-8-5 ν_e and ν_μ interaction rates from ten thousand simulations, each using one hundred generated neutrinos.

'Non-prompt' neutrinos are on average much less energetic than those from 'prompt' sources since the available phase space is much greater for the charmed meson

decays. Also, it is predominantly the lower momentum light mesons which decay before they interact in the dump: the probability of decay is a function of proper time whereas the probability of interaction depends only of path length traveled.

Light meson production and decay

Mesons are produced in a shower like fashion in the dump, resulting not only from the initial proton–nucleon interaction but all subsequent interaction of the initial products. The physics of light meson productions is well understood and reliably modeled. A Monte Carlo simulation of the production and decay of pions and kaons is used to calculate the flux of ν_μ from these sources a the emulsion target.[28]

A GIESHA simulation [33] of 800 GeV/c protons interacting in Tungsten is used to create the light mesons. A weight is assigned to each pion and kaon created in the interaction equal to the probability of it decaying before it re-interacts in the tungsten dump. Decay lengths are calculated from a lifetime, T, that is chosen from an from distribution e^{-T}, the interaction distance, L, is taken from a distribution proportional to $e^{-L/\lambda}$, where λ = 9.65 cm. is the nuclear interaction length in tungsten. Ä simulation of the leptonic or semi-leptonic channels is performed sand the resulting neutrino is projected to the emulsion target position. The flux of ν_μ and average energy weighted by interaction probability is shown in Table A-. The uncertainty is almost entirely due to the total proton-tungsten cross-section.

source	ϕ_ν ($pot^{-1}m^{-2}$)	$\langle Energy_\nu \rangle$ (GeV)	Rate (kg^{-1} $proton^{-1}$)
$\pi^\pm$	$6.9 \pm 1.2 \times 10^{-5}$	28.4	$2.4 \pm 0.4 \times 10^{-18}$
$K^\pm, K^0_L$	$2.6 \pm 0.4 \times 10^{-5}$	63.5	$2.0 \pm 0.3 \times 10^{-18}$

Table A-9 Non-prompt neutrino flux and energy. From reference 28

[1] S.Weinberg, Phys. Re. Lett. 19, 1264 (1967)
[2] A. Salam. *Elementary Particle Theory* ed. N. Sartholm (Almquist and Forlag 1968)
[3] F. Reines and C. L. Cowan,Jr. Phys. Rev 92, 8301 (1953)
[4] R. Davis and D.S. Harmer, Bull. Am. Phys. Soc. 4, 217 (1959)
[5] Danby et al., Phys. Rev. Lett. 9, 36 (1962)
[6] M. Perl et al., Phys. Rev. Lett. 35, 1489 (1975)
[7] The LEP Electroweak working group, LEPEWG/94-01
[8] ARGUS Collaboration Phys. Lett. B 202, 149 (1988)
[9] w. Seligman, Ph.D. Thesis, Nevis Report 292 (1996).
[10] P. S. Auchincloss *et al*, Z. Phys., C48, 411 (1990).
[11] D. B. MacFarlane *et al*, Z. Phys., C26, 1 (1984).
[12] P. Berge *et al*, Z. Phys., C35, 443 (1987).
[13] J. Morphin *et al*,Phys. Lett., 104B, 235 (1981).
[14] D. C. Coley *et al*, Z. Phys., C2, 187 (1979).
[15] S. Campollio *et al*, Phys. Lett., 80B, 309 (1979).
[16] O.Erriquez *et al*, Phys. Lett., 84B, 281 (1979).
[17] A.S. Vovenko *et al*, So.J.Nucl. Phys. 30, 527 (1979).
[18] D.S. Baranov *et al*, Phys. Lett., 81B, 255 (1979).
[19] C. Baltay *et al*, Phys. Rev. Lett. 44, 916, (1990).
[20] S.J. Barish *et al*, Phys. Rev. D44, 2521, (1979).
[21] N.J. Baker *et al*, Phys. Rev. D25, 617, (1982).
[22] J. V. Allaby *et al*, Z. Phys., C38, 403 (1979).
[23] C. Albright abd C. Jarlskog Nucl. Phys. B40, 85 (1975)
[24] E. Eichten et al Supercollider Physics, Rev. Mod. Phys. 56, 579 (1984): erratum 58 1065.
[25] J.Z. Bai et al Physics Reiew D 53, 20 (1996)
[26] R .Barte et al Phys. Lett. B 414, 362 (1997)
[27] D.E. Groom et al, The European Physics Journal C15, 1 (2000)
[28] P. Berghaus Ph.D. Thesis (2001)
[29] R. Schwienhorst Ph.D. Thesis (2000)
[30] S.Aoki et al., Nuclear Tracks 12, 249-252 (1986)
[31] S. Aoki *et al*., Nucl. Inst. Meth. B51 466-472 (1990)
[32] G. Ingelram, J.Ratham, A.Edin, *LEPTO- The LUND Monte Carlo for Deep Inelastic Lepton-Nucleon Scattering*, Comp. Phys. Comm. 101,108-134 (1997)
[33] Application Software Group, *GEANT - Detector Description and Simulation Tool*, CERN Geneva, Switzerland (1998)
[34] Niki Sa…. E872 internal memo ANN …..
[35] S.Frixione e-Print archive: hep-ph/9702287
[36] A.Alton *et al*., Phys. Rev. D46 (2001) 012002
[37] T.Bollton prerint hep-ex/9708014
[38] Mark III collaboration, Phys. Rev. B263, 135 (1991)
[39] http://charon.web.cern.ch/charon

[40] W.M Geist, Nucl. Phys. A 525 149c-169c (1991)
[41] F. James *MINUIT Reference manual* (*version 94.1). Program Library* D506. CERN (1998)
[42] G. Cowan, *Statistical data Analysis* (Oxford University Press, 1998).
[43] D.S. Barton et al Phys. Re. D27, 2580 (1983)
[44] S. Fredriksson et al., Phys. Rep144,187 (1987)
[45] D. Bortoletto Et al., Phys. Rev. D37: 1719-1743 (1988)
[46] S. Barlag et al., Z. Phys. C49 555-562 (1991)
[47] M.Adamoich et al., Nucl. Phys. B495:3-34 (1997)
[48] K. Kodama et al., Phys. Lett. B 284: 461-470 (1992)
[49] K. Kodama et al., Phys. Lett. B 263: 573-578 (1991)
[50] J.C. Anjos et al., Phys. Rev. Lett. 62,5:513-516 (1989)
[51] G.A. Alves et al., Phys. Rev. Lett. 77:2388-2395 (1996)
[52] R.Ammar et al., Phys. Rev. Lett. 61, 19:2185-2188 (1988)
[53] D.M. Kaplan et al., Int. J. Mod. Phys. A 12: 3827-3863 (1997)
[54] M. Adamovich et al., Phys. Lett. B 284:453-456 (1992)
[55] M. Adamovich et al., Nucl. Phys. B 495:3-34 (1997)
[56] G.A. Alves et al., Phys. Rev.Lett. 70:722-725 (1993)
[57] M.J.Leitch et al., Phys.Prev.Lett. 72:2542-2545 (1994)
[58] Accairri et al Phys. Lett. B396 327 (1997)
[59] S. Sbarra talk at the Recontres de Moriond, Les Arcs France (March 11-18,2000)
[60] M. Chana et al Phys. Re. D58: 032002 1-100 (1998)
[61] S. Aoki et al Prog. Theor. Phys. 98:131 (1993)
[62] J. Z. Bai et al Phys Re. Lett. 74: 4599 (1995)
[63] K. Kodama et al., Phys. Lett. B382: 299 (1996)
[64] F. Parodi et al., HEP'97 conference Jerusalem,1997, paper 455
[65] S. Fixione, M.L. Mangano, P. Nason and G Ridolifi, in Heavy Flaours II, eds. A. J. Buras, world Scientific Publishing Co., Singapore (1998)
[66] R. Ammar et al., Phys. Lett. B 183: 110 (1987). Erratum- ibid. B192: 478 (1987)